The Effect of Interference Techniques on Fischer-Tropsch Product Distributions

by

James Michael Bucher

A dissertation submitted in partial fulfillment
of the requirements for the degree of
Doctor of Philosophy
(Chemical Engineering)
in the University of Michigan
2010

Doctoral Committee:

Professor Johannes W. Schwank, Chair
Professor Melanie Sanford
Professor Phillip Savage
Adjunct Professor Galen Fisher

To Amy and my family

Acknowledgments

I would like first to thank my adviser, Johannes Schwank, for providing the funding, inspiration, and feedback for the work presented in this dissertation. I would also like to thank Jerry Mader for his hard work in procurement of funding for the Schwank research group. My research would not have been possible without their efforts in support of my colleagues and myself.

I would like to thank the past and present members of my committee – Phillip Savage, Scott Fogler, Melanie Sanford, and Galen Fisher – for their input into my doctoral work. A special thanks is in order for Galen Fisher, who made time in his schedule to meet with me several times over the final months of my graduate career to give input on a large portion of my research.

I would not have been able to complete my doctoral research without the considerable help of my fellow research group members. Thank you to Andy Tadd for providing aid and input in virtually every aspect of my experimental work, and thank you to Ben Gould for help in initially constructing my experimental system. Thank you to Tom Westrich, who helped carry out infrared catalyst studies, and thanks to him, Joe Mayne, and the rest of the Schwank research group for taking time over the past few years to discuss my research with me.

I would like to thank my family for their support and understanding in my pursuit

of a doctoral degree. I'd like especially to thank my wife Amy for her patience and unwavering support as I have completed my research and written my thesis.

Finally, I'd like to thank the friends I have made here at Michigan for their support throughout my graduate career. Scientific research is an inherently frustrating task, one that I probably would not have been able to endure without the encouragement and companionship of those who were experiencing it as well.

Table of Contents

List of Tables

List of Figures

List of Appendices

Abstract

Novel reaction engineering designs, also referred to as interference techniques, have been shown to improve the yield of heavier hydrocarbons in Fischer-Tropsch (FT) product distributions. This dissertation explores two such techniques: distributed syngas feeding and azomethane co-feeding.

An FT reaction model is first developed as an aid in simulating and understanding the experimental results presented herein. This model also explores whether the rate constants governing the FT polymerization reaction depend upon the length of the growing surface hydrocarbon chain.

A distributed syngas feeding strategy was employed experimentally by using two series plug flow reactors and feeding syngas into the entrances of both. The results from these experiments are compared against those from a normal feeding strategy in which syngas was fed only to the entrance of the first series reactor. A distributed feeding strategy is counterproductive to generating heavier product distributions when complete or near-complete CO conversion is effected within the first series reactor, leading to a decrease in C_{5+} hydrocarbon selectivity of over 60%. However, effecting only incremental CO conversion within the first series reactor leads to an improvement in C_{5+} hydrocarbon selectivity of up to 30% using a distributed feeding strategy. This result

represents a significant finding in that the weight of an FT product distribution was increased simply by altering the location of the inlet syngas.

Azomethane co-feeding was meant both to demonstrate a proof of concept in adding a recycled stream of activated methane to an FT reactor and to ascertain the occurrence of methyl termination steps in FT. Azomethane co-feeding experiments generated lighter product distributions compared to experiments in which deionized water was co-fed as a control – α values for C_8-C_{13} hydrocarbons were 0.69-0.70 for the water co-feeding experiments and 0.64-0.65 for the azomethane co-feeding experiments. However, the azomethane co-feeding experiments generated product distributions with greater paraffinic content than the corresponding water co-feeding experiments. These results demonstrate the likelihood that methyl termination steps take place on the surface of iron FT catalysts. Further exploration must be performed to find conditions in which a recycled, re-activated methane stream can improve heavy hydrocarbon selectivity.

Chapter One

Introduction

1.1 World Energy Supply and the Fischer-Tropsch Synthesis

Dwindling supplies of petroleum in conjunction with exponentially rising global demand may lead to a worldwide transportation fuel shortage within the next thirty to fifty years. The geologist M. King Hubbert, who correctly pinpointed the 1971 peak in U.S. crude oil production, calculated that the peak of world oil production would occur in 2005 [1]. His prediction appears to have been correct within two to three years [2]; as a result, the extreme price volatility observed for gasoline and diesel fuels during the summer of 2008 [3] may occur repeatedly in the near future on a more drastic scale.

Perhaps more problematic than the problems presented by declining petroleum quantity are those presented by the degradation in overall petroleum quality. Petroleum refiners consider sources of crude oil that are substantially free of sulfur, i.e., sweet, and consist of lighter hydrocarbons, i.e., light, to be favorable due to the ease with which they are processed into gasoline and diesel fuels. However, crude oil recovered today contains increasing amounts of sulfur, aromatic species, and heavy residues [4], all of which increase the technical difficulty and operating costs of petroleum refining. Such refining challenges may throttle the supply of transportation fuels and exacerbate the volatility seen in gasoline and diesel prices.

Synthetic transportation fuels produced from plentiful feedstocks would alleviate potential difficulties presented by crude oil supply shortages. In the United States, coal deposits exist in the greatest abundance relative to other fossil fuel resources, with reserves estimated to last another 234 years at current consumption rates [5]. A domestic synthetic fuel program based on coal would simultaneously extend the nation's supply of transportation fuel while granting a measure of energy independence. Other large industrialized nations rich in coal reserves, such as China, Russia, and India, would also benefit from implementing such a program themselves.

The Fischer-Tropsch (FT) synthesis provides one potential route from coal to transportation fuel. The reaction was discovered in the 1920s by chemists Hans Tropsch and Franz Fischer, and it has been utilized industrially for coal-based fuel production since that time. The process involves first gasifying coal to carbon monoxide and hydrogen gases, a mixture known as syngas, followed by subsequent conversion of those gases at high pressure over a transition metal catalyst to hydrocarbon products. A wide array of these hydrocarbon products are generated, ranging in weight from methane to heavy paraffin waxes. Sections 1.2 and 1.3 further describe FT product distributions.

FT fuels compete with conventional fuels when the price of crude oil is $40 per barrel or above [6], but the enormous initial capital costs associated with FT plants have deterred widespread construction in most industrialized nations. Approximately 60-70% of these capital costs are associated with syngas production from coal, whereas product refining operations comprise another 10% of costs [7]. Increasing the yield of fuels relative to unwanted products such as methane would decrease the costs affiliated with both syngas production and product refining, thereby making FT a more economically

viable alternative to conventional transportation fuels. Furthermore, a breakthrough in narrowing FT product selectivity within a specific range could make smaller, distributed FT systems possible.

The research put forth in this dissertation endeavors to increase the yield of FT products in the transportation fuel range (C_8-C_{16} hydrocarbons) by implementing novel reaction engineering schemes, also referred to as interference techniques herein. Section 1.4 discusses in further detail previous examples of interference techniques from the scientific literature. Section 1.5 previews the specific techniques discussed in the subsequent chapters of this dissertation.

1.2 Fischer-Tropsch Chemistry

The FT synthesis produces hydrocarbons and water from carbon monoxide and hydrogen gases, two of the main constituents of syngas. The reaction takes place at elevated pressures (1-10 MPa) and relatively mild temperatures (200-350°C). Common industrial catalysts include iron and cobalt; nickel exhibits some activity toward FT but produces primarily methane, and ruthenium exhibits excellent FT activity but is not abundant enough for industrial use. The reaction stoichiometry is shown in Equations 1-1 and 1-2 by classification of the hydrocarbon product.

n-paraffin: $$nCO + (2n+1)H_2 \rightarrow C_nH_{2n+2} + nH_2O \quad (1\text{-}1)$$

α-olefin: $$nCO + 2nH_2 \rightarrow C_nH_{2n} + nH_2O \quad (1\text{-}2)$$

The synthesis also generates branched paraffins, β-olefins, and alcohols as minor products. The research described in the following chapters focuses exclusively on n-

paraffins and α-olefins as FT hydrocarbon products and ignores the aforementioned minor products.

The most commonly accepted mechanism for the growth of Fischer-Tropsch products involves the stepwise addition of methylene monomers to a hydrocarbon chain growing on the catalyst surface [8], summarized in Figure 1.1. Carbon monoxide and hydrogen are thought to dissociate into their respective elemental species on the catalyst surface (a), followed by hydrogenation of carbon to methyl and methylene species and removal of oxygen by hydrogen to form water (b and c). Methyl species act as hydrocarbon chain initiators into which methylene monomers insert themselves successively (d). Paraffins are formed as the result of hydrogen termination of the growing chain, whereas olefins result from hydrogen abstraction and desorption (e).

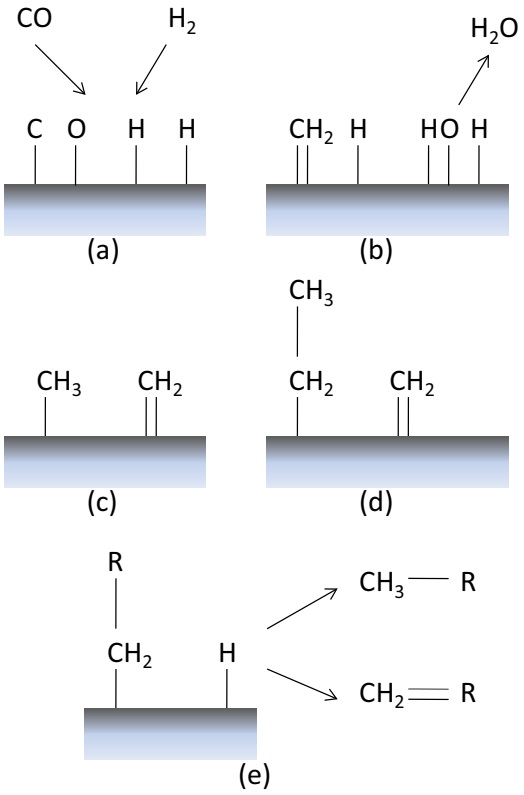

Figure 1.1: Depiction of CH_2 insertion mechanism for FT chain growth.

Several alternate explanations for the mechanism of FT hydrocarbon production exist in the scientific literature. Olefin formation has also been explained by means of the so-called alkenyl mechanism, in which a surface bound ethylene species ($-CH=CH_2$) acts as the initiator [9,10]. Methylene monomers then successively insert themselves into the bond between the CH group and the surface. Prior to the next methylene insertion, isomerization of the surface hydrocarbon chain occurs so that the double bond is always in the beta position relative to the surface. Termination of the surface chain by hydrogen then results in α-olefin formation. The alkenyl mechanism does not account for the direct production of paraffin species.

Multiple mechanisms have been put forth in the literature suggesting that carbon monoxide does not dissociatively desorb into elemental species on the catalyst surface [11-15]. Such proposals maintain that an oxygenated carbon surface species takes part in the initiation and propagation steps of the FT chain growth process. Paraffins and olefins result from dehydration steps; the formation of oxygenates and alcohols can be explained by termination in the absence of dehydration.

The summary by Claeys and van Steen gives further details of the aforementioned FT reaction mechanisms [16]. The work presented in this dissertation assumes the methylene insertion mechanism to be prevalent on the catalyst surface, specifically in the FT reaction model put forth in Chapter Two.

Process conditions favorable to the production of heavier hydrocarbons include:

- Low temperature (220-250°C). Kinetic and thermodynamic considerations must be balanced, but higher temperatures thermodynamically favor the production of lighter hydrocarbon species such as methane.

- High pressure: Elevated pressure is necessary for heavier hydrocarbon production, as it maintains high concentrations of surface species.
- Low H_2/CO ratio: Increased hydrogen partial pressure leads to increased concentration of surface hydrogen. This in turn raises the rate of hydrogen termination steps relative to propagation, thereby decreasing chain growth probability.

1.3 The Anderson-Schulz-Flory Product Distribution and Deviations Therefrom

FT product distributions generally adhere to the Anderson-Schulz-Flory (ASF) distribution in which the molar selectivity of hydrocarbon products declines logarithmically with carbon number according to the example plot in Figure 1.2 from the work of van der Laan and Beenackers [17]:

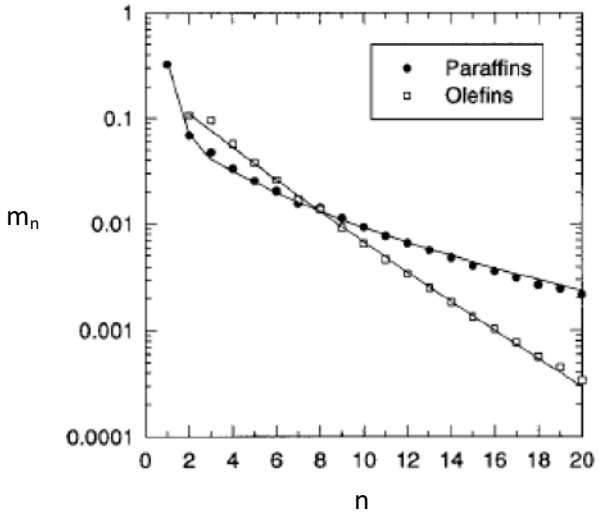

Figure 1.2: Depiction of a typical ASF plot, where m_n represents the molar selectivity of a hydrocarbon containing n carbon atoms [17].

The ASF distribution can be expressed analytically as:

$$m_n = n \ln \alpha + \ln\left(\frac{1-\alpha}{\alpha}\right), \tag{1-3}$$

where m_n represents the molar selectivity of a hydrocarbon product containing n carbon atoms and α represents chain growth probability. The α-value of an FT product distribution has a value between zero and one, where higher values indicate a heavier product distribution.

Both positive and negative deviations from the ASF distribution have been observed experimentally. Negative deviations, in which the selectivity of a certain hydrocarbon range is lower than predicted by ASF, have been explained by the accumulation of heavier hydrocarbon products in the slurry oil in which FT reactions typically have been held [18]. The explanations for positive deviations, in which the selectivity of a certain hydrocarbon range is higher than predicted by ASF, have been the source of more extensive debate within the literature.

One such explanation maintains that olefins produced during FT return to the catalyst surface, re-adsorb, undergo further chain growth, and finally desorb as longer chained paraffin species [19-26]. Iglesia et al. claim that diffusional limitations are responsible for this phenomenon, as heavier olefins move away from the catalyst surface more slowly and therefore have an increased chance of re-adsorbing [21]. Schulz et al. maintain that increased solubility of heavier hydrocarbons in the liquid layer surrounding the catalyst prevent heavier olefins from departing the catalyst surface as products, thereby increasing the likelihood of re-adsorption [23]. The assertions of both camps are supported by the fact that the olefinic content of hydrocarbon products decreases with increasing carbon number.

Mechanistic differences provide another possible explanation for positive deviations from ASF. Wojciechowski asserts that olefinic re-adsorption “plays no

observable role in the chain growth process" of the synthesis. He explains that two distinct termination reactions of paraffinic products – the first by hydrogen surface species, the second by methyl surface species – account for experimentally observed deviations [27]. Puskas and Hurlbut agree with Wojciechowski's assessment regarding the role of secondary olefinic re-adsorption and state generally that a multiplicity of chain growth probabilities leads to observed deviations from ASF [28]. Finally, Fernandes argues that these experimental observations result from the superposition of product distributions resulting from two hydrocarbon chain growth mechanisms [29].

The work presented in this dissertation does not endeavor to resolutely solve the previously described debate. However, the implications of the debate have influenced its hypotheses and conclusions.

1.4 The Use of Interference Techniques to Alter Fischer-Tropsch Product Distributions

Throughout the history of the FT synthesis, researchers have sought ways to increase the yield of heavier hydrocarbons by increasing the α-value of product distributions or effecting departures from ASF distributions altogether. Such improvements can generally be placed into one of two categories: novel catalyst synthesis or process condition optimization. Improvements in catalyst synthesis have included the promotion of conventional FT catalysts, such as the addition of alkali metals to precipitated iron catalysts [30]. Optimization of process conditions has included the development of high and low temperature Fischer-Tropsch synthesis (HTFT and LTFT respectively), where lower temperatures favor the production of heavier hydrocarbons [31].

More recently a third category of improvements to FT selectivity control has emerged, hereafter referred to as interference techniques. These techniques employ the use of novel reaction engineering schemes in an effort to interfere with normal FT reaction conditions and cause deviations from the conventional ASF distribution. In several cases researchers employing these techniques have greatly improved the selectivity of the synthesis in certain hydrocarbon ranges.

One such technique has involved the addition of alternate chemical species to the conventional FT reaction mixture of carbon monoxide and hydrogen. An example is the work of Snel and Espinoza, who co-fed dimethyl ether and diethyl ether with synthesis gas and observed both an increase in reactant conversion (carbon monoxide and co-fed oxygenates) and a decrease in methane selectivity [32]. Many studies have explored the effect of co-fed olefins in the conventional FT synthesis [23,25,26,33-35]. These studies have mainly investigated the potential effect of olefinic re-adsorption on FT product distributions, but some of these studies have reported improved yields of heavier hydrocarbon products as a result of olefinic co-feeding.

In situ water removal from an FT catalyst bed has been shown in some cases to improve the activity and selectivity control of the synthesis given the propensity of water to retard the overall FT reaction rate [36-40]. Rohde et al. removed water from an iron catalyst bed using a selectively permeable membrane and found that conversion and hydrocarbon yield improved compared to a control reaction from which water was not removed [41]. This study mainly endeavored to examine the effect of water removal on total carbon conversion (both CO and CO_2) and overall hydrocarbon yield; as such, the relative yields of lighter and heavier hydrocarbons were not discussed.

Another example of interference techniques in the scientific literature involves the use of zeolites in conjunction with traditional FT catalysts. Li et al. demonstrated improved C_4-C_{10} selectivity when a zeolite catalyst was used in combination with a traditional cobalt catalyst in a two-stage reactor system [42]. Their system appears to have achieved this improved yield by means of hydrocracking longer chain hydrocarbons (i.e., C_{15+}) into lighter compounds. Zhao et al. performed similar experiments, using a variety of zeolite catalysts in the second of a two-stage reactor system for post-FT cracking and isomerization [43]. They found that a combination of zeolite and palladium as a second stage catalyst gave the highest selectivity of heavier hydrocarbons, reported in this case as C_{7+} hydrocarbons. The use of zeolites to improve the yield of heavier hydrocarbons in FT product distributions has become the subject of extensive study, with many examples present in the literature beyond those cited here.

Several researchers have explored the effect of staged hydrogen feeding strategies on FT product distributions. Sharifnia et al. employed a distributed hydrogen feeding strategy in a fixed bed reactor over a silica supported cobalt catalyst [44], while Guillou et al. performed similar staged hydrogen feeding experiments using 200μL micro-reactors [45]. Both research groups reported increased selectivity of C_{5+} hydrocarbons when hydrogen was fed into the catalyst bed downstream of the reactor entrance, although the reported conversion of carbon monoxide decreased.

1.5 Overview of Dissertation

The research presented in the following chapters of this thesis explores the effects of certain interference techniques on FT product distributions, explains the effects using a

combination of experimental and computational data, and challenges mechanistic theories prevalent in the literature that may be affecting these observations. Appendix A reviews definitions of important experimental and computational parameters referenced throughout this dissertation (CO conversion, hydrocarbon selectivity, carbon atom selectivity, paraffin fraction, chain growth probability); the reader should familiarize him or herself with these definitions before reading Chapters Two through Five. Chapter Two discusses the development of an FT reaction model based on carbon number dependent rate constants for FT propagation and termination steps; the predictions of this model are then compared to those of a model from the scientific literature. Chapters Three and Four examine FT product distributions resulting from a distributed syngas feeding regime employing dual series reactors. Chapter Five investigates the use of azomethane, a compound known for decomposing into methyl radicals, as a chemical co-feed in the FT synthesis. Chapter Six summarizes the results of Chapters Two through Five and elaborates upon future work that arises from the research described herein.

References

1. Deffeyes, Beyond Oil: The View From Hubbert's Peak, Hill and Wang, New York, 2005, p. 4.

2. W. Zittel, J. Schindler, Crude Oil: The Supply Outlook, Energy Watch Group, Ottobrunn, 2007, p. 11.

3. From data supplied by the Energy Information Administration of the United States Department of Energy, http://tonto.eia.doe.gov/dnav/pet/hist/LeafHandler.ashx?n=PET&s=MG_TT_US&f=W.

4. Organization of the Petroleum Exporting Countries Monthly Oil Market Report, August 2005, p. 3.

5. From data supplied by the Energy Information Administration of the United States Department of Energy, http://tonto.eia.doe.gov/energyexplained/index.cfm?page=coal_reserves.

6. National Energy Technology Laboratory of the Department of Energy, Baseline Technical and Economic Assessment of a Commercial Scale Fischer-Tropsch Liquids Facility, April 2007, p. 7.

7. M. Dry, J. Chem. Technol. Biotechnol. 77 (2001) 43-50.

8. M. Claeys, E. van Steen in: A. Steynberg, M. Dry (Eds.), Fischer-Tropsch Technology, Elsevier, Amsterdam, 2004, p. 605-606.

9. P. Maitlis et al., Chem. Commun. 1 (1996) 1-8.

10. P. Maitlis et al., App. Catal. A 186 (1999) 363-374.

11. H. Storch, N. Golumbic, R. Anderson, The Fischer-Tropsch and Related Synthesis, John Wiley and Sons, New York, 1951.

12. R. Gupta et al., J. Catal 26 (1972) 212-217.

13. A. Sternberg, J. Wender, Proc. Intern. Conf. Coordination Chem. 1 (1959) 53.

14. S. Roginski, Proc. 3rd Congr. Catal. 1 (1965) 939.

15. H. Pichler, H. Schulz, Chem. Ing. Tech 42 (1970) 1162-1174.

16. M. Claeys, E. van Steen in: A. Steynberg, M. Dry (Eds.), Fischer-Tropsch Technology, Elsevier, Amsterdam, 2004, p. 609-613.

17. G. van der Laan, A. Beenackers, Ind. Eng. Chem. Res. 38 (1999) 1277-1290.

18. R. Dictor, A. Bell, Ind. Eng. Chem. Proc. Des. Dev. 22 (1983) 678-681.

19. R. Madon, E. Iglesia, J. Catal. 139 (1993) 576-590.

20. R. Madon, S. Reyes, E. Iglesia, J. Phys. Chem. 95 (1991) 7795-7804.

21. E. Iglesia et al., Advances in Catal. 39 (1993) 221-302.

22. R. Madon, E. Iglesia, J. Catal. 149 (1994) 428-437.

23. H. Schulz, M. Claeys, App. Catal. A 186 (1999) 71-90.

24. E. Kuipers, I. Vinkenburg, H. Oosterbeck, J. Cat. 152 (1995) 137-146.

25. E. Kuipers et al., J. Catal. 158 (1996) 288-300.

26. D. Dwyer, G. Somorjai, J.Catal. 56 (1979) 249-257.

27. B. Wojciechowski, Catal. Reviews 30 (1988) 629-702.

28. I. Puskas, R. Hurlbut, Catal. Today 84 (2003) 99-109.

29. F. Fernandes, Chem. Eng. Technol. 28 (2005) 930-938.

30. M. Dry in: J. Anderson and M. Boudart (Eds.), Catalysis Science and Technology Vol. 1, Springer Verlag, Berlin, 1981, p. 182.

31. A. Steynberg, M. Dry, B. Davis, B. Breman in: A. Steynberg, M. Dry (Eds.), Fischer-Tropsch Technology, Elsevier, Amsterdam, 2004, p. 64-66.

32. R. Snel, R. Espinoza, J. Mol. Catal. 54 (1989) 213-223.

33. C. Satterfield et al., J. Catal. 80 (1983) 486-490.

34. W. Hall, R. Kokes, P. Emmet, J. Amer. Chem. Soc. 82 (1960) 1027-1037.

35. H. Schulz, B. Rao, M. Elstner, Erdöl Kohle Erdgas Petrochem. Brennst. Chem. 23 (1970) 651-660.

36. M. Dry, Ind. Eng. Chem. Prod. Res. Dev. 15 (1976) 282-286.

37. R. Anderson, U.S. Bureau of Mines Bulletin (1964) 614.

38. G. Huff, C. Satterfield, Ind. Eng. Chem. Process Des. Dev. 23 (1984) 696-705.

39. S. Ledakowicz et al., Ind. Eng. Chem. Process Des. Dev. 24 (1985) 1043-1049.

40. T. Das et al., Energy & Fuels 19 (2005) 1430-1439.

41. M. Rohde et al., Ind. Eng. Chem. Res. 44 (2005) 9653-9658.

42. X. Li et al., Catal. Today 84 (2003) 59-65.

43. T. Zhao, Ind. Eng. Chem. Res. 44 (2005) 769-775.

44. S. Sharifnia et al., Fuel Proc. Technol. 86 (2005**)** 1253-1264.

45. L. Guillou et al., Chem. Eng. Journal 136 (2008) 66-76.

Chapter Two

Fischer-Tropsch Reaction Modeling

2.1 Introduction

This chapter concentrates on the development of a reaction model capable of accurately calculating FT product distributions. The experimental work presented in subsequent chapters of this dissertation was performed using plug flow reactors, the concentration profiles of which can prove difficult to measure. The trends along the axes of plug flow FT reactors may be ascertained by simulating experiments using a mathematical FT model, thereby improving the understanding of effects observed during the experiments. The model of the present chapter is developed from and validated with experimental results from a continuously stirred tank reactor; the model's applicability to the analysis of plug flow reactor systems is briefly discussed in Chapter Four.

The deviations from ASF discussed in Section 1.3 have provided a special challenge to those endeavoring to create a model that accurately predicts FT product distributions. Teng et al. developed an FT model for an industrial Fe-Mn catalyst, but it failed to predict experimental deviations from ASF [1]. Fernandes created an FT model that assumed the occurrence of two simultaneous oligomerization reactions over a precipitated iron catalyst [2]. He claimed good agreement with experimental data, but his analysis suffered from faulty assumptions in quantifying the concentration of surface methylene monomers and neglected to take into account the water-gas shift reaction.

Nowicki et al. [3], van der Laan and Beenackers [4], Zimmerman et al. [5], and Schulz and Claeys [6] designed hydrocarbon selectivity models over precipitated iron catalysts that took into account secondary olefin reactions. The study of van der Laan and Beenackers claimed good agreement between an olefin re-adsorption model and experimental data [4]; however, the comparisons of computational and experimental hydrocarbon selectivities in that study (Figures 4, 9, 12, and 15) separated the plots of olefins and paraffins. All hydrocarbon species containing the same number of carbon atoms must be plotted together to accurately determine the extent of experimental deviations from ASF and the extent to which a mathematical model agrees with those deviations, as noted by Iglesia [7]. Zimmerman et al. appropriately depicted hydrocarbon selectivity on a semilogarithmic plot (Figure 3) and claimed good agreement between their olefin re-adsorption model and experimental data [5]. Their model accurately reflects the negative deviations experimentally observed at carbon numbers greater than 25 but adheres to ASF for C_1-C_{25} hydrocarbons. Closer examination of Figure 3 reveals that the olefin re-adsorption model over-calculates methane selectivity compared to experimental data.

In the above cited studies, the rate constants that govern the propagation and termination reactions of the FT polymerization are treated as independent of the intermediate hydrocarbon chain length. Positive deviations from ASF have been described mainly by re-adsorption of olefins onto the catalyst surface followed by further chain growth. A distinct termination constant for C_1 surface groups has been derived in some cases to account for unexpectedly high methane selectivity, but propagation and termination of all species heavier than C_2 are assumed to be driven by the same constants.

This assumption holds provided that the intermediate hydrocarbon chain grows away from the catalyst surface and does not interfere with subsequent reactions, as depicted in the "growing tree" model of Figure 2.1(a). If the hydrocarbon chain intermediate propagates along the surface of the catalyst as depicted in the "earthworm" model of Figure 2.1(b), the intermediate chain may interfere with subsequent propagation and termination steps. In this case, the relevant rate constants would depend strongly on the length of the intermediate hydrocarbon chain.

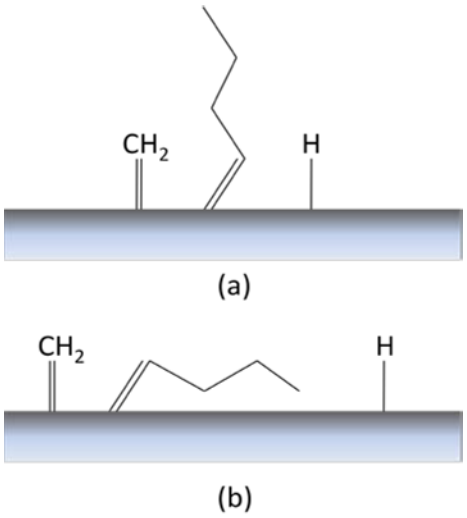

Figure 2.1: Depiction of physical hydrocarbon chain growth from the chemisorbed site. (a) The "tree" growth model, in which the hydrocarbon chain grows away from the catalyst surface. (b) The "earthworm" growth model, in which the hydrocarbon chain grows along the catalyst surface.

The current study explores the validity of an FT reaction model based on carbon number dependent rate constants over precipitated iron catalysts. Hydrocarbon product rates up to C_{10} are calculated and compared to experimental data. As iron FT catalysts have simultaneous activity to the water-gas shift reaction, the kinetics of this side reaction are necessarily included in the model. Experimental data generated by van der Laan and

Beenackers [4] are used to derive rate constants and to further validate the model. The FT output parameters calculated by the carbon number dependent model of the current study are then compared to those of an olefin re-adsorption model (ORM) based on previously published mechanisms. The ORM operates under the popular theory in the scientific literature that non-ASF product distributions result from secondary olefin re-adsorption and chain growth. Relevant assumptions and mechanistic details are discussed in the following sections.

Model development and subsequent analysis are presented in two parts. First, two distinct models relying on carbon number dependent rate constants are developed. These models differ in the mechanism by which gas phase CO and H_2 form surface methylene and hydrogen species. The carbon number dependent quasi-equilibrium model (CNDQEM) assumes the gas phase reactants to be in quasi-equilibrium with elemental surface species, while the carbon number dependent empirical rate model (CNDERM) relates CO consumption and methylene monomer appearance to a well established rate law available in the literature [8,9]. The predictions of these models are then compared.

The second part of this analysis compares the CNDERM to one that assumes olefins re-adsorb to the catalyst surface and undergo secondary reactions, hereafter referred to as the ORM. The equations derived by van der Laan and Beenackers [4] are used to describe these secondary olefinic reactions mathematically. Due to the superior accuracy of the CNDERM in approximating experimental CO conversions, the empirical rate method is also used to describe CO conversion to methylene monomers in the ORM. In this manner an unbiased comparison of the CNDERM and ORM could be made.

2.2 Development of Fischer-Tropsch Reaction Model

For the purposes of this study, the FT reaction is assumed to take place in a well mixed slurry reactor without concentration or temperature gradients. The model catalyst, based on the catalyst used in the experiments and model of van der Laan and Beenackers [4], is composed of precipitated iron supported by silica and promoted by copper and potassium. Catalyst particle size is taken to be sufficiently small so that intra-particle diffusion limitations do not dictate the rate of reaction. Finally, the FT and water-gas shift reactions are assumed to occur on different catalytic sites. This assumption is supported by the work of Rao et al., who found that the water-gas shift reaction takes place on catalytic sites composed of irreducible magnetite [10]. It is well established in the scientific literature that FT takes place on an iron carbide phase (Fe_5C_2) that results from the pre-reduction and conditioning of hematite [11].

2.2.1 Elementary Rate Steps

2.2.1.1 Fischer-Tropsch Synthesis

Two distinct models were developed to express the transformation of gaseous carbon monoxide and hydrogen into water and surface methylene monomers. The CNDQEM assumes that the forward and reverse rates of reactant dissociation are approximately equal. The CNDERM assumes that the formation of methylene monomers is irreversible and rate limiting. The elementary steps for the CNDQEM are shown in Equations 2-1 through 2-4.

$$CO + 2s \xleftrightarrow{K_{CO}} Cs + Os \tag{2-1}$$

$$H_2 + 2s \xleftrightarrow{K_{H2}} 2Hs \tag{2-2}$$

$$2Hs + Os \xleftrightarrow{K_{H2O}} H_2O + 3s \tag{2-3}$$

$$Cs + 2Hs \xleftrightarrow{K_{CH2s}} CH_2s + 2s \tag{2-4}$$

In the preceding equations, *s* represents empty surface sites, *Hs* represents surface hydrogen, *Cs* represents surface carbon, *Os* represents surface oxygen, and CH_2s represents surface methylene monomers.

The CNDQEM simply assumes that carbon monoxide dissociates on the catalyst surface into elemental carbon and hydrogen. Similarly, hydrogen dissociates into surface elemental hydrogen. The combination of surface carbon and hydrogen to form methylene monomers occurs reversibly, as does the combination of surface hydrogen and oxygen to form water. Methylene monomers are then consumed irreversibly by a number of product formation steps that are described subsequently.

The rate limiting step of the CNDERM is related to an empirical rate equation established in the literature [8,9] for the consumption of carbon monoxide on iron catalysts. The elementary rate step and rate expression are depicted in Equations 2-5 and 2-6.

$$CO + 2H_2 + s \xrightarrow{-r_{CO}} CH_2s + H_2O \tag{2-5}$$

$$-r_{CO} = \frac{kP_{CO}P_{H2}}{P_{CO} + bP_{H2O}} \tag{2-6}$$

In Equation 2-6, $-r_{CO}$ represents the rate of carbon monoxide consumption in mol/h-g(Fe); P_{CO}, P_{H2}, and P_{H2O} represent the respective partial pressures of carbon monoxide, hydrogen, and water in MPa; *k* is a constant of units mol/h-g(Fe)-MPa; and *b* is a dimensionless parameter. Raje and Davis [12] found the values of *k* and *b* to be

0.398 and 3.016 respectively; the current study derives its own values for these parameters.

Hydrocarbon product formation is assumed to take place by means of a stepwise intermediate hydrocarbon chain growth mechanism from surface methylene monomers. This mechanism holds for both the CNDQEM and CNDERM, and its steps are depicted in Equations 2-7 through 2-12. Figures 1.1(c) through 1.1(e) (Chapter One) depict the relevant product formation steps. Initiating methyl species are produced upon reaction of a methylene monomer with surface hydrogen. Chain propagation occurs by means of methylene monomer insertion into the bond between the methyl species and the catalyst surface; successive methylene insertion steps further propagate the surface-bound hydrocarbon chain. Termination may occur through either hydrogen addition to form an n-paraffin or hydrogen abstraction to form an α-olefin. Isomerization products such as β-olefins and isoparaffins, although observed experimentally, are deemed to be produced at negligible rates compared to straight chained paraffins and α-olefins. Oxygenate production from FT is similarly neglected.

Initiation Step:

$$CH_2s + Hs \xrightarrow{k_i} R_1 + s \tag{2-7}$$

Propagation Steps:

$$R_1 + CH_2s \xrightarrow{k_{prop,1}} R_2 + s \tag{2-8}$$

$$R_2 + CH_2s \xrightarrow{k_{prop,2}} R_3 + s \tag{2-9}$$

$$R_n + CH_2s \xrightarrow{k_{prop,n}} R_{n+1} + s \tag{2-10}$$

Termination Steps:

$$R_n + Hs \xrightarrow{k_{pn}} P_n + s \tag{2-11}$$

$$R_n + s \xrightarrow{k_{on}} O_n + Hs + s \tag{2-12}$$

The symbols R_n, P_n, and O_n respectively represent adsorbed hydrocarbon chains, desorbed paraffin products, and desorbed olefin products, each containing *n* carbon atoms.

2.2.1.2 Water-Gas Shift Reaction

Simultaneous water-gas shift kinetics must also be taken into account given the activity of iron catalysts for this reaction. The formate mechanism, described in detail by Teng et al. [13], is assumed to be responsible for all carbon dioxide formation through the water-gas shift reaction in the reactor system. Equations 2-13 through 2-15 depict the relevant elementary rate steps.

$$CO + H_2O + 2s \xrightarrow{K_1} COOHs + Hs \tag{2-13}$$

$$COOHs \xleftrightarrow{k_2 / k_{-2}} CO_2 + Hs \tag{2-14}$$

$$2Hs \xrightarrow{K_3} H_2 + 2s \tag{2-15}$$

The term COOHs represents surface formate species; Equation 2-14 is assumed to be rate limiting.

2.2.2. Expressions for Product Formation Rates and Surface Intermediate Concentrations

2.2.2.1 Fischer-Tropsch Synthesis

Based upon the elementary rate steps in Equations 2-11 and 2-12, the n-paraffin and α-olefin production rates can be written as follows:

n-paraffin: $r_{pn} = k_{pn}[R_n][Hs]$ (2-16)

α-olefin: $r_{on} = k_{on}[R_n][s]$, n>1 (2-17)

The concentrations of surface species are not measurable experimentally, and therefore expressions for them in terms of measurable parameters must be derived.

- Surface Hydrogen

Solving the equilibrium expression for hydrogen dissociation resulting from Equation 2-2 in terms of [*Hs*] gives:

$$[Hs] = (K_{H2}P_{H2})^{0.5}[s] \quad (2\text{-}18)$$

The elementary rate step for hydrogen dissociation is identical for the CNDQEM and CNDERM; therefore, both models use Equation 2-18 to express surface hydrogen concentration.

- Surface Oxygen

The surface oxygen term, [*Os*], appears in the CNDQEM only. Rearranging the equilibrium expression resulting from Equation 2-3 and substituting Equation 2-18 for the [*Hs*] term yield:

$$[Os] = \frac{P_{H2O}[s]}{K_{H2O}K_{H2}P_{H2}} \quad (2\text{-}19)$$

- Surface Carbon

As with surface oxygen, the surface carbon term, [*Cs*], appears only in the CNDQEM. Rearranging the equilibrium expression resulting from Equation 2-1 and substituting the expression for the [*Os*] term in Equation 2-19 give:

$$[Cs] = \frac{K_{CO}K_{H2}K_{H2O}P_{CO}P_{H2}[s]}{P_{H2O}} \tag{2-20}$$

- Surface Methylene

The CNDQEM assumes that carbon and hydrogen form surface methylene in a reversible fashion. Therefore, rearranging the equilibrium expression resulting from Equation 2-4 and respectively substituting Equations 2-18 and 2-20 for [*Hs*] and [*Cs*] give:

$$[CH_2s] = \frac{K_{CH2s}K_{CO}K_{H2}{}^2K_{H2O}P_{CO}P_{H2}{}^2[s]}{P_{H2O}} \text{ (CNDQEM)} \tag{2-21}$$

The formation of methylene monomers is considered to be rate limiting in the CNDERM. The quasi steady-state approximation (QSSA) is used to determine the concentration of surface methylene:

$$0 = r_{formation,CH2s} - r_{consumption,CH2s} \tag{2-22}$$

$$0 = r_{rds} - (k_i[Hs][CH_2s] + \sum_{n=1}^{\infty} k_{prop,n}[R_n][CH_2s]) \tag{2-23}$$

The rate determining step term, r_{rds}, is equivalent to the empirical rate of carbon monoxide consumption (Equation 2-6). Methylene is consumed in reactions with surface hydrogen (initiation) and surface hydrocarbon chains (propagation), respectively represented by the two consumption terms in Equation 2-23. Solving for [CH_2s] in this equation gives:

$$[CH_2s] = \frac{\left(\frac{kP_{CO}P_{H2}}{P_{CO} + bP_{H2O}}\right)}{k_i[Hs] + \sum_{n=1}^{\infty} k_{prop,n}[R_n][CH_2s]} \text{ (CNDERM)} \tag{2-24}$$

- Intermediate Hydrocarbon Chains

Expressions for intermediate hydrocarbon chains are identical for the CNDQEM and CNDERM. The QSSA is used to derive expressions for these species.

Methyl species (represented by the term R_1) are formed upon reaction of surface hydrogen with a methylene monomer (Equation 2-7) and are consumed by propagation and hydrogen termination steps (Equations 2-8 and 2-11 respectively). Therefore:

$$0 = k_i[Hs][CH_2s] - (k_{p1}[Hs][R_1] + k_{prop,1}[CH_2s][R_1]) \tag{2-25}$$

$$R_1 = \frac{k_i[Hs][CH_2s]}{k_{p1}[Hs] + k_{prop,1}[CH_2s]} \tag{2-26}$$

Hydrocarbon chains with more than one carbon atom can be propagated by a methylene monomer, terminated by hydrogen addition to form a paraffin, or terminated by hydrogen abstraction to form an olefin. The QSSA expression for these surface chains of n carbon atoms (R_n) can be written:

$$0 = k_{prop,n-1}[R_{n-1}][CH_2s] - (k_{pn}[Hs][R_n] + k_{on}[s][R_n] + k_{prop,n}[CH_2s][R_n]) \tag{2-27}$$

$$R_n = \frac{k_{prop,n-1}[R_{n-1}][CH_2s]}{k_{p1}[Hs] + k_{on}[s] + k_{prop,1}[CH_2s]} \tag{2-28}$$

- Empty Surface Sites

The sum of all surface species for each model can be written as:

$$[s_T] = [Hs] + [Os] + [Cs] + [CH_2s] + \sum_{n=1}^{\infty} R_n + [s] \quad \text{(CNDQEM)} \tag{2-29}$$

$$[s_T] = [Hs] + [CH_2s] + \sum_{n=1}^{\infty} R_n + [s] \quad \text{(CNDERM)} \tag{2-30}$$

The terms [s] and [s_T] represent the concentration of empty surface sites and the total concentration of sites available to perform FT chemistry, respectively. Normalization by [s_T] and rearrangement to solve for θ_s yield the expressions:

$$\theta_s = 1 - (\theta_H + \theta_O + \theta_C + \theta_{CH2} + \sum_{n=1}^{\infty} \theta_{Rn}) \quad \text{(CNDQEM)} \tag{2-31}$$

$$\theta_s = 1 - (\theta_H + \theta_{CH2} + \sum_{n=1}^{\infty} \theta_{Rn}) \quad \text{(CNDERM)} \tag{2-32}$$

Equations 2-18 through 2-28 were similarly normalized by [s_T].

The assumption of the CNDQEM that the methylene surface concentration is in quasi-equilibrium allows an analytical solution to be found for θ_{CH2} (Equation 2-21), but an analytical solution for θ_s cannot be calculated. Therefore, the CNDQEM must be solved numerically. The CNDERM allows analytical solutions to be calculated neither for θ_{CH2} nor θ_s, making a numerical solution necessary in this case as well.

2.2.2.2 Water-Gas Shift Reaction

The net rate of the water-gas shift reaction can be written from the rate determining step, Equation 2-14:

$$r_{WGS} = k_2[COOHs] - k_{-2}P_{CO2}[Hs] \tag{2-33}$$

Solving for [H_s] in the equilibrium expression resulting from Equation 2-15 yields the following expression for [Hs] on water-gas shift sites:

$$[Hs] = [s]\sqrt{\frac{P_{H2}}{K_3}} \tag{2-34}$$

Similarly, solving for [$COOHs$] in the equilibrium expression from Equation 2-13 and substituting Equation 2-34 for [Hs] give:

$$[COOHs] = \frac{K_1 P_{CO} P_{H2O}[s]}{\sqrt{\frac{P_{H2}}{K_3}}} \tag{2-35}$$

Summing total surface sites and normalizing by $[s_T]$ yields the following expression for empty water-gas shift sites:

$$\theta_s = 1 - (\theta_{COOH} + \theta_H) \tag{2-36}$$

Normalizing Equation 2-33 by the total number of available water-gas shift sites and substituting Equations 2-34 and 2-35 into 2-33 give the following rate expression:

$$r_{WGS} = \frac{k_2 K_1 P_{CO} P_{H2O} / \sqrt{P_{H2} / K_3} - k_{-2} P_{CO2} \sqrt{P_{H2} / K_3}}{1 + K_1 P_{CO} P_{H2O} / \sqrt{P_{H2} / K_3} + \sqrt{P_{H2} / K_3}} \tag{2-37}$$

2.2.3 Derivation of Equilibrium and Rate Constants

Van der Laan and Beenackers [4] published comprehensive conversion and selectivity data for FT over an Fe-Cu-K-SiO_2 catalyst in conjunction with a product distribution model. The data from Run 2 of that study were used to derive values for all equilibrium and carbon number dependent rate constants of the current model. A sum of least squares method was used to match the product formation rates calculated by the CNDQEM and CNDERM to the rates reported by van der Laan and Beenackers. The following expression was minimized using the solver algorithm in Microsoft Excel:

$$\sum_i \frac{(r_{i,\exp} - r_{i,calc})^2}{r_{i,\exp}} \tag{2-38}$$

with $r_{i,exp}$ and $r_{i,calc}$ representing the experimental and calculated rates of the *i*th component, respectively.

Table 2.1 summarizes the values of the equilibrium and rate constants found by the solver algorithm for the CNDQEM and CNDERM. The derivation of these rate constants leads to computations of a catalytic surface covered mainly by elemental carbon for the CNDQEM and by methylene monomers and hydrocarbon chains for the CNDERM. This calculation is consistent with the assumptions of van Steen and Schulz [14].

Table 2.1: Rate constants as derived by solver algorithm in Microsoft Excel. Conversion and selectivity data from Run 2 of the van der Laan and Beenackers study were used [4].

FT Equilibrium and Rate Limiting Step Constants			
CNDQEM		*CNDERM*	
K_{H2} (1/MPa)	0.894	K_{H2} (1/MPa)	0.972
K_{CO} (1/MPa)	$7.52(10^{-3})$	k (mol/h-g(Fe)-MPa)	0.183
K_{H2O} (MPa)	51.7	b (dimensionless)	3.02
K_{CH2} (dimensionless)	69.9		
FT Polymerization Constants			
	CNDQEM	*CNDERM*	
Initiation Constant (mol/h-g(Fe))			
k_i	1	1	
Propagation Constants (mol/h-g(Fe))			
$k_{prop,1}$	0.134	0.129	
$k_{prop,2}$	0.686	0.638	
$k_{prop,3}$	0.595	0.548	
$k_{prop,4}$	0.706	0.653	
$k_{prop,5}$	0.768	0.713	
$k_{prop,6}$	1.04	0.968	
$k_{prop,7}$	1.25	1.17	
$k_{prop,8}$	1.52	1.44	
$k_{prop,9}$	1.78	1.69	
$k_{prop,10}$	2.48	2.39	
Paraffin Termination Constants (mol/h-g(Fe))			
k_{p1}	1.67	1.73	
k_{p2}	1.40	1.40	
k_{p3}	0.527	0.518	
k_{p4}	0.709	0.701	
k_{p5}	0.737	0.730	
k_{p6}	0.660	0.659	
k_{p7}	0.700	0.704	
k_{p8}	0.723	0.731	
k_{p9}	0.719	0.730	
k_{p10}	0.706	0.723	
Olefin Termination Constants (mol/h-g(Fe))			
k_{o2}	1.44	1.49	
k_{o3}	2.10	2.15	
k_{o4}	1.77	1.82	
k_{o5}	1.72	1.78	
k_{o6}	1.54	1.61	
k_{o7}	1.35	1.42	
k_{o8}	1.18	1.25	
k_{o9}	1.17	1.24	
k_{o10}	0.988	1.06	

2.2.4 Development of Comparative Olefin Re-Adsorption Model

An olefin re-adsorption model (ORM) was developed to compare the performance of the current model to those that have been developed in the literature previously. The model was developed using the empirical rate method, whereby methylene formation from CO and H_2 was assumed to proceed at the rate described in Equation 2-6. An analogous quasi-equilibrium method was not developed for reasons elaborated upon in subsequent sections. As with the CNDQEM and CNDERM, rate and equilibrium constants were derived using a sum of least squares method comparing calculated product rates with those of Run 2 of the van der Laan and Beenackers study [4].

Six rate constants were included in the model: one to describe initiation events, one to describe propagation events, three to describe termination events (methane, C_2+ paraffins, olefins), and one to describe olefin re-adsorption. Van der Laan and Beenackers expressed the net rate of olefin production as the difference in olefin termination and re-adsorption rates:

$$r_{on} = k_o \theta_{Rn} \theta_s - k_{reads} P_{on} \tag{2-39}$$

with k_o representing the carbon number independent olefin termination constant, k_{reads} representing the rate constant for re-adsorption events, and P_{on} representing the partial pressure of an olefin with n carbon atoms. Van der Laan and Beenackers then show:

$$r_{on} = \frac{k_o \theta_{Rn} \theta_s}{1 + k_{reads} e^{cn}} \tag{2-40}$$

where c is a constant with a value of approximately 0.3 [15]. The concentration of intermediate hydrocarbon chains is then:

$$\theta_{Rn} = \frac{k_{prop}\theta_{R(n-1)}\theta_{CH2}}{k_p\theta_H + \frac{k_o\theta_s}{1+k_{reads}e^{cn}} + k_{prop}\theta_{CH2}} \tag{2-41}$$

All other expressions for reaction rates and surface intermediates are identical to the CNDERM. Table 2.2 summarizes the rate constant values of the ORM.

Table 2.2: Rate constants for the ORM.

k (mol/h-g(Fe))	0.182
b (dimensionless)	3.02
K_{H2} (1/MPa)	0.0123
k_i (mol/h-g(Fe))	1
k_{prop} (mol/h-g(Fe))	7.94
k_{meth} (mol/h-g(Fe))	9.44
k_p (mol/h-g(Fe))	0.461
k_o (mol/h-g(Fe))	0.412
k_{reads} (mol/h-g(Fe)-MPa)	0.380
c (dimensionless)	0.3

2.2.5 Quantification of Comparison between Model Calculations and Experimental Observations

Each of the above models were run under the conditions of Runs 1-4 of the van der Laan and Beenackers study and subsequently compared to experimental data for CO conversion, CO_2 selectivity, CO_2 production rate, hydrocarbon selectivity, and paraffin content. Mean absolute relative residuals (MARR) were calculated to quantify the closeness of the model calculation to experimental observation according to the following formula:

$$MARR = 100 \times \frac{\sum_{i=1}^{n} \frac{\left| v_{i,\mathrm{exp}erimental} - v_{i,\mathrm{mod}el} \right|}{v_{i,\mathrm{exp}erimental}}}{n} \tag{2-42}$$

where $v_{i,experimental}$ represents the experimental output value of the *i*th trial, $v_{i,model}$ represents the model output value of the *i*th trial, and *n* represents the total number of

trials. MARR values are expressed as percentage deviations from experimental observations; values under 25% are taken to indicate strong agreement between model and experiment whereas values above 40% indicate significant deviation. MARR values between these limits warrant further examination comparing computational and experimental trends, as discussed in the following sections.

2.3 Results and Discussion

2.3.1 Comparison of CNDQEM and CNDERM

2.3.1.1 Carbon Monoxide Conversion

Figure 2.2 compares the predicted and observed CO conversion levels under the experimental conditions of the van der Laan and Beenackers study. The CNDQEM predicts lower conversions than were observed experimentally for all experimental runs; the CNDERM predicts higher conversion than experiment for Runs 1 and 4 and lower conversion than experiment for Runs 2 and 3.

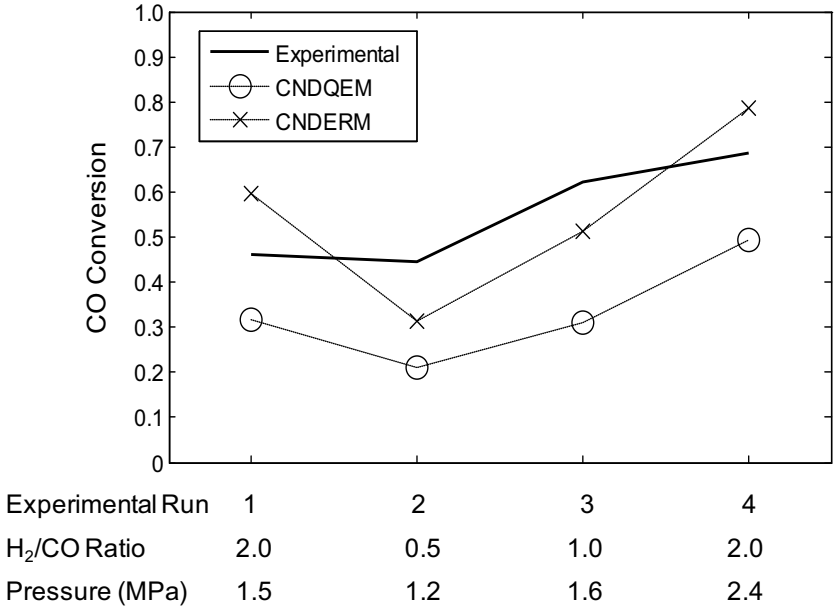

Figure 2.2: CO conversion calculated by CNDQEM and CNDERM. Experimental observations of van der Laan and Beenackers included for comparison.

Both models reflect the experimentally observed trend of increasing CO conversion with increasing inlet H_2/CO ratio. The CNDQEM ranges from 21.1% CO conversion for an inlet H_2/CO ratio of 0.5 to 49.3% CO conversion for an inlet H_2/CO ratio of 2, whereas the CNDERM varies between 31.2% and 78.7% for the same inlet H_2/CO values. The MARR values for CO conversion, averaged among Runs 1-4, were calculated from Equation 2-42 to be 40.6% and 22.8% for the CNDQEM and CNDERM respectively. These values indicate weak agreement for the CNDQEM and strong agreement for the CNDERM with regard to experimental CO conversion data.

2.3.1.2 Carbon Dioxide Selectivity and Production Rate

Figure 2.3 compares the CO_2 carbon atom selectivity and CO_2 production rates as calculated by the CNDQEM and CNDERM with the experimental data of van der Laan and Beenackers. The CNDERM more closely calculates the experimental values of CO_2

carbon atom selectivity, although neither model mimics the experimentally observed trend among experimental Runs 1-4. Both the CNDQEM and CNDERM accurately predict the experimental CO_2 production rates with the exception of Run 3, for which a drastically larger rate was reported experimentally relative to Runs 1, 2, and 4. Both models predict a relatively constant level of CO_2 production, varying by less than 6.0% among Runs 1-4.

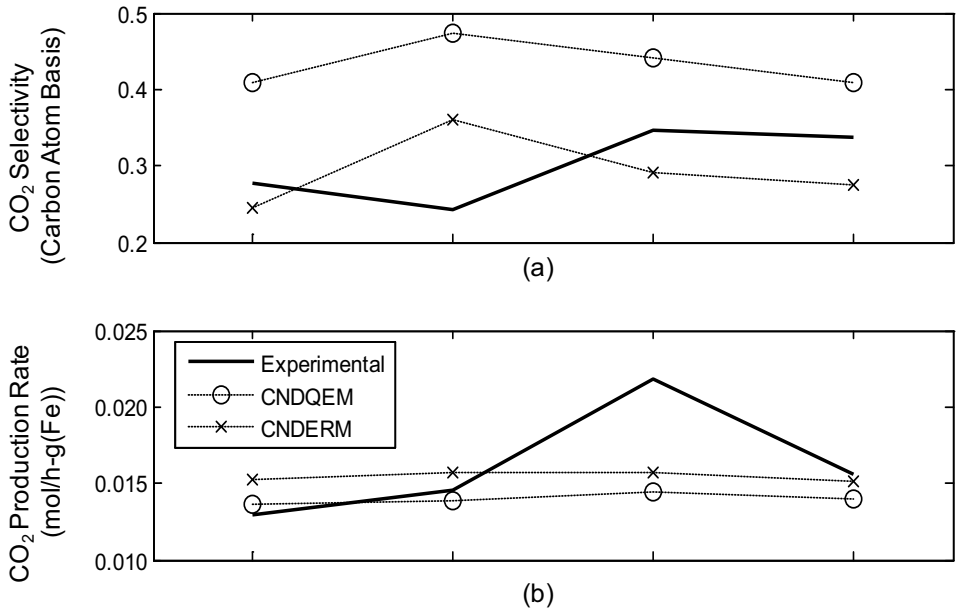

Experimental Run	1	2	3	4
H_2/CO Ratio	2.0	0.5	1.0	2.0
Pressure (MPa)	1.5	1.2	1.6	2.4

Figure 2.3: (a) CO_2 carbon atom selectivity and (b) CO_2 production rate calculated by CNDQEM and CNDERM. Experimental observations of van der Laan and Beenackers included for comparison.

The CNDQEM calculates a higher CO_2 carbon atom selectivity but a lower CO_2 production rate relative to both CNDERM and experimental data; this phenomenon can be explained by the lower overall CO conversion as predicted by the CNDQEM. Table 2.3 summarizes the MARR values that evaluate the performance of the CNDQEM and

CNDERM relative to the experimental data. Both models show strong agreement with experimental CO_2 production rates; however, the CNDQEM deviates significantly from experimentally reported CO_2 carbon atom selectivities, while the CNDERM demonstrates stronger agreement.

Table 2.3: MARR values (%) for CO_2 carbon atom selectivity and production rate averaged among Runs 1-4. Values shown are relative to experimental observations.

	CNDQEM	CNDERM
CO_2 Selectivity	47.6	23.5
CO_2 Production Rate	13.6	14.3

2.3.1.3 Hydrocarbon selectivity

Figure 2.4 depicts the experimental and calculated C_1-C_{10} hydrocarbon selectivities for each of experimental Runs 1-4. The CNDQEM and CNDERM exhibit similar selectivity values relative to each other over the entire hydrocarbon range that was simulated. Both models accurately predict the abnormally low C_2 and abnormally high C_3 selectivities that are characteristic of FT product distributions. The selectivity of hydrocarbons in the C_6-C_{10} range is closely predicted by both models for Runs 1-3, whereas a greater deviation between model and experimental results is observed for Run 4 over this hydrocarbon range.

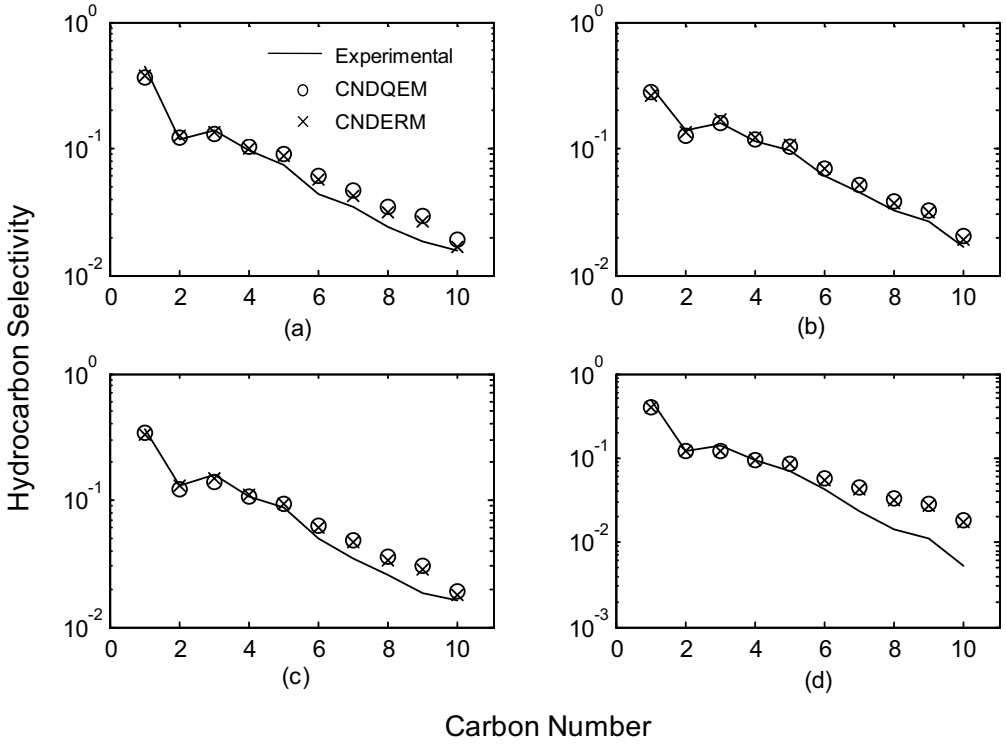

Figure 2.4: Hydrocarbon selectivities calculated by the CNDQEM and CNDERM for the conditions of experimental Runs (a) 1, (b) 2, (c) 3, and (d) 4 [4]. Solid lines represent experimental observations; individual marks represent model predictions.

Table 2.4 shows the MARR values describing the extent of variation between the model and experimental selectivities. The CNDERM strongly agrees with experimental hydrocarbon selectivities for Runs 1-3 and deviates significantly for Run 4; similar agreement exists between the CNDQEM and experiment. The CNDERM exhibits lower MARR values than the CNDQEM for each of Runs 1-4, indicating that the CNDERM more effectively calculates experimental hydrocarbon selectivities than the CNDQEM.

Table 2.4: MARR values (%) for hydrocarbon selectivity averaged among C_1-C_{10} species. Values shown are relative to experimental observations.

Experimental Run	CNDQEM	CNDERM
1	28.5	18.5
2	12.3	11.5
3	22.2	18.1
4	70.4	64.3

2.3.1.4 Paraffin Fraction

Figure 2.5 compares the paraffin fractions calculated by the models to those reported experimentally by van der Laan and Beenackers. The CNDQEM calculates a slightly larger paraffin fraction relative to the CNDERM along the entire hydrocarbon range and among all experimental runs. Both models correlate well with the experimental paraffin fraction values for Runs 1 and 2 but deviate more significantly for Runs 3 and 4.

Table 2.5 quantifies the relative differences between the model predictions and experimental observations via MARR values. The CNDQEM agrees strongly with experimentally reported paraffin fractions for Runs 1-3 – with MARR values below 10% for Runs 1 and 2 – and shows moderately strong agreement with experiment for Run 4. The CNDERM shows strong agreement with experiment for Runs 1 and 2 only with moderately strong agreement for Runs 3 and 4. The CNDQEM has lower MARR values than the CNDERM for each of Runs 1-4 with respect to experimental paraffin fraction data.

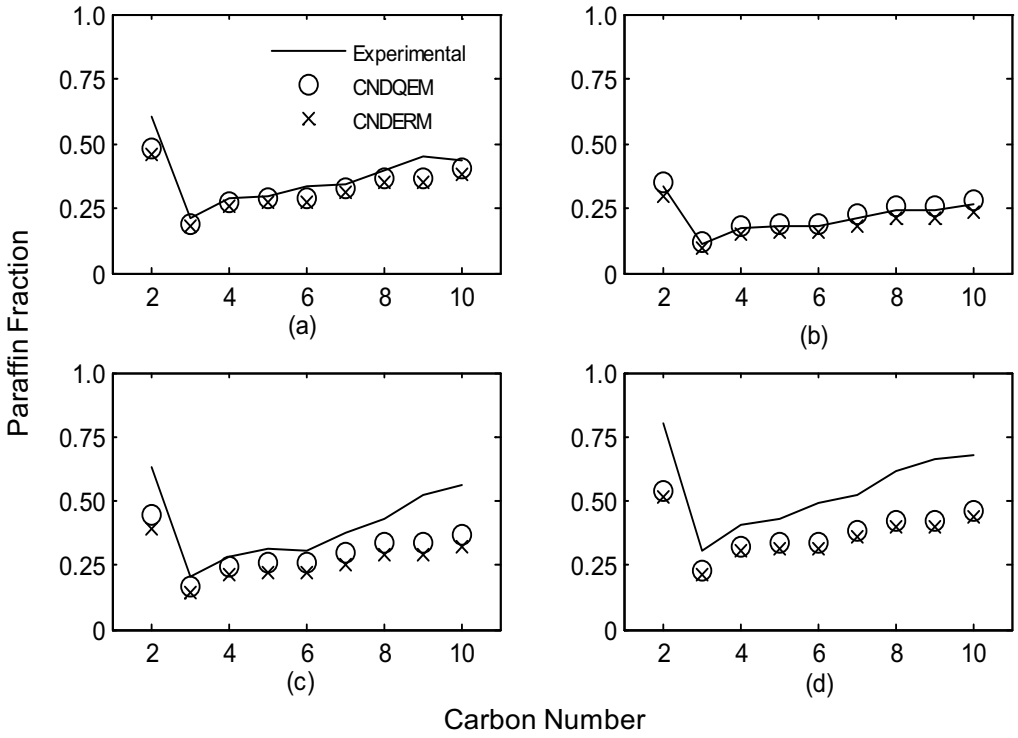

Figure 2.5: Paraffin fractions calculated by the CNDQEM and CNDERM for the conditions of experimental Runs (a) 1, (b) 2, (c) 3, and (d) 4 [4]. Solid lines represent experimental observations; individual marks represent model predictions.

Table 2.5: MARR values (%) for paraffin fraction averaged among C_2-C_{10} species. Values shown are relative to experimental observations.

Experimental Run	CNDQEM	CNDERM
1	9.99	14.5
2	6.44	12.2
3	22.6	33.9
4	28.8	32.9

2.3.1.5 Summary

Both models correlate best to the hydrocarbon selectivities and paraffin fractions of Run 2, with neither the CNDQEM nor CNDERM deviating by more than 12.3%. This result is unsurprising given that the kinetic and equilibrium parameters for both models

were derived using the data from this experimental run. Each model predicts the hydrocarbon selectivity results of Run 1 slightly better than those of Run 3, whereas the difference in model performance between Runs 1 and 3 is much more significant for the paraffin fraction data. Both the CNDQEM and CNDERM most poorly predict the hydrocarbon selectivity and paraffin fraction data of Run 4 relative to other experimental runs. This finding may indicate that the models are insufficiently sensitive to changes in total pressure, as Run 4 took place at a significantly higher total pressure than Runs 1-3. Changes in the H_2/CO ratio or input rate of the feed stream likely cannot explain the deviation between model and experiment for Run 4, since Runs 1 and 3 took place under a similar range of conditions to Run 4 yet were approximated more closely by the models.

The CNDERM clearly predicts the experimentally observed CO conversions, CO_2 carbon atom selectivities, and hydrocarbon selectivities more accurately than does the CNDQEM model according to MARR values. Despite slightly stronger agreement between the CNDQEM and experimental paraffin fractions, the CNDERM generally computes experimental FT outputs more closely than the CNDQEM. For this reason the empirical rate method was used to derive an expression for θ_{CH2} in the ORM for comparison with the CNDERM.

2.3.2 Comparison of CNDERM and ORM

2.3.2.1 Carbon Monoxide Conversion

Figure 2.6 compares the CO conversions calculated by the CNDERM and ORM. The ORM matches the experimentally reported CO conversions almost exactly for Runs

1 and 4 but deviates from experiment more drastically than the CNDERM for Runs 2 and 3. The two models deviate from experiment by approximately the same relative amount according to MARR averaged across Runs 1-4 (22.8% for the CNDERM, 21.4% for the ORM), but the standard deviation of the individual differences is far larger in the case of the ORM (7.91% for CNDERM, 22.9% for the ORM). For this reason, the CNDERM is a better predictor of experimentally observed CO conversion.

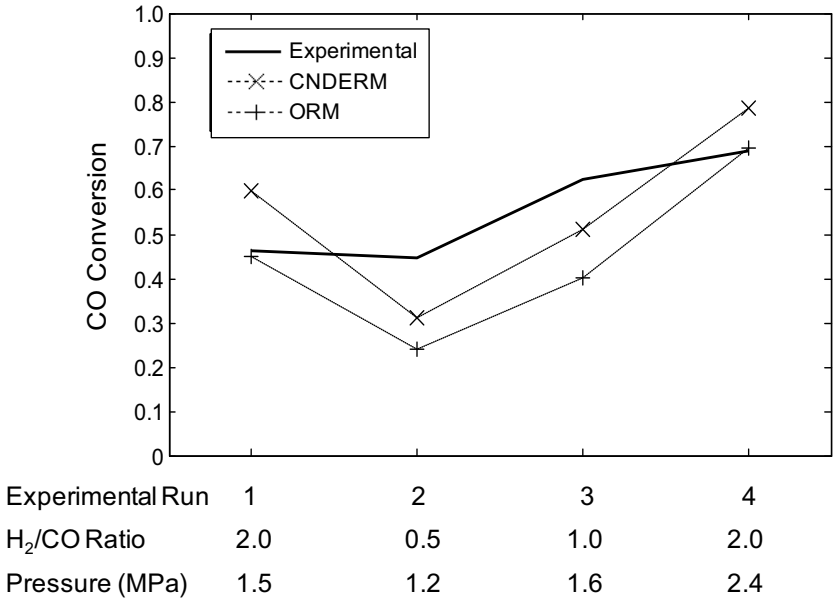

Experimental Run	1	2	3	4
H_2/CO Ratio	2.0	0.5	1.0	2.0
Pressure (MPa)	1.5	1.2	1.6	2.4

Figure 2.6: CO conversion calculated by CNDERM and ORM. Experimental observations of van der Laan and Beenackers included for comparison.

2.3.2.2 Carbon Dioxide Selectivity and Production Rate

The CNDERM and ORM predict nearly identical CO_2 production rates as shown in Figure 2.7. The CO_2 carbon atom selectivity values of the ORM are higher than those of the CNDERM, an expected result given the overall lower CO conversion predicted by the ORM.

The CNDERM and ORM both predict nearly constant CO_2 production rates across all experimental runs, and while they compute different absolute CO_2 carbon atom

selectivity values, the trend across experimental runs is similar between the two. The computational trend of increasing CO_2 carbon atom selectivity with decreasing feed H_2/CO ratio meets intuitive expectations yet represents the opposite of experimental observations.

While the ORM predicts substantially higher CO_2 carbon atom selectivity compared to experimental observations for Run 2, it more precisely computes CO_2 carbon atom selectivity for Runs 3 and 4. However, the CNDERM computes these outputs slightly more precisely when an average of experimental Runs 1-4 is taken into account, driven mostly by the drastic deviation between experiment and ORM for Run 2. Table 2.6 compares the deviation of the two models from experiment with regard to CO_2 carbon atom selectivity and production rate. The MARR values of the two models are almost identical for CO_2 production rate, but the CNDERM shows slightly stronger agreement than the ORM for CO_2 carbon atom selectivity.

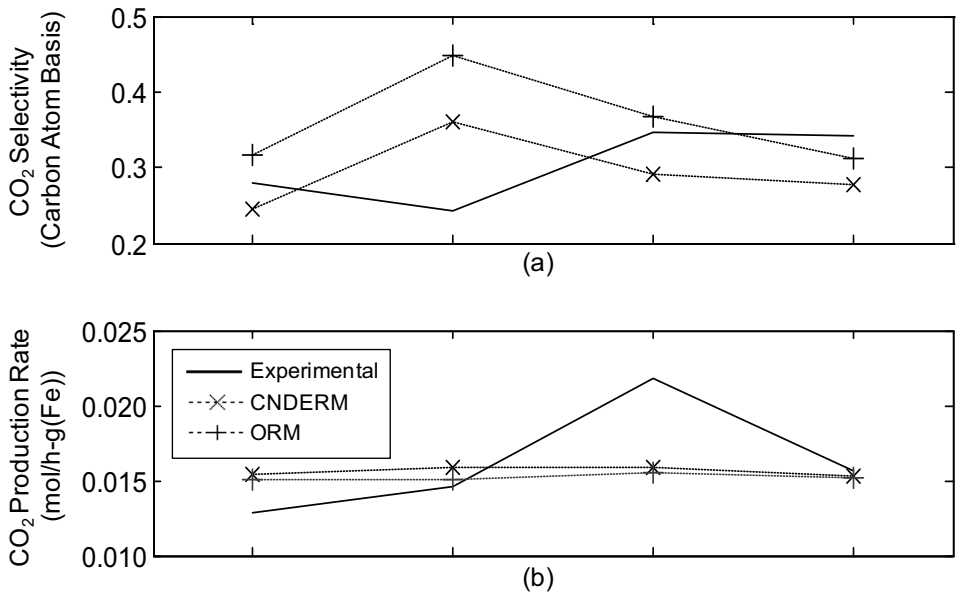

Experimental Run	1	2	3	4
H_2/CO Ratio	2.0	0.5	1.0	2.0
Pressure (MPa)	1.5	1.2	1.6	2.4

Figure 2.7: (a) CO_2 carbon atom selectivity and (b) CO_2 production rate calculated by CNDERM and ORM. Experimental observations of van der Laan and Beenackers included for comparison.

Table 2.6: MARR values (%) for CO_2 carbon atom selectivity and production rate averaged among Runs 1-4. Values shown are relative to experimental observations.

	CNDERM	ORM
CO_2 Selectivity	23.5	28.3
CO_2 Production Rate	14.3	13.0

2.3.2.3 Hydrocarbon Selectivity

Each model was used to compute the selectivity of hydrocarbon species ranging from C_1 to C_{10}, and these selectivities were plotted against experimental observations. Figure 2.8 depicts the results for experimental Runs 1-4.

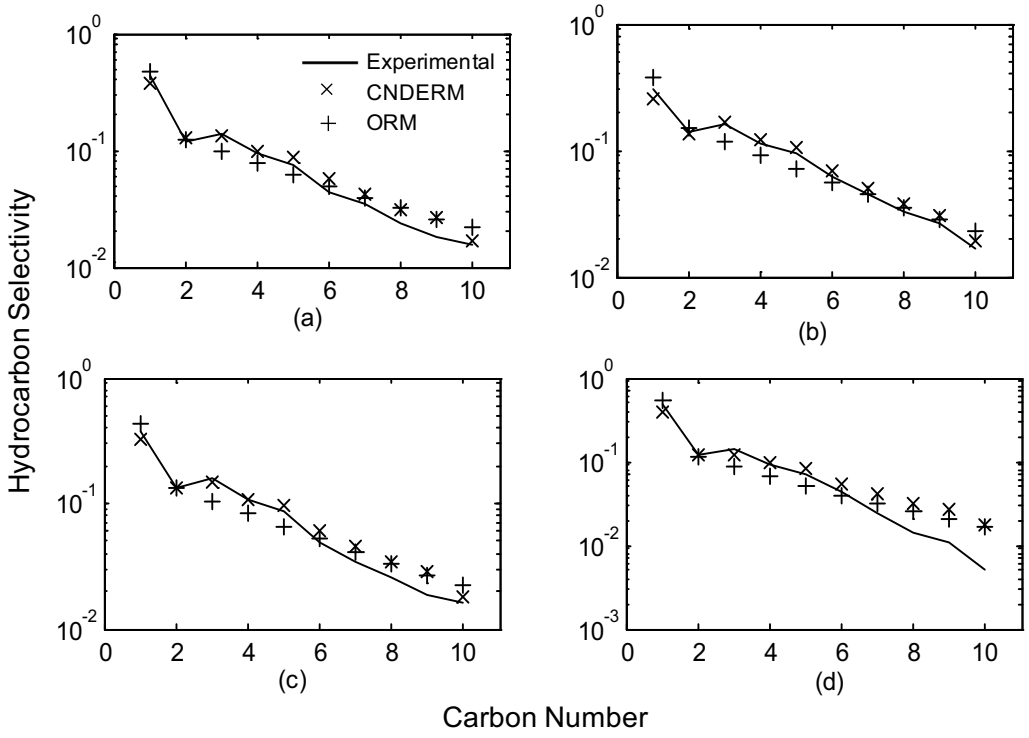

Figure 2.8: Hydrocarbon selectivities calculated by the CNDERM and ORM for the conditions of experimental Runs (a) 1, (b) 2, (c) 3, and (d) 4 [4]. Solid lines represent experimental observations; individual marks represent model predictions.

The adherence of each model to experimentally observed selectivity values resembles that of Section 2.3.1.3, whereby the best agreement between model and experiment is observed for Run 2. Again, this result fits expectations given that the rate constants for each model were derived empirically using experimental data from this run. Both models deviate most from experimental observations for Run 4.

Table 2.7 summarizes the MARR values for both models with regards to hydrocarbon selectivity. The CNDERM has lower MARR values than the ORM for Runs 1-3, indicating stronger agreement with experimental hydrocarbon selectivities for these runs. The CNDERM shows a higher MARR value than the ORM for Run 4,

although both models show wide deviation from experiment under these experimental conditions.

Table 2.7: MARR values (%) for hydrocarbon selectivity averaged among C_1-C_{10} species. Values shown are relative to experimental observations.

Experimental Run	CNDERM	ORM
1	18.5	22.1
2	11.5	15.6
3	18.1	23.6
4	64.3	52.7

The ORM accurately calculates C_2 selectivity but does so at the expense of methane selectivity, which it overpredicts across all runs, and C_3 through C_6, which it underpredicts across all runs. Despite accounting for changes in olefin re-adsorption with carbon number, the model generally predicts a strictly logarithmic relationship between carbon number and the logarithm of hydrocarbon selectivity.

The CNDERM reaches far better agreement with experimental observations than the ORM model, particularly in the C_1 to C_6 range. The model accurately simulates the abnormalities relative to ASF that are observed experimentally for C_2 and C_3 species. Methane selectivity is also accurately predicted, as is the selectivity of C_7-C_{10} hydrocarbons for Runs 1-3. The ORM computes the experimentally observed hydrocarbon selectivities more closely than the CNDERM for Run 4 only, as Table 2.7 shows.

The advantage of the CNDERM in predicting hydrocarbon selectivities resides in its ability to accurately predict deviations from ASF. Of course, this ability was designed into the model by deriving rate constants that change with carbon number, leading to carbon number dependent chain growth probabilities. Any model that relies upon chain

growth probabilities that do not change with carbon number will necessarily output an ASF product distribution. The ORM of van der Laan and Beenackers, replicated in the present study, depends slightly on carbon number to describe olefin re-adsorption effects but otherwise relies on constant chain growth probabilities to describe hydrocarbon selectivity. Section 2.4 further elaborates upon the physical implications of the differences between the two models.

2.3.2.4 Paraffin Fractions

Figure 2.9 depicts a comparison of the paraffin fractions predicted by the CNDERM and ORM. The most glaring shortcoming of the ORM is its inability to accurately predict the abnormally high amount of ethane relative to ethylene. The model published by Fernandes [2] assumes that two distinct reactions – termination of a C_2 surface chain by hydrogen and combination of two surface methyl groups – are responsible for producing ethane. In this fashion he reports good agreement between the calculations of his model and experimental data for C_2 selectivity and paraffin fraction within C_2 species. The CNDERM of the present study predicts the abnormally high ethane fraction by virtue of different rate constants for ethane and ethylene termination reactions. In the absence of experimental evidence in support or contradiction of either regime, an *a priori* determination of the "correct" model is not possible.

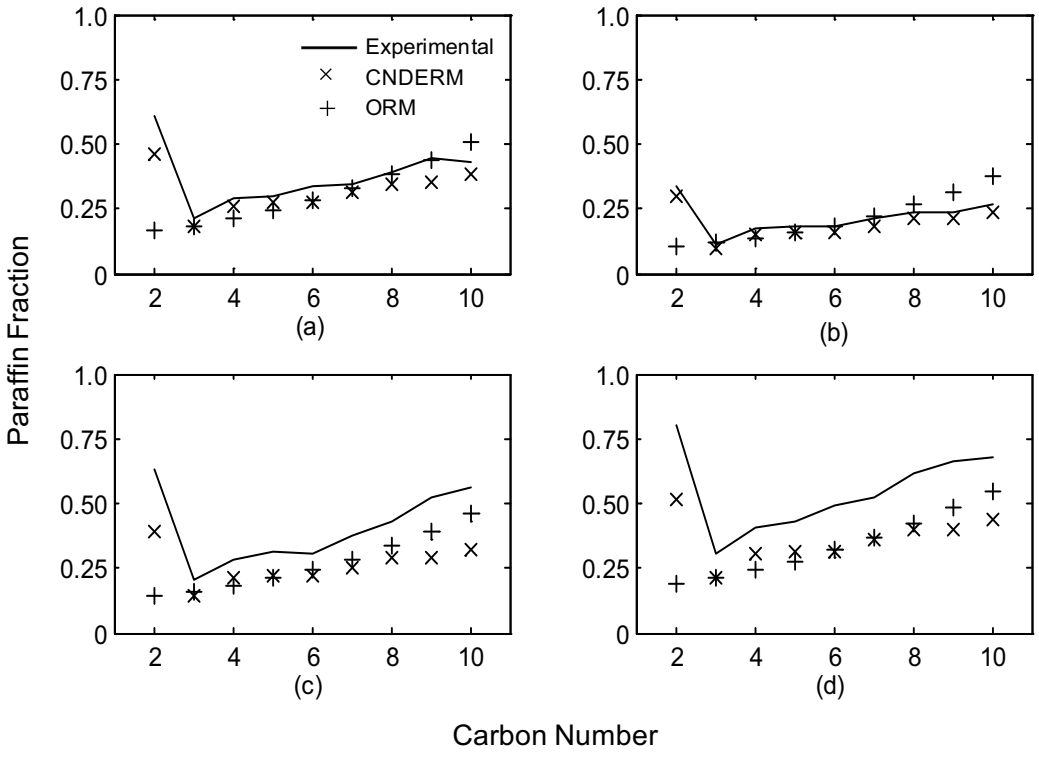

Figure 2.9: Paraffin fractions calculated by the CNDERM and ORM for the conditions of experimental Runs (a) 1, (b) 2, (c) 3, and (d) 4 [4]. Solid lines represent experimental observations; individual marks represent model predictions.

The CNDERM generally computes lower paraffin fractions than were observed experimentally by van der Laan and Beenackers in Runs 1-4. This underprediction was also the case with the ORM for Runs 3 and 4, although the deviation was less drastic for C_8-C_{10} hydrocarbons compared to the CNDERM. For Runs 1 and 2, the rate of increase in paraffin fraction from C_3 to C_{10} is larger as predicted by the ORM than was observed experimentally.

Table 2.8 summarizes MARR values for the models with regard to paraffin fraction. Much of the discrepancy between the ORM and experiment can be attributed to the difference in C_2 paraffin fraction, and as a result the CNDERM has lower MARR

values than the ORM for paraffin fraction data. However, the ORM exhibits residuals slightly better than the CND model for Run 3.

Table 2.8: MARR values (%) for paraffin fraction averaged among C_2-C_{10} species. Values shown are relative to experimental observations.

Experimental Run	CNDERM	ORM
1	14.5	19.2
2	12.2	21.8
3	33.9	30.7
4	32.9	36.1

2.3.2.5 Summary

Similar patterns of adherence to the observations of experimental Runs 1-4 were observed in the comparison between the CNDERM and ORM as were observed in the comparison between the CNDQEM and CNDERM with regards to hydrocarbon selectivity and paraffin fractions. The largest deviation between model and experiment was observed for Run 4 with the best agreement occurring for Run 2. The CNDERM and ORM each achieved differing degrees of success when predicting CO conversion, although both generally mimicked the experimental trend observed across Runs 1-4. The models calculated similar CO_2 production rates to each other and across experimental runs, with the ORM exhibiting higher CO_2 carbon atom selectivity than the CNDERM due to lower predicted CO conversion.

The CNDERM approximates the selectivity and paraffin fraction of lighter hydrocarbons more precisely than does the ORM. The ability of the CNDERM to predict the abnormally low C_2 selectivity and abnormally high C_2 paraffin fraction that are characteristic of experimental FT product distributions represents the most notable difference in the performance of the two models. Experimental methane and C_3-C_6

selectivity are also computed more precisely by the CNDERM for Runs 1-4, as the ORM computes hydrocarbon selectivity plots that generally adhere to ASF.

2.4 Conclusions

The present study develops an FT reaction model using carbon number dependent rate constants to describe propagation and termination steps. The first part of this analysis examines two methods by which FT reactants may be converted into reactive surface species. The CNDQEM assumes the reactants to be in quasi-equilibrium with their respective surface species; the rate of reaction is then limited by the consumption of methylene monomers. The CNDERM assumes the production of monomers to be rate limiting and uses a well established empirical FT rate law to describe their appearance. The CNDQEM shows slightly stronger agreement than the CNDERM with respect to experimental paraffin fractions, but the CNDERM more accurately predicts experimental CO conversion, CO_2 selectivity, and hydrocarbon selectivities. For this reason the empirical rate method is used to describe reactant dissociation in the ORM for comparison with the CNDERM.

The CNDERM calculates higher CO conversions and lower CO_2 selectivities than the ORM under the same reaction conditions, and it more accurately predicts experimental C_1-C_6 hydrocarbon selectivities. The hydrocarbon selectivities of the ORM appear to adhere to the ASF distribution, whereby a plot of molar hydrocarbon selectivity against carbon number yields a linear plot. Moreover, the ORM does not account for the abnormally high paraffin fraction that is experimentally observed within C_2 species.

The current study reveals the possibility that chain length dependence on propagation and termination reactions may partially explain experimental deviations from ASF, despite the findings of previous reaction modeling studies that olefinic re-adsorption alone explains these deviations. The analysis of the present study demonstrates that a model based only upon olefinic re-adsorption cannot accurately describe experimental FT product distributions.

The experimental evidence in support of olefinic re-adsorption largely relies on studies that co-fed olefins into an FT reactor to determine the extent to which they undergo further chain growth. If equilibrium exists between desorbed olefins and adsorbed hydrocarbon chains, then co-feeding olefins will artificially force this equilibrium in favor of the adsorbed chains and increase the rate of re-adsorbed hydrocarbon chain growth. It is obvious that olefins are chemically active, but the way in which olefins have been co-fed may exaggerate their effect on intrinsic FT product distributions. This dissertation does not seek to discount the effect of re-adsorbed olefins on FT product distributions completely – the work presented in Chapter Three is explained partly by olefinic re-adsorption in conjunction with bed residence times – but only to question its sole responsibility for ASF deviations.

While the CNDERM appears to outperform the ORM in certain aspects of FT, care must be taken to avoid faulty conclusions about the nature of the FT reaction mechanism based on this finding. Agreement between model calculations and experimental data does not necessarily confirm model validity. Furthermore, a model based on Langmuir-Hinshelwood kinetics gives no information concerning the conformational configurations of surface bound hydrocarbon chains. Such information is

necessary to confirm the earthworm model put forth in Figure 2.1. Further modeling work must be performed to determine the path followed by a growing hydrocarbon chain. These computations must take into account the physical forces and steric effects that may interfere with propagation and termination steps in FT.

References

1. B. Teng et al., App. Catal. A 301 (2006) 39-50.

2. F. Fernandes, Chem. Eng. Technol. 28 (2005) 930-938.

3. L. Nowicki et al., Chem. Eng. Sci. 56 (2001) 1175-1180.

4. G. van der Laan, A. Beenackers, Ind. Eng. Chem. Res. 38 (1999) 1277-1290.

5. W. Zimmerman, D. Bukur, S. Ledakowicz, Chem. Eng. Sci. 47 (1992) 2707-2712.

6. H. Schulz, M. Claeys, App. Catal. A 186 (1999) 91-107.

7. E. Iglesia, S. Reyes, R. Madon in: D. Eley, H. Pines, P. Weisz (Eds.), Advances in Catalysis Volume 39, Academic Press, San Diego, 1993, p. 227.

8. R. Anderson in: P. Emmet (Ed.), Catalysis Vol. IV, Reinhold, New York, 1956, p. 297.

9. M. Dry, Ind. Eng. Chem. Prod. Res. Dev. 15 (1976) 282-286.

10. K. Rao et al., Topics in Catal. 2 (1995) 71-78.

11. M. Dry in: J. Anderson and M. Boudart (Eds.), Catalysis Science and Technology Vol. 1, Springer Verlag, Berlin, 1981, p. 196.

12. A. Raje, B. Davis, Catal. Today 36 (1997) 335-345.

13. B. Teng et al., Fuel 84 (2005) 917-926.

14. E. van Steen, H. Schulz, App. Catal. A 186 (1999) 309-320.

15. E. Iglesia, S. Reyes, R. Madon, J. Catal. 129 (1991) 238-256.

Chapter Three

The Effect of Distributed Syngas Feeding on Fischer-Tropsch Product Distributions – Part 1

3.1 Introduction

The current chapter examines the effect of a distributed syngas feeding strategy on FT product distributions. This work represents a furtherance of the previously discussed studies of Sharifnia et al. [1] and Guillou et al. [2] in which a distributed hydrogen feeding strategy over cobalt catalysts was followed. While these groups found improvements to C_{5+} selectivity for certain hydrogen feeding configurations, the practical industrial applicability of this strategy is limited by the difficulty and expense of attaining pure hydrogen. Implementation of a distributed syngas feeding strategy in an FT plant would necessitate only simple splitting of the inlet syngas feed.

The experiments performed in this chapter employ a two-stage reactor system using two series FT reactors loaded with precipitated iron catalyst. The first portion of the study examines the array of product distributions that result when syngas flow to the entrance of the first FT reactor is held constant and when the H_2/CO ratio of the syngas fed at the entrance of the second reactor is varied. The second portion of this study compares product distributions resulting from this distributed feeding strategy to those that occur during normal FT plug flow operation.

The hypothesis underlying this work maintains that exposing products from a first FT reactor to fresh synthesis gas would cause concentration profiles not achieved during normal FT operation through plug flow reactors. Olefinic products formed in the first reactor, thusly exposed to fresh syngas and presumably higher concentrations of methylene monomers, would undergo re-adsorptive growth at a higher probability than normal within a second FT reactor. This mechanism of re-adsorption and further chain growth has been supported by the work of Iglesia, Kuipers, and Schulz [3-5].

3.2 Experimental

3.2.1 Catalyst Synthesis

A silica supported, precipitated iron catalyst was prepared by first precipitating a 13.8 wt.% solution of iron (III) nitrate nonahydrate at 80°C with a 9.1 wt.% solution of sodium carbonate monohydrate at 80°C until the pH of the well mixed suspension reached approximately 9.0. The suspension was allowed to cool and then was filtered over a vacuum in a Buchner funnel and rinsed with deionized water. The wet precipitate mass was returned to suspension in deionized water (5 mL for every gram of $Fe(NO_3)_3 \bullet 9H_2O$ used), and tetraethyl orthosilicate was added (0.33 mL for every gram of $Fe_3(NO_3)_3 \bullet 9H_2O$ used). This suspension was stirred vigorously for two hours at room temperature and then filtered again over a vacuum in a Buchner funnel while rinsing again with of deionized water. The wet precipitate mass was put into a 100°C oven for twelve hours to dry, followed by calcination in a 400°C oven for four hours. Finally, the catalyst was crushed to 60-80 mesh size (0.074 to 0.25 mm diameter), physically blended with two times its volume of 60-200 mesh silica gel (approximately 1.0 g silica gel for

every 1.5 g of catalyst), and reduced at 300°C at 55 psia (0.38 MPa) for 24 hours in 200 sccm H_2.

3.2.2 Distributed Syngas Feeding Experiments

Figure 3.1 depicts the experimental apparatus used for these experiments. Carbon monoxide and hydrogen were fed with nitrogen as an inert standard (not depicted in Figure 3.1) through mass flow controllers (MKS Instruments, M100B Series) into fixed bed reactors. The reactor tubes were comprised of 316 stainless steel with outer diameter of 3/4" and 0.065" wall thickness and were housed in vertical split tube furnaces (Applied Test Systems, Series 3210). All other lines in the reactor system were made of 1/4" outer diameter 316 stainless steel. The reactor effluent stream was fed into a gas chromatograph (Varian, Model CP-3800) equipped with one thermal conductivity detector for quantification of N_2, CO, and CO_2; one thermal conductivity detector for quantification of H_2; and a flame ionization detector for quantification of hydrocarbons through C_{15}. Appendix B gives further details regarding analytical methods.

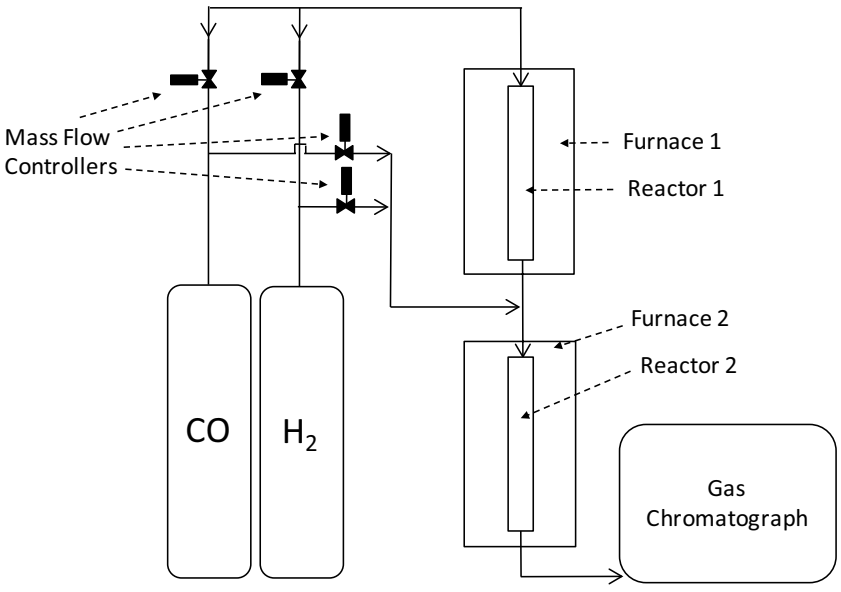

Figure 3.1: Depiction of experimental system.

All lines carrying FT products were heated to 205°C and insulated with fiber glass in order to prevent condensation of heavier products. Antoine's equations were used to ensure that the resulting concentrations of all hydrocarbons were below their respective dew point concentrations.

Each reactor was maintained at a temperature of 250°C and a pressure of 135 psia (0.93 MPa) and was loaded with 3.0 g of catalyst blended physically with 2.0 g of silica gel set atop a plug of fine quartz wool. The approximate volume of each catalyst bed was 9.0 mL; pressure drop across the beds was negligible and did not affect experimental results.

The flow of reactant gases to the first reactor was maintained at 20 sccm CO, 50 sccm H_2, and 20 sccm N_2, yielding a molar H_2/CO ratio of 2.5 and a catalyst weight to molar flow (W/F) value of 12.4 g·h/mol. Flows to the second reactor for each experimental case are given in Table 3.1. Each experimental case will be referred to hereafter by the H_2/CO ratio of the synthesis gas fed to the second reactor ("the 3.0 H_2/CO case," "the 2.0 H_2/CO case," etc.). The W/F values and residence times calculated in Table 3.1 take into account the product stream exiting the first reactor as well as the fresh synthesis gas feed.

Table 3.1: Flowrates and residence times in Reactor 2.

H_2/CO Ratio of Syngas fed into	Fresh Syngas Flowrates (sccm of CO/H_2)	W/F value (g·h/mol)	Residence Time (s)
None (single reactor)	–	–	–
3.0	20/60	6.59	3.2
2.0	20/40	7.47	3.6
1.0	20/20	8.62	4.2
0.5	20/10	9.34	4.5

After the catalyst had been reduced as described in Section 3.2.1, the reactant gases were fed to the system for 24 hours to ensure the catalyst was running at steady state. Selectivity data for hydrocarbons up to C_{15} were then gathered for another 24 hours.

As part of the present study, it was desired to compare the effects of the previously described experiments with results obtained when all synthesis gas was simply fed into the entrance of the first reactor, hereafter referred to as the normal syngas feeding regimes. This comparison was performed against the results of the distributed feeding regime for the 1.0 and 2.0 H_2/CO cases. Table 3.2 compares the flow conditions of the distributed and normal syngas feeding regimes; all other experimental conditions (catalyst weight, temperature, pressure) remained identical.

Table 3.2: Flowrates for distributed and normal syngas feeding regimes.

		Distributed Regime		Normal Regime	
H_2/CO Case	Species	Flowrates to Reactor 1 (sccm)	Flowrates to Reactor 2 (sccm)	Flowrates to Reactor 1 (sccm)	Flowrates to Reactor 2 (sccm)
2.0	CO	20	20	40	0
	H_2	50	40	90	0
	N_2	20	0	20	0
1.0	CO	20	20	40	0
	H_2	50	20	70	0
	N_2	20	0	20	0

The experiments conducted under the normal syngas feeding regime were named according to the corresponding experiments of the distributed feeding regime. As can be seen from the flowrates in Table 3.2, the inlet H_2/CO ratios for the 2.0 and 1.0 cases of

the normal feeding regime were 2.25 and 1.75 respectively. As with the experiments conducted under the distributed syngas feeding regime, a 24-hour catalyst pre-reduction period preceded the 24-hour data collection period.

3.3 Results and Discussion

3.3.1 Single Reactor Experiment

An experiment conducted with a single reactor was performed to characterize the effluent exiting the first reactor in the distributed syngas feeding experiments. The flow of reactant gases into the single reactor was identical to the flow into the first series reactor as described in the Experimental section (2.5 H_2/CO ratio, 50 sccm H_2, 20 sccm CO). The conversion of carbon monoxide exiting this reactor was approximately 95%. Table 3.3 depicts the carbon atom selectivity of the products and the molar concentrations of all species exiting this reactor.

Table 3.3: Carbon atom selectivity of products and effluent concentrations exiting Reactor 1 in the single reactor case.

Species	Single Reactor Selectivity (%, carbon atom basis)	Effluent Concentration (%, molar basis)
CO_2	49.9	13.8
Methane	14.2	5.96
C_2-C_3 Hydrocarbons	21.5	2.87
C_4-C_6 Hydrocarbons	9.27	0.76
C_7-C_{10} Hydrocarbons	3.93	0.16
C_{11}-C_{15} Hydrocarbons	1.34	0.036
H_2	–	42.1
CO	–	2.36
H_2O	–	2.85
N_2	–	29.2

3.3.2 Distributed Syngas Feeding Experiments

3.3.2.1 Carbon Monoxide Conversion

During the distributed feeding experiments, synthesis gas with four different H_2/CO ratios (3.0, 2.0, 1.0, 0.5) was fed into the entrance of the second reactor with the products from the first reactor (quantified in Table 3.3). Figure 3.2 shows CO conversion against time on stream for each experimental case.

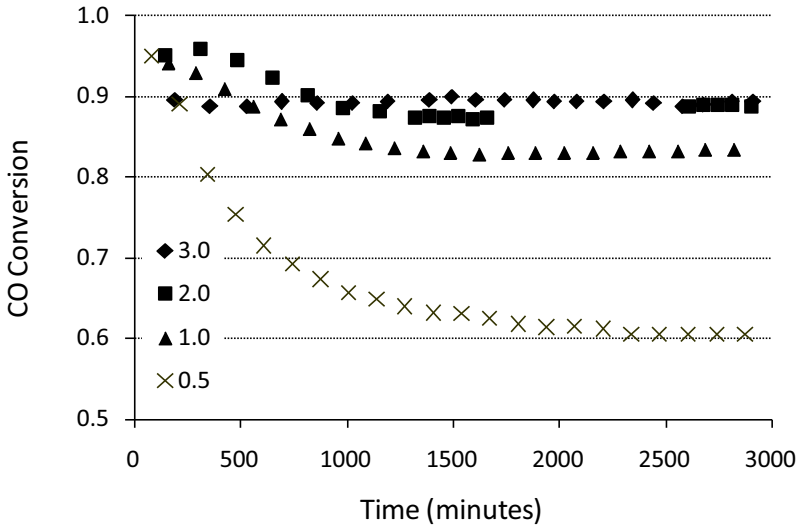

Figure 3.2: CO conversion against time on stream. The ratios in the legend refer to the H_2/CO ratio of the synthesis gas fed at the entrance of the second reactor.

CO conversion after 48 hours remained roughly the same (between 83% and 90%) for downstream synthesis gas mixtures with H_2/CO ratios as low as 1.0. However, CO conversion dropped to approximately 60% when syngas with an H_2/CO ratio of 0.5 was fed into the entrance of Reactor 2.

Two competing factors controlled the extent of CO conversion: the H_2/CO ratio of the inlet syngas and the bed residence time in Reactor 2. Lower H_2/CO ratios lead to lower overall CO conversions over iron (and other) FT catalysts due to the decrease in the FT reaction rate with decreasing hydrogen partial pressure [6,7]. Conversely, higher

bed residence times generally lead to higher conversion for any catalyzed reaction. During these experiments, the H_2/CO ratio of the Reactor 2 inlet syngas was reduced by lowering the H_2 flowrate of hydrogen while keeping CO flowrate constant. As a result, bed residence time in Reactor 2 increased as the H_2/CO ratio of the Reactor 2 inlet syngas decreased.

The H_2/CO ratio in the Reactor 2 inlet syngas appears to have been the driving force behind the experimental trends observed in CO conversion, as it decreased drastically when the H_2/CO ratio fell below unity. Bed residence times were kept within a relatively close range by the additional presence of the product stream from Reactor 1. Therefore, the low partial pressure of hydrogen in the 0.5 H_2/CO case led to a decreased overall FT rate in Reactor 2, causing markedly lower conversion

The CO conversion exiting Reactor 1 was higher than the overall CO conversion exiting Reactor 2 for any of the distributed feeding cases. This observation could be attributed to two factors: longer bed residence time and higher concentration of reactants in Reactor 1. The products fed to the second reactor acted to both increase the bulk velocity and dilute the concentrations of FT reactants in Reactor 2, leading to lower conversion through this reactor than was observed through Reactor 1.

Some decrease in catalyst activity was observed for each experimental case. CO conversion exiting Reactor 2 began at approximately 95% and then steadily decreased during the first 1500 minutes on stream, reaching a constant level thereafter. The decrease in activity most likely can be attributed to a change in the catalyst phase from elemental iron to an iron carbide species, as has been reported in the literature [8]. Iron FT catalysts also exhibit some loss in surface area when they are initially exposed to

reaction conditions, a phenomenon which is arrested by the presence of the silica support. These effects were believed to be consistent among experimental cases, and differences in steady state CO conversion levels exiting Reactor 2 can be explained mostly according to the relative partial pressures of hydrogen present in the Reactor 2 inlet syngas.

3.3.2.2 Product Selectivity

Carbon Dioxide

Iron FT catalysts are known to have simultaneous water-gas shift activity. In industrial FT applications, CO_2 is often treated as a reactant due to its presence in syngas and its ability to be consumed by the reverse water-gas shift reaction [9]. For the purposes of this study, for which CO_2-free syngas was used, CO_2 was treated as a product.

Figure 3.3 compares the CO_2 carbon atom selectivity for each experimental case, which increases from approximately 43% in the 3.0 H_2/CO case to almost 50% in the 0.5 H_2/CO case. This observation is in agreement with the slurry reactor study of Raje and Davis, who found that as the H_2/CO ratio of the inlet syngas was decreased from 1.7 to 0.67, the selectivity of CO_2 drastically increased [7]. This trend correlates with the expected yield of CO_2; as the downstream synthesis gas becomes increasingly hydrogen deficient, the water gas shift reaction is forced toward its products, resulting in the production of more CO_2. The subsequent consumption of hydrogen by FT sustains the driving force of the water-gas shift reaction towards it products.

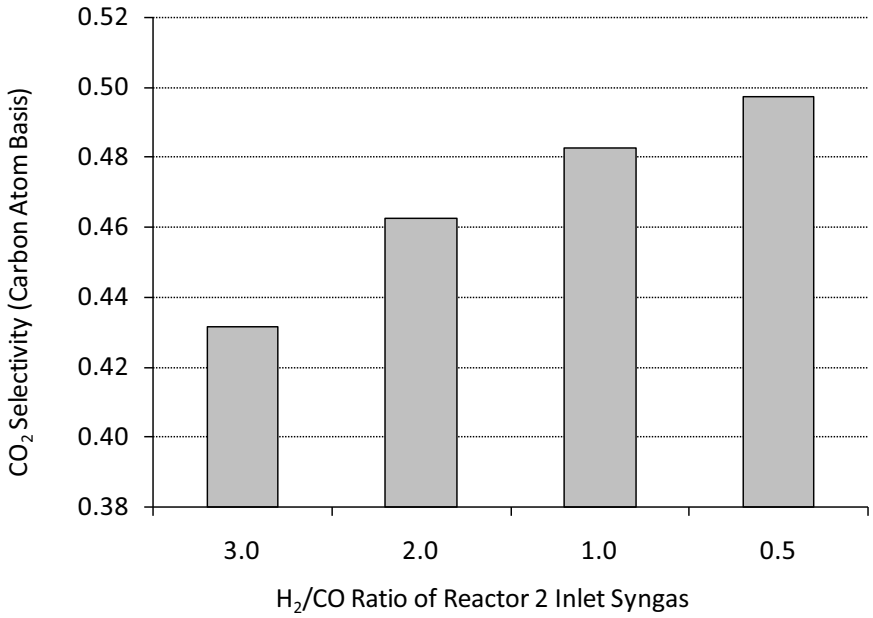

Figure 3.3: CO_2 carbon atom selectivity of the Reactor 2 effluent in the distributed syngas feeding experiments.

The product distribution exiting Reactor 1 was more selective to CO_2 (49.9%, carbon atom basis) than the distributions exiting Reactor 2 for each case of the distributed feeding experiments. The feed entering the second reactor was closer to water-gas shift equilibrium than that entering the first, resulting in a slower water-gas shift rate in Reactor 2 and therefore lower CO_2 production compared to FT products.

Hydrocarbon Species

Table 3.4 summarizes the carbon atom selectivity of different hydrocarbon ranges for each downstream feeding case. As the partial pressure of hydrogen in the downstream synthesis gas decreased, methane selectivity decreased while the selectivity of C_{5+} hydrocarbons increased. The most drastic increase was observed in the C_{11}-C_{15} range, the selectivity of which increased by over six times by decreasing the H_2/CO ratio of the Reactor 2 inlet syngas. These findings agree with previous experimental trends

observed over FT catalysts in general, including iron [10], cobalt [11], and ruthenium [12]. Higher H_2/CO ratios favor the formation of lighter hydrocarbons due to the increased likelihood of hydrocarbon chain termination by hydrogen on the surface of the catalyst [13].

Table 3.4: Carbon atom selectivity of hydrocarbon products for each experimental case, in percentages.

Experimental Case	Methane	$C_2 - C_3$	$C_4 - C_6$	$C_7 - C_{10}$	$C_{11} - C_{15}$	C_{5+}
3.0	35.0	18.0	3.20	.629	.0758	1.83
2.0	28.4	19.3	4.71	1.11	.264	3.17
1.0	26.8	18.6	4.78	1.20	.374	3.46
0.5	23.8	19.1	5.39	1.48	.482	4.08

Product distribution plots are shown in Figure 3.4 with the single reactor product distribution included for comparison. For the purpose of finding the chain growth probabilities of the distributions, a distinct line was fit to the selectivity data for C_1-C_5 hydrocarbons and C_6-C_{15} hydrocarbons of each experimental case. Such double-α models have been used in the literature where a break exists in the conventional ASF plot [14]. The α-values of the present study are reported in Table 3.5; the single reactor values are included for comparison. A negative deviation from the linear ASF plot was observed at C_2, agreeing with the findings of previous studies [7,15], and slight positive deviations from ASF were observed at hydrocarbon numbers above twelve. Chain growth probability increased slightly as the H_2/CO ratio was decreased from 3.0 to 0.5 with the largest increase observed between the 3.0 and 2.0 H_2/CO cases.

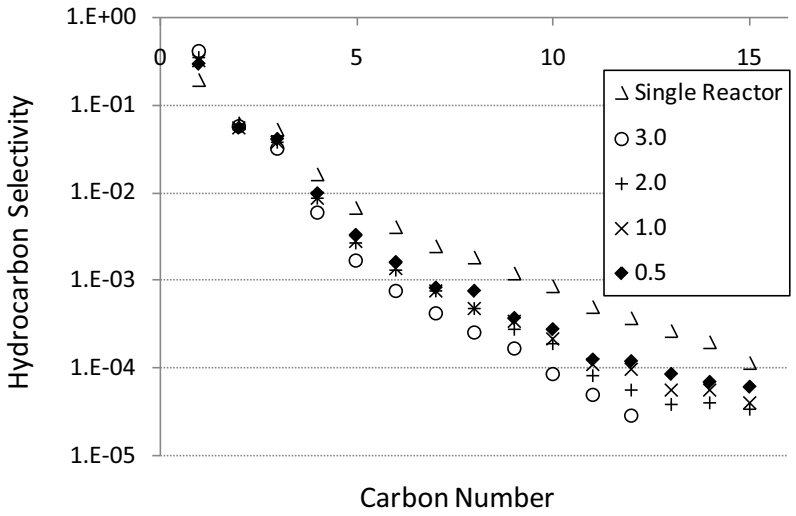

Figure 3.4: ASF plots depicting the natural logarithm of hydrocarbon selectivity versus carbon number. The legend refers to the H_2/CO ratio of the syngas fed into the entrance of Reactor 2 in the distributed syngas feeding experiments.

Table 3.5: α-values for each experimental case of the distributed syngas feeding experiments. A double-α model was used in which C_1-C_5 selectivities were used to derive α_1 and C_6-C_{15} selectivities were used to derive α_2.

Experimental Case	α_1 (C_1-C_5)	α_2 ($C_6 - C_{15}$)
Single Reactor	0.45	0.68
3.0	0.27	0.58
2.0	0.31	0.65
1.0	0.32	0.67
0.5	0.34	0.69

Comparison with the single reactor case reveals the effect on FT product distributions when a secondary synthesis gas feed stream is added to the effluent of an upstream reactor. Figure 3.4 demonstrates that the product distributions exiting Reactor 2 were significantly less selective towards heavier hydrocarbons than the product distribution exiting Reactor 1. Two main factors were responsible for these results: differences in bed residence time between the two reactors and the effect of both FT and the water-gas shift reaction on H_2/CO ratios along the reaction axis of the catalyst bed.

- *Bed Residence Times:* Longer bed residence times are associated with heavier hydrocarbon product distributions due to the increased likelihood that olefins will be readsorbed onto the catalyst surface, undergo further chain growth, and desorb as paraffins via hydrogenation [3]. The current studies were run such that Reactor 1 experienced a significantly higher residence time (6.0 seconds) than Reactor 2 (3.2, 3.6, 4.2, and 4.5 seconds for the 3.0, 2.0, 1.0, and 0.5 H_2/CO cases, respectively), mainly due to the additional presence of Reactor 1 products in the Reactor 2 feed. Primarily formed olefins in Reactor 1 had more opportunity to be re-adsorbed at the catalyst surface and undergo further hydrocarbon chain growth, resulting in a heavier product distribution. The paraffin fraction of the products, depicted in Figure 3.5, supports this explanation as the products exiting Reactor 1 exhibit a higher paraffin fraction (and thus lower olefin content) than any of the downstream synthesis gas feeding cases.

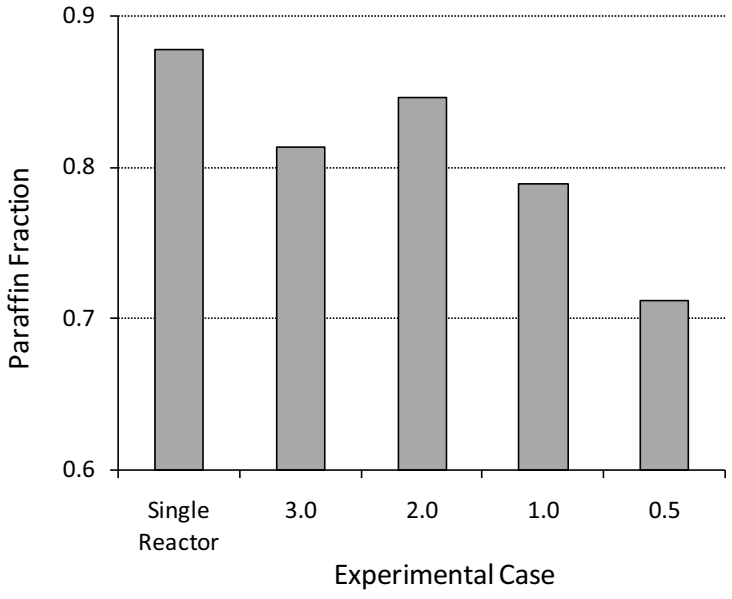

Figure 3.5: Paraffin fraction of hydrocarbon species C_2-C_{15} in the effluent of Reactor 2.

- *H_2/CO Ratios:* FT and the water-gas shift reaction occur simultaneously over iron catalysts. Hydrogen is consumed by FT but produced by the water-gas shift reaction, whereas CO is consumed by both reactions. Water-gas shift equilibrium at the reaction temperature heavily favors its products, H_2 and CO_2 ($K_{eq} = 86.8$). Therefore, as the CO partial pressure decreases along the catalyst bed, the partial pressure of hydrogen remains relatively constant. The H_2/CO ratio increases over the length of a fixed bed reactor as a result, and this ratio increases with CO conversion.

Due to almost complete CO conversion, the Reactor 1 effluent contained an abundance of hydrogen relative to unreacted CO (see Table 3.3). The total H_2/CO ratio fed to Reactor 2 was therefore higher than it would have been had fresh syngas alone been fed to it, and the higher H_2/CO ratios favored the formation of lighter hydrocarbons. Table 3.6 summarizes the H_2/CO ratios entering Reactor 2 for each experimental case; for the 3.0 and 2.0 H_2/CO cases, these ratios were higher than those entering Reactor 1.

Table 3.6: H_2/CO ratios entering Reactor 2, accounting for both fresh syngas and remaining hydrogen and carbon monoxide exiting Reactor 1.

Experimental Case	H_2/CO Ratio
3.0	4.1
2.0	3.2
1.0	2.3
0.5	1.8

3.3.3 Comparison of Distributed and Normal Syngas Feeding Regimes

Table 3.7 compares the CO conversion and carbon atom selectivity of hydrocarbon products for corresponding cases of the distributed and normal syngas feeding regimes. Methane selectivity was significantly lower in each experimental case

of the normal feeding regime, and the selectivity of C_{5+} hydrocarbons was approximately three times higher in the normal feeding regime for both the 2.0 and 1.0 H_2/CO cases. CO conversion was also higher in both cases of the normal regime as compared to the corresponding cases of the distributed regime.

Table 3.7: Comparison of CO conversion and carbon atom selectivity for hydrocarbon products between distributed and normal syngas feeding regimes.

Experimental Case/Syngas Feeding Regime		CO Conv.	Carbon Atom Selectivity of Hydrocarbons (%)					
			Methane	$C_2 - C_3$	$C_4 - C_6$	$C_7 - C_{10}$	$C_{11} - C_{15}$	C_{5+}
2.0	Distributed	0.89	28.4	19.3	4.71	1.11	.264	3.17
	Normal	0.94	21.2	18.3	6.32	2.80	3.06	8.66
1.0	Distributed	0.83	26.8	18.6	4.78	1.20	.374	3.46
	Normal	0.92	19.2	18.8	6.72	3.32	3.27	9.62

Differences in conversion can be attributed mainly to bed residence times, whereas differences in selectivity can be attributed to bed residence times and H_2/CO ratio along the axes of the reactors. These factors are explained in subsequent sections.

3.3.3.1 Carbon Monoxide Conversion

The bed residence times in Reactor 2 were approximately the same for corresponding cases of the distributed and normal regimes. The bed residence time in Reactor 1 was shorter in the experiments of the normal feeding regime since all syngas was fed into the Reactor 1 entrance. However, half of the CO fed to the system in the experiments of the distributed feeding regime had no contact time with the catalyst bed in Reactor 1. Lower overall catalyst contact time was the primary factor contributing to the lower observed CO conversion in the experiments of the distributed feeding regime.

3.3.3.2 Product Selectivity

Differences in bed residence time between the normal and distributed feeding regimes affected product selectivity as well as CO conversion. The increased CO catalyst contact time in the normal feeding regime allowed greater opportunity for primarily formed olefins to be re-adsorbed onto the catalyst surface, undergo further chain growth, and desorb as paraffins. This explanation is supported by the higher C_2-C_{15} paraffin fractions observed for under the normal syngas feeding regime (Figure 3.6).

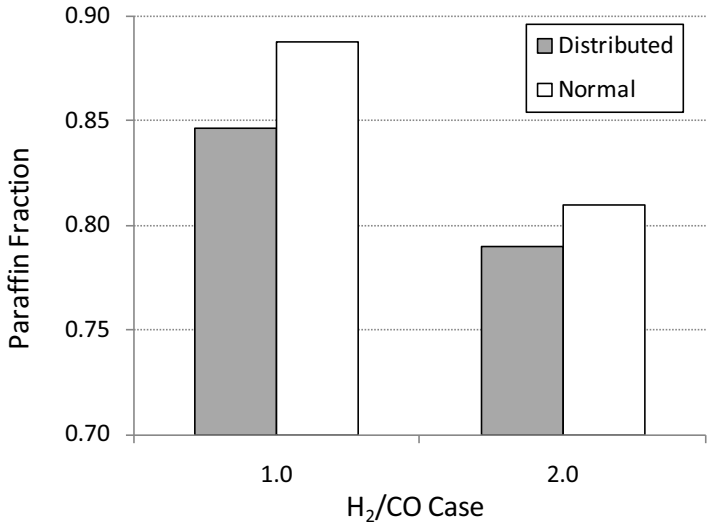

Figure 3.6: Comparison of paraffin fractions for C_2-C_{15} hydrocarbon products between corresponding H_2/CO cases of the distributed and normal syngas feeding regimes.

Differences in H_2/CO ratios between the two syngas feeding regimes also explain the greater selectivity toward heavier hydrocarbons observed for the top feeding cases. In the distributed syngas feeding experiments, an abundance of hydrogen entered Reactor 2 due to simultaneous water-gas shift activity, as was previously described. In experiments of the normal feeding regime, all reactants were fed together into the entrance of Reactor 1; the overall H_2/CO ratio remained lower along the reaction axis, leading to the formation of heavier products as compared to those generated under the distributed

feeding regime. Table 3.8 summarizes the H_2/CO ratios for each syngas feeding regime where syngas was added to the system (at the entrance of both Reactors 1 and 2 for the distributed regime, at the entrance of Reactor 1 for the normal regime).

Table 3.8: Comparison of H_2/CO between the normal and distributed feeding regimes at locations where syngas was added to the reactor system.

Experimental Case/Syngas Feeding Regime		H_2/CO Ratio at Reactor 1 Entrance	H_2/CO Ratio at Reactor 2 Entrance
2.0	Distributed	2.50	3.2
	Normal	2.25	–
1.0	Distributed	2.50	2.3
	Normal	1.75	–

3.4 Conclusions

In an effort to increase the selectivity of the Fischer-Tropsch synthesis toward C_{5+} hydrocarbons, fresh syngas was fed into the entrances of two series fixed bed reactors fitted with beds of precipitated iron catalyst. These experiments were performed under the hypothesis that the interaction of a primarily formed FT product distribution with fresh syngas would create concentration profiles not experienced during normal FT fixed bed operation. It was believed that such interaction would include the re-adsorption and further chain growth of olefins in the second reactor upon exposure to the downstream syngas feed. However, the results of these experiments showed that C_{5+} selectivity decreased by over 60% when compared to product distributions of the normal feeding regime.

The bed residence time in Reactor 1 of the distributed regime experiments allowed for almost complete CO conversion, leading to an abundance of hydrogen at the

entrance of Reactor 2 due to the influence of the water-gas shift reaction. The resulting higher H_2/CO ratios in Reactor 2 yielded lighter overall product distributions. It is clear that effecting complete CO conversion in a distributed fashion is counterproductive in the endeavor to create heavier FT product distributions.

The insights gained from these experiments suggest a different strategy that may improve the results of this approach. Reducing the amount of catalyst in the first reactor would lead to a decrease in the amount of hydrogen entering Reactor 2, generating conditions more favorable to the formation of heavier hydrocarbons in the experiments of the distributed feeding regime. Higher catalyst loading in Reactor 2 should provide more complete CO conversion while increasing the likelihood of primarily formed olefins originating from both reactors undergoing further chain growth subsequent to re-adsorption. Finally, since hydrogen-rich inlet syngas serves only to increase yield of methane and other light hydrocarbons, the use of syngas with H_2/CO ratios above 2.0 should be avoided in favor of CO-rich syngas.

References

1. S. Sharifnia et al., Fuel Proc. Technol. 86 (2005) 1253-1264.

2. L. Guillou et al., Chem. Eng. Journal 136 (2008) 66-76.

3. E. Iglesia et al., Advances in Catal. 39 (1993) 221-302.

4. E. Kuipers et al., J. Catal. 158 (1996) 288-300.

5. H. Schulz, M. Claeys, App. Catal. A 186 (1999) 71-90.

6. M. Dry, Ind. Eng. Chem. Prod. Res. Develop. 15 (1976) 282-286.

7. A. Raje, B. Davis, Catal. Today 36 (1997) 335-345.

8. M. Claeys, E. van Steen in: A. Steynberg, M. Dry (Eds.), Fischer-Tropsch Technology, Elsevier, Amsterdam, 2004, p. 555-557.

9. M. Claeys, E. van Steen in: A. Steynberg, M. Dry (Eds.), Fischer-Tropsch Technology, Elsevier, Amsterdam, 2004, p. 197.

10. M. Dry in: J. Anderson and M. Boudart (Eds.), Catalysis Science and Technology Vol. 1, Springer Verlag, Berlin, 1981, p. 182.

11. R. Anderson in: P.H. Emmett (Ed.), Catalysis Vol. IV, Reinhold, New York, 1956, p. 117.

12. R. Madon, E. Iglesia, J. Catal. 149 (1994) 428-437.

13. M. Dry, Catal. Today 71 (2002) 227-241.

14. T. Donnelly, I. Yates, C. Satterfield, Energy & Fuels 2 (1988) 734-739.

15. J. Patzlaff, Y. Liu, J. Gaube, App. Catal. A 186 (1999) 109-119.

Chapter Four

The Effect of Distributed Syngas Feeding on Fischer-Tropsch Product Distributions – Part 2

4.1 Introduction

The experiments of the preceding chapter demonstrate the ineffectiveness of a distributed syngas feeding approach in creating higher molecular weight products when complete CO conversion is effected within the first of two series reactors. This chapter compares the product distributions generated by distributed and normal feeding regimes for incomplete CO conversion in the first reactor. Two separate sets of experiments were designed and performed; the first utilized high catalyst loadings in the second series reactor while the second utilized low catalyst loadings in the second reactor.

The first experiments, hereafter referred to as HR2CL (for high Reactor 2 catalyst loading), represent a continuation of the previous chapter's work. High CO conversion in Reactor 1 of the distributed regime caused the H_2/CO ratio to increase quickly due to simultaneous hydrogen production by the water-gas shift reaction. This concentration profile resulted in the generation of a lighter product distribution relative to the normal regime. The HR2CL experiments explore the effect of lower CO conversion in Reactor 1 while attempting to keep Reactor 2 conversions high to maximize product yield.

The second set of experiments, abbreviated LR2CL (for low Reactor 2 catalyst loading), examines the effect of incremental CO conversion in each series reactor on FT product distributions. This configuration would act as an initial proof of concept for a

reactor system using several series reactors with incremental CO conversion occurring through each one. The subsequent analysis compares the results of the LR2CL experiments to simulations conducted with the reaction model described in Chapter Two.

4.2 Experimental

4.2.1 Catalyst Synthesis

A precipitated iron catalyst similar to the one described in Chapter Three was employed in the experiments (HR2CL and LR2CL) of the present chapter. The catalyst was promoted with copper and potassium in order to improve the validity of comparison with the FT reaction model of Chapter Two that was based on an Fe-Cu-K-SiO_2 catalyst [1].

A solution of 9.1 wt.% sodium carbonate monohydrate heated to 80°C was added to a solution of 13.7 wt.% iron (III) nitrate nonahydrate and 36.1 parts per million (ppm) by weight cupric nitrate trihydrate until the pH of the resulting suspension reached 8.0. This suspension was maintained at a temperature of 80°C while potassium carbonate 1.5-hydrate (0.25 grams per 250 mL suspension) and tetraethyl orthosilicate (0.5 mL per 250 mL suspension) were added. It was then allowed to cool to room temperature followed by filtration and rinsing with 2.0 mL deionized water per 1.0 mL suspension. The wet filtrate was dried at 110°C for twelve to fifteen hours. The final weight ratio of the species comprising the catalyst was approximately 100:5.0:2.8:4.9 Fe:Cu:K:SiO_2 as estimated by the proportion of starting materials.

The catalyst was calcined at 400°C for four hours followed by crushing and sieving to 60-200 mesh size (0.074 to 0.25 mm particle diameter). The crushed catalyst

was blended with at least two times its volume of 60-200 mesh size silica gel to achieve isothermality in the catalyst bed. Reduction took place under flowing hydrogen at 200 sccm and 55 psia (0.38 MPa) for 24 hours.

4.2.2 Reaction Conditions and Procedure

The experiments of the present chapter used an apparatus identical to the one of Figure 3.1 described in Chapter Three. Appendix B gives further detail regarding analytical methods. Reaction conditions for each set of experiments are described below.

4.2.2.1. HR2CL Experiments

Reactor 1 was loaded with 0.5 g precipitated iron catalyst blended with 1.5 g silica gel, while Reactor 2 was loaded with 3.0 g precipitated iron catalyst blended with 3.0 g silica gel. Temperature and pressure were maintained at 270°C and 140 psia (0.97 MPa) in both reactors. A constant amount of syngas was fed into the reactor system under each syngas feeding regime in addition to a small flow of nitrogen as an inert standard. The syngas was fed entirely into the entrance of the first reactor under the normal feeding regime, whereas it was divided equally and fed into the entrances of Reactors 1 and 2 in the distributed feeding regime.

Experiments were conducted using two different inlet syngas compositions for each syngas feeding regime: one deficient in hydrogen ($H_2/CO = 1.0$) and one rich in hydrogen ($H_2/CO = 2.0$). Analysis of both Reactor 1 and Reactor 2 effluent streams was performed. Table 4.1 summarizes the experimental flowrates and catalyst weight to flowrate (W/F) ratios. The values for W/F ratios take into account the total reactant

flowrates and catalyst weights; due to differences in feed location, the reactors of the distributed and normal feeding regimes have different resident times.

Table 4.1: Summary of flowrates into each reactor under the distributed and normal syngas feeding regimes of the HR2CL experiments.

Inlet H_2/CO Ratio	1.0		2.0	
Flowrates	Distributed	Normal	Distributed	Normal
Reactor 1 (sccm H_2/CO)	20/20	40/40	40/20	80/40
Reactor 2 (sccm H_2/CO)	20/20	–	40/20	–
W/F (g·h/mol)	16.6		11.0	

After catalyst pre-reduction, the catalyst was pre-conditioned for 24 hours under reaction conditions. Data was then gathered for another 24 hours with the final 12 hours of data averaged for the analysis presented in Section 4.3. The catalyst was replaced, pre-reduced, and pre-conditioned before implementing the next set of experimental conditions.

4.2.2.2 LR2CL Experiments

Reactors 1 and 2 were each loaded with 0.25 g of the previously described iron catalyst physically blended with 5.0 g silica gel. Temperature and pressure were maintained at 250°C and 140 psia (0.97 MPa) in both reactors.

As with the HR2CL experiments, analysis of Reactor 1 and Reactor 2 effluents was performed for the LR2CL experiments using syngas with H_2/CO ratios of 1.0 and 2.0. Table 4.2 summarizes the flowrates and W/F values of each syngas feeding regime and reactant composition case.

Table 4.2: Summary of flowrates into each reactor under the distributed and normal syngas feeding regimes of the LR2CL experiments.

Inlet H_2/CO Ratio	1.0		2.0	
Flowrates	Distributed	Normal	Distributed	Normal
Reactor 1 (sccm H_2/CO)	10/10	20/20	20/10	40/20
Reactor 2 (sccm H_2/CO)	10/10	–	20/10	–
Single Reactor W/F (g·h/mol)	4.73	2.36	3.15	1.58
Dual Reactor W/F (g·h/mol)	4.73		3.15	

The same catalyst batch was used for every experimental case in the LR2CL experiments. The catalyst was first pre-conditioned at a flowrate of 30 sccm H_2 and 20 sccm CO fed into the entrance of Reactor 1 for 24 hours, after which 24 hours of data were gathered under each combination of conditions. Flow conditions were changed on-line at the end of each 24-hour period. As with the HR2CL experiments, the results of Section 4.3 represent an average of the final 12 hours of data collection at each set of experimental conditions. These conditions were intermittently returned to a baseline set of conditions to ensure the catalyst was operating under steady state.

4.3 Results and Discussion

4.3.1 HR2CL Experiments

4.3.1.1 Carbon Monoxide Conversion

Figure 4.1 summarizes the observed CO conversions at the exit of each reactor. Total CO conversions were 50-60% for the 1.0 H_2/CO inlet syngas case and 65-75% for the 2.0 H_2/CO inlet syngas case. The higher conversion levels in the 2.0 H_2/CO inlet syngas case were expected given that FT reaction rate increases with increasing hydrogen partial pressure [2].

These conversion levels were less than desired, as the experiments were designed to effect incremental CO conversion through Reactor 1 and nearly complete total conversion through both reactors. Loss of catalyst surface area may explain the failure to achieve the desired conversion results. Upon unloading the catalyst from the reactors after the experiments, agglomeration of the catalyst powder into larger particles was observed. This agglomeration may have indicated that the catalyst was insufficiently diluted with silica gel to ensure isothermality during catalyst reduction, as the exothermicity associated with reduction can increase the kinetics of catalyst sintering. Precipitated iron catalysts can lose 25-50% of their initial surface area during reduction under flowing H_2 [3].

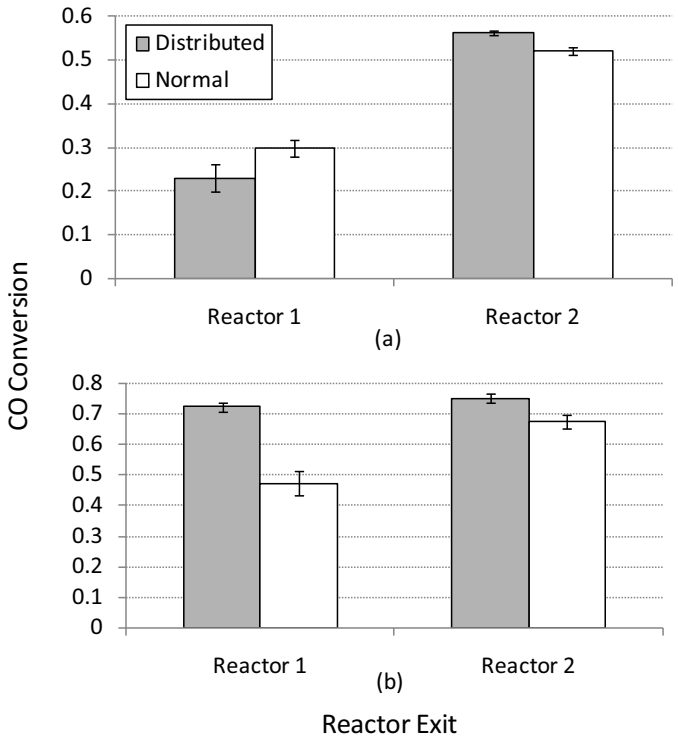

Figure 4.1: Experimental CO conversions as measured at the exits of Reactors 1 and 2 in the HR2CL experiments. (a) Inlet $H_2/CO = 1.0$. (b) Inlet $H_2/CO = 2.0$.

1.0 H_2/CO Case

The Reactor 1 CO conversions in the 1.0 H_2/CO case are somewhat counterintuitive, in that one would expect greater CO conversion in the distributed regime due to higher residence time. This effect may be explained by greater CO_2 selectivity in the distributed case, as is discussed in Section 4.3.1.2. The initial FT rate within Reactor 1 of the distributed regime may have led to a quick decrease in the H_2/CO ratio due to below stoichiometric proportions of hydrogen in the inlet syngas and low bulk flowrates compared to the normal regime. In turn this effect may have led to a sustained increase in the rate of the water-gas shift reaction in Reactor 1 and higher overall CO conversion, with a large portion of the reactant CO converted to the undesirable product CO_2. Total CO conversions were also slightly higher for the distributed regime despite lower reactant contact time with the catalyst.

2.0 H_2/CO Case

Conversion levels between 70-75% were observed at the exit of each reactor for the distributed regime, whereas approximately 45% CO conversion through Reactor 1 and almost 70% total CO conversion was achieved in the normal regime. The distributed regime resulted in higher total CO conversion levels, consistent with observations for the 1.0 H_2/CO case.

4.3.1.2 Carbon Dioxide Selectivity

Figure 4.2 summarizes the CO_2 carbon atom selectivity within each reactor and in total for each set of experimental conditions; these data represent the amount of CO converted to CO_2 via the water-gas shift reaction relative to FT. The 1.0 H_2/CO case exhibited higher CO_2 carbon atom selectivities than the 2.0 H_2/CO case, an expected

observation given that the syngas of the former composition was further from equilibrium and therefore would cause the water-gas shift reaction to occur at a higher rate.

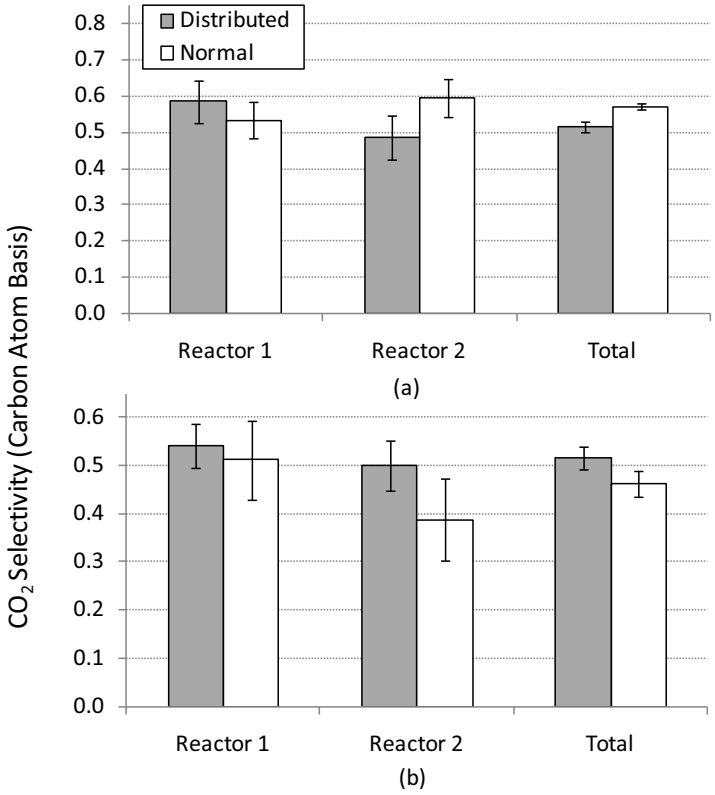

Figure 4.2: Experimental carbon atom selectivities of CO_2 in the HR2CL experiments. (a) Inlet $H_2/CO = 1.0$. (b) Inlet $H_2/CO = 2.0$.

1.0 H_2/CO Case

An increase in CO_2 carbon atom selectivity was observed for the normal regime between Reactors 1 and 2 (53.2% to 59.4%) whereas a significant decrease was observed for the distributed regime (58.3% to 48.3%). The difference between syngas feeding regimes within Reactor 2 seemed to control the overall difference in CO_2 carbon atom selectivities.

2.0 H_2/CO Case

The CO_2 carbon atom selectivity was lower in Reactor 2 than in Reactor 1 in each syngas feeding regime, although the values within individual reactors were not statistically different from one another for either syngas feeding regime. The decrease between reactors was more significant for the normal regime, translating to a higher total CO_2 carbon atom selectivity in the distributed regime. As with the 1.0 H_2/CO case, Reactor 2 appeared to control the difference in total CO_2 carbon atom selectivity observed between the two syngas feeding regimes.

4.3.1.3 Hydrocarbon Selectivity

Figure 4.3 depicts the molar selectivity of hydrocarbon products against carbon number for each experimental case. The distributions depicted in Figures 4.3(b) and 4.3(d) represent those calculated at the Reactor 2 exit and therefore represent the overall hydrocarbon selectivities of each system.

The following sections discuss the product distributions of the normal and distributed feeding regimes relative to each other for each inlet syngas composition case. Figure 4.4 summarizes the rates of CO conversion within each reactor and shows the proportion of CO converted to CO_2 and to hydrocarbons. This figure is used to explain the results presented in Figure 4.3.

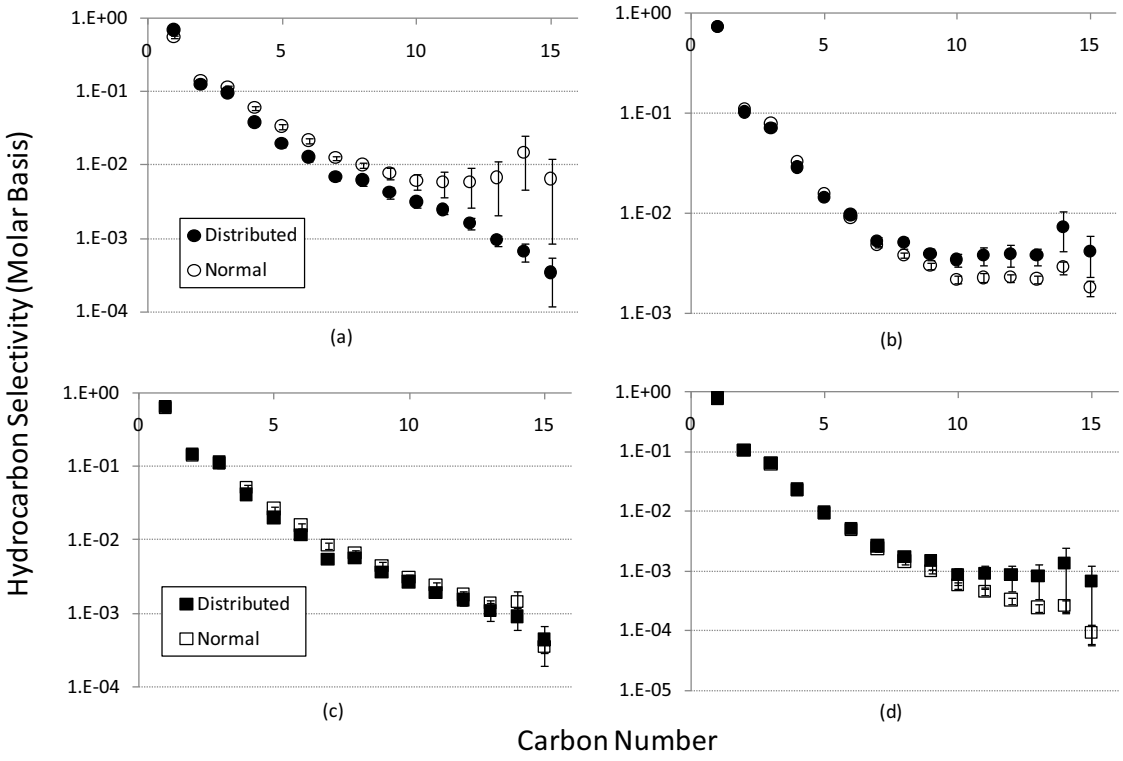

Figure 4.3: Experimental hydrocarbon selectivities in the HR2CL experiments.
(a) Reactor 1 effluent, inlet $H_2/CO = 1.0$. (b) Reactor 2 effluent, inlet $H_2/CO = 1.0$.
(c) Reactor 1 effluent, inlet $H_2/CO = 2.0$. (d) Reactor 2 effluent, inlet $H_2/CO = 2.0$.

1.0 H_2/CO Case

The normal regime generated a heavier product distribution than the distributed regime at the exit of Reactor 1; this trend reverses itself by the Reactor 2 exit at which the distributed regime exhibits higher selectivity toward hydrocarbons in the $C_9 - C_{15}$ range. This result suggests the existence of a "crossover point" in Reactor 2 at which the selectivity toward higher molecular weight products of the distributed regime surpasses that of the normal regime.

The interaction of FT with the water-gas shift reaction provides a possible explanation for the observed product distributions. Figure 4.4(a) shows that the distributed regime generated more total products on a carbon atom basis than did the

normal regime, but each regime produced CO_2 at approximately equal rates. The production of CO_2 via the water-gas shift reaction results in the equimolar production of hydrogen that then may be used by FT. Therefore, the ratio of extra hydrogen production to hydrocarbon product generation was higher in the normal regime, resulting in a lighter total distribution among hydrocarbon products relative to the distributed regime.

The chemistry in Reactor 2 appears to control the final product distributions. CO_2 accounts for nearly 60% of the carbon containing products generated in the normal regime and only 48% in the distributed regime within Reactor 2. FT in the normal regime occurred under conditions of greater hydrogen production, and the resulting products were lighter in average molecular weight as compared to those of the distributed regime.

2.0 H_2/CO Case

The hydrocarbon product distributions of the distributed and normal regimes exiting Reactor 1 were very close in average molecular weight, and as with the 1.0 H_2/CO case, a heavier overall distribution was observed for the distributed regime as measured at the Reactor 2 exit. The hydrocarbon selectivity data of the distributed regime showed wide experimental variability, calling into question whether the hydrocarbon selectivity of the two syngas feeding regimes in the C_9-C_{15} range were statistically different from one another.

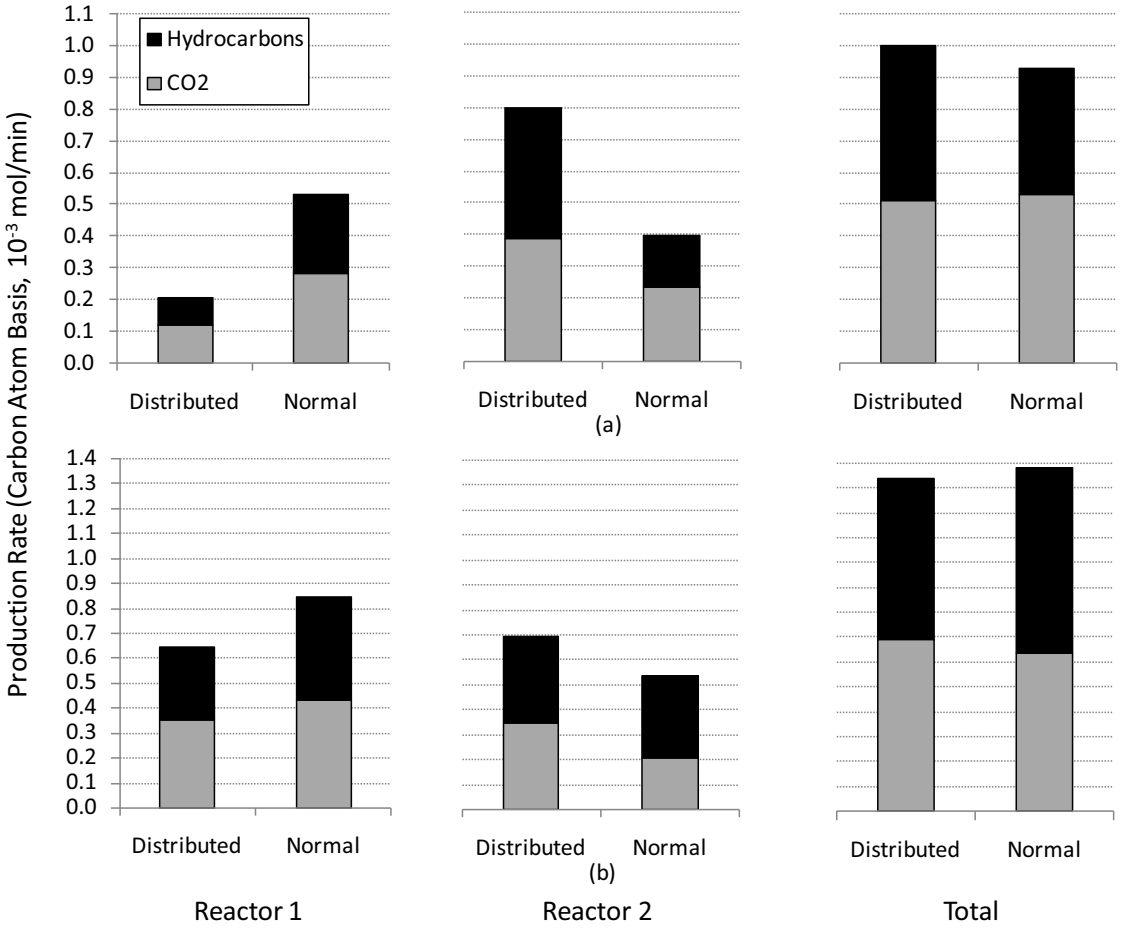

Figure 4.4: Experimental production rates of hydrocarbons and CO_2 on a carbon atom basis for the HR2CL experiments within Reactor 1, within Reactor 2, and in total. (a) Inlet $H_2/CO = 1.0$. (b) Inlet $H_2/CO = 2.0$.

4.3.2 LR2CL Experiments

The LR2CL experiments were run under conditions identical to those assumed by the reaction model developed in Chapter Two. The subsequent sections present the results of these experiments with regards to CO conversion, CO_2 selectivity, and hydrocarbon selectivity. The CNDERM reaction model developed in Chapter Two was used to simulate these experiments through plug flow reactors, and the relevant calculations are compared with experimental observations.

The reader will recall that an analytical expression for empty surface sites or methylene monomers could not be derived in the CNDERM. Therefore, the catalyst bed of each reactor was simulated as 100 continuously stirred tank reactors (CSTRs) with the effluent of the previous reactor used as the influent of the next. In the simulations of the distributed regime, fresh reactants were added to the initial conditions between the 100th and 101st model CSTRs. Although development of the reaction model relied upon experimental data from a CSTR, application of the model to plug flow reactor experiments is valid given experimental efforts to maintain catalyst bed isothermality in a kinetically limited regime.

4.3.2.1 Carbon Monoxide Conversion

Figure 4.5 shows the experimental CO conversion values at the exits of Reactor 1 and 2, and Figure 4.6 depicts CO conversion along the reactor axes as calculated by the reaction model. Conversion through Reactor 1 of the distributed regime takes into account only the CO fed at the entrance of this reactor. Reactor 2 exit conversion levels take into account all CO fed to the reactor system.

CO conversion in the 2.0 H_2/CO case is higher than in the 1.0 case, both experimentally and computationally. The experimental finding was similar to that of the HR2CL experiments and was expected due to higher FT rates associated with increased H_2 partial pressure.

1.0 H_2/CO Case

CO conversion in the distributed regime through Reactor 1 was approximately the same as total conversion (35%), an observation that was matched by the reactor model prediction. Less than half of the total CO conversion in the normal regime (40%)

occurred in Reactor 1 (15%). Total CO conversion as predicted by the model correlated well with the experimentally observed values. Experimental and computational results diverged for Reactor 1 conversion in the normal regime, with the model predicting slightly more than half of the total conversion occurring in Reactor 1.

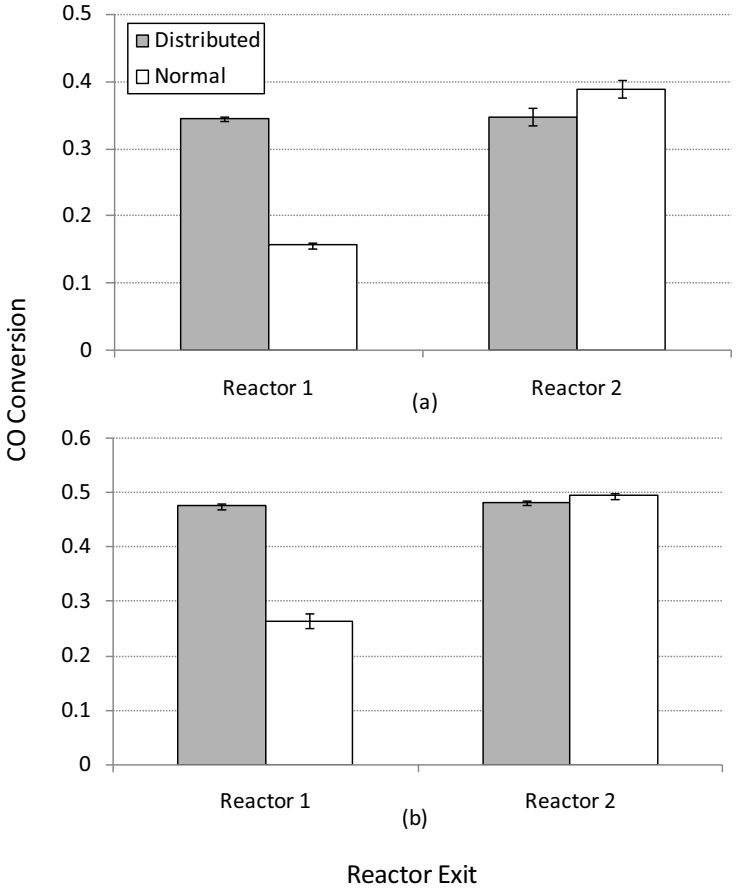

Figure 4.5: Experimental CO conversions as measured at the exits of Reactors 1 and 2 in the LR2CL experiments. (a) Inlet $H_2/CO = 1.0$. (b) Inlet $H_2/CO = 2.0$.

2.0 H_2/CO case

Total experimental conversions were approximately 50% in both syngas feeding regimes with similar computational results. The distributed regime showed similar experimental and computational conversion at the exits of Reactor 1 and 2. Again, the main point of divergence between model and experiment was the relative amount of CO

converted within each reactor in the normal regime, with half of the total CO conversion occurring within the first reactor experimentally and slightly more than half occurring within the first reactor according to the model.

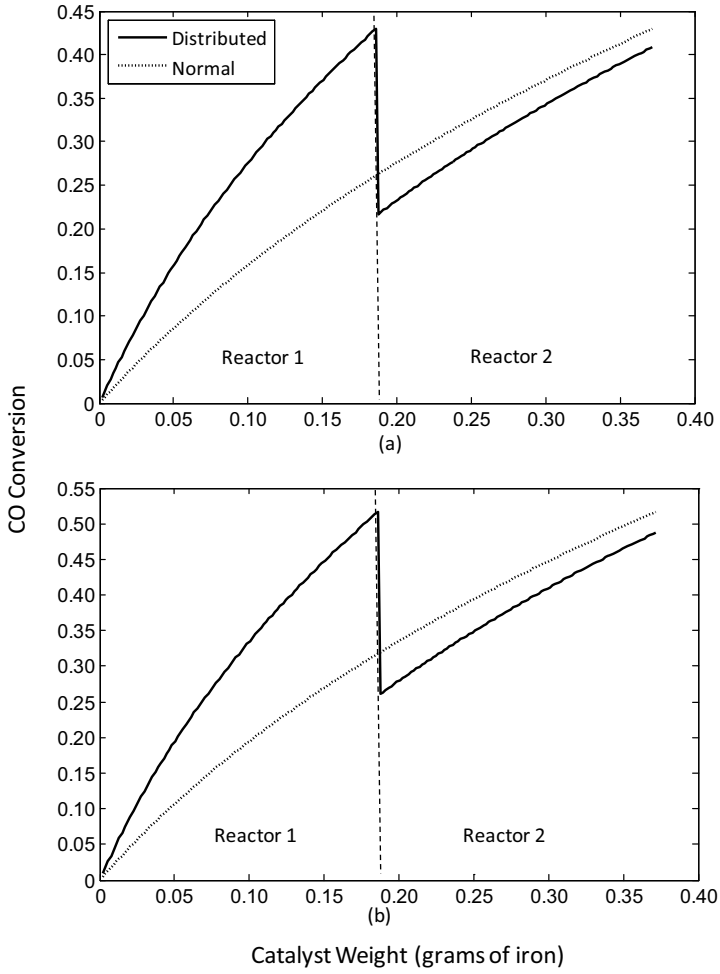

Figure 4.6: CO conversions along the reaction axis as computed by the FT reaction model for the conditions of the LR2CL experiments. (a) Inlet $H_2/CO = 1.0$. (b) Inlet $H_2/CO = 2.0$.

4.3.2.2 Carbon Dioxide Selectivity

Experimental CO_2 selectivities within each reactor and in total are shown in Figure 4.7. The 1.0 and 2.0 H_2/CO cases showed similar levels of CO_2 selectivity, an observation that may be explained by the cancellation of competing effects. The

composition of syngas in the 1.0 H_2/CO case lies to the left of water-gas shift equilibrium, meaning that the water-gas shift rate toward CO_2 and H_2 would be accelerated. However, FT and associated water production would have occurred more quickly in the 2.0 H_2/CO case due to the aforementioned effect of increased hydrogen partial pressure on FT reaction rate. The heightened rate of water production would have increased the rate of the water-gas shift reaction.

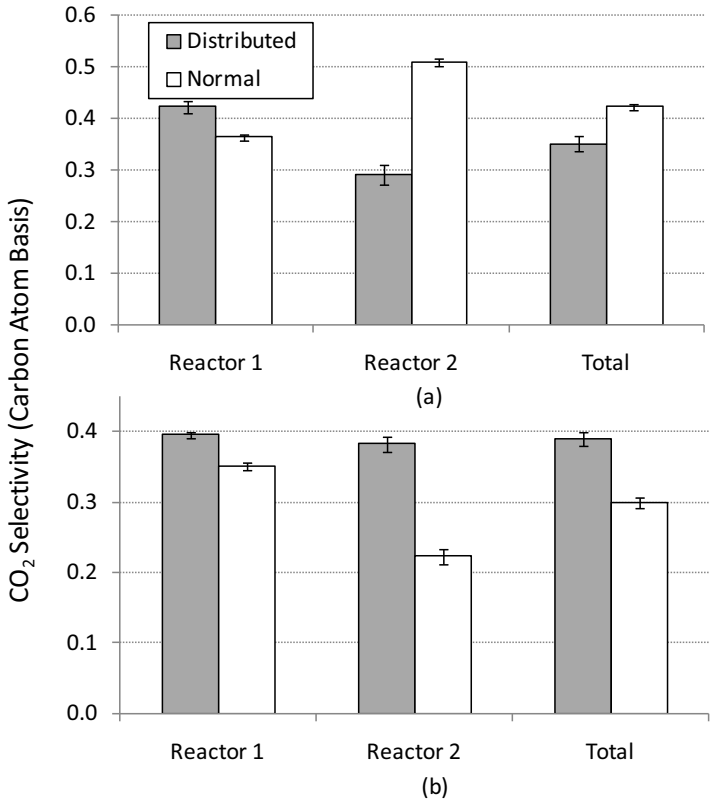

Figure 4.7: Experimental carbon atom selectivities of CO_2 in the LR2CL experiments. (a) Inlet H_2/CO = 1.0. (b) Inlet H_2/CO = 2.0.

Figure 4.8 depicts the computational CO_2 carbon atom selectivities along the reaction axis. Disagreement exists with the experimental observations in that the model calculates the CO_2 selectivities to be appreciably higher in the 1.0 H_2/CO case. The model also predicts that CO_2 selectivity increases monotonically along the reaction axis

regardless of inlet syngas composition or syngas feeding regime, a phenomenon that was not observed experimentally.

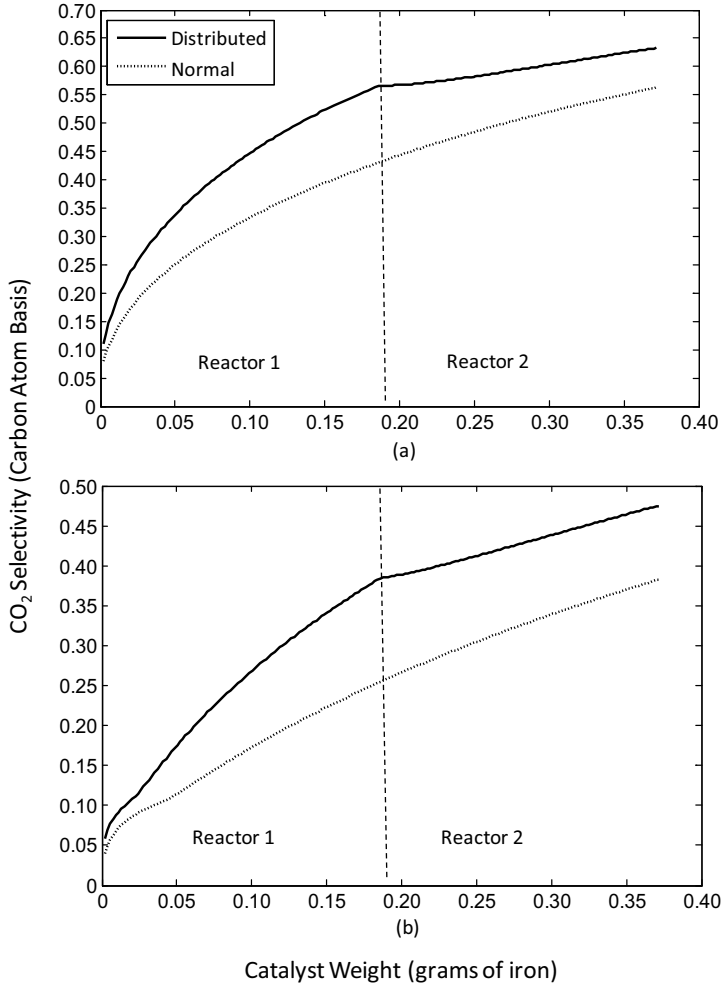

Figure 4.8: CO_2 carbon atom selectivity along the reaction axis as computed by the FT reaction model for the conditions of the LR2CL experiments. (a) Inlet $H_2/CO = 1.0$. (b) Inlet $H_2/CO = 2.0$.

1.0 H_2/CO case

Experimental CO_2 carbon atom selectivity was greater in the normal regime than in the distributed regime, driven primarily by Reactor 2. The normal regime exhibited greater CO_2 selectivity in Reactor 2 (over 50%) compared to Reactor 1 (36%), whereas the opposite was true for the distributed regime (42% in Reactor 1, 29% in Reactor 2).

The distributed feeding regime appears to have suppressed water-gas shift activity within Reactor 2 as compared to the normal regime, a phenomenon that also was observed for the 1.0 H_2/CO case of the HR2CL experiments. This apparent suppression resulted in lower overall CO_2 selectivity in the distributed regime for the 1.0 H_2/CO case of the LR2CL experiments.

The reaction model calculates total CO_2 carbon atom selectivities between 55 and 65% in contrast with the experimentally observed values of 35 to 45%. The simulations also show an increase in CO_2 carbon atom selectivity between the exits of Reactors 1 and 2 for both syngas feeding regimes, whereas only the normal regime exhibited such an increase experimentally. However, the reaction model clearly predicts that the rate of increase slows in the distributed regime upon addition of fresh syngas at the Reactor 2 entrance, indicating a suppression of water-gas shift activity that was also observed experimentally.

2.0 H_2/CO case

Experimental CO_2 carbon atom selectivity in the distributed regime was higher than that in the normal regime within Reactor 1 (40% for distributed, 35% for normal), within Reactor 2 (38% vs. 22%), and in total (39% vs. 30%). The CO_2 carbon atom selectivity in Reactor 2 was lower than in Reactor 1 of the normal regime, while the CO_2 carbon atom selectivities within Reactors 1 and 2 of the distributed regime remained relatively constant. The suppression of water-gas shift activity that appeared to occur at the entrance of Reactor 2 of the distributed regime in the 1.0 H_2/CO case did not occur in the 2.0 H_2/CO case.

As with the 1.0 H_2/CO case, the reaction model predicts an increase for both syngas feeding regimes along the entire reaction axis, and the CO_2 carbon atom selectivity throughout Reactor 2 of the distributed regime is clearly affected by the secondary syngas feed. However, the gap between CO_2 carbon atom selectivities of the normal and distributed regimes remains constant throughout Reactor 2 in the 2.0 H_2/CO case, where this gap decreased in the 1.0 H_2/CO case as calculated by the reaction model.

4.3.2.3 Hydrocarbon Selectivity

Figure 4.9 summarizes the experimental product distributions of each syngas feeding regime and reactant composition case, and Figure 4.10 summarizes production rates of carbon containing products. The following sections discuss the effect of the relationship between the water-gas shift reaction and FT on the experimentally observed product distributions.

1.0 H_2/CO case

At the Reactor 1 exit, the distributed regime generated a distribution more selective to methane and very slightly less selective to C_{5+} hydrocarbons as compared to the normal regime (CH_4 selectivity: 32.2%±0.4% for distributed, 30.4%±0.3% for normal; CH_{5+} selectivity: 30.5%±0.3% for distributed, 30.8%±0.5% for normal). However, the distributed regime produced a heavier total distribution as determined by the hydrocarbon selectivities at the Reactor 2 exit (CH_4 selectivity: 31.0%±0.9% for distributed, 33.7%±0.5% for normal; C_{5+} selectivity: 34.8%±2.1% distributed, 27.8%±0.5% normal). The same crossover point observed in the HR2CL experiments described in Section 4.3.1.3 was seen in the LR2CL experiments as well, whereby the

distributed regime surpassed the normal in average product weight at some point in Reactor 2.

Figure 4.10 shows that a larger proportion of CO converted within Reactor 2 of the normal regime was converted to CO_2 as compared to the distributed regime. Therefore, FT in Reactor 2 of the distributed regime took place under conditions of less hydrogen production from the water-gas shift reaction, resulting in a final product distribution that was heavier than that generated under the normal regime.

Figure 4.11 depicts the selectivity of C_{5+} hydrocarbons along the reaction axis as calculated by the reaction model. The most noteworthy aspect of this figure is the sudden increase in C_{5+} selectivity that occurs at the entrance of Reactor 2 and corresponds with the suppression of the increase in CO_2 selectivity seen in Figure 4.8. If Reactor 2 indeed controlled the overall product distributions, this sudden may explain the "crossover point" that was postulated experimentally.

2.0 H_2/CO case

The product distribution of the normal regime in the 2.0 H_2/CO case was slightly heavier than that of the distributed regime exiting Reactor 1 (CH_4 selectivity: 39.8%±0.4% for distributed, 37.2%±0.4% for normal; C_{5+} selectivity: 24.0%±0.4% for distributed, 26.3%±0.4% for normal) and became more so through Reactor 2 (CH_4 selectivity: 40.6%±0.6% for distributed, 35.6%±0.8% for normal; C_{5+} selectivity: 22.0%±1.0% for distributed, 31.1%±1.8% for normal). This observation indicates that a distributed feeding strategy is counterproductive in producing higher molecular weight hydrocarbons using hydrogen rich syngas at incremental CO conversions. Reactor 2 again appeared to weight the final product distributions more heavily than Reactor 1.

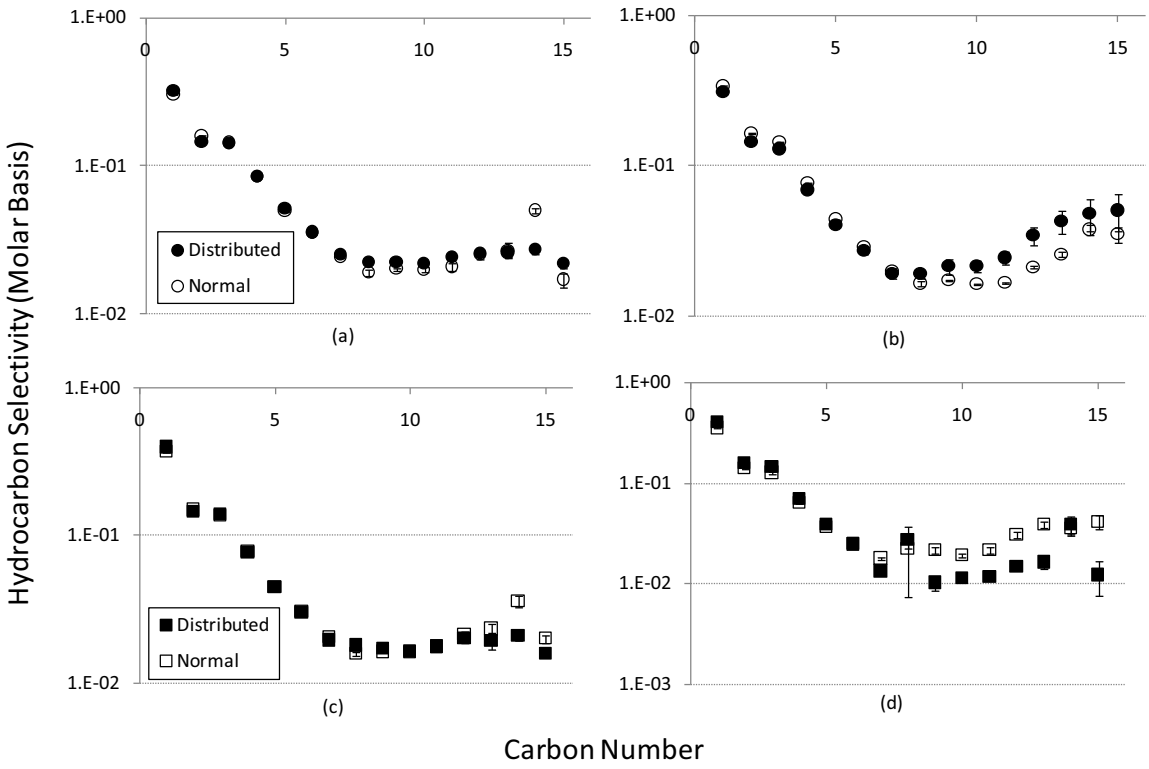

Figure 4.9: Experimental hydrocarbon selectivities in the LR2CL experiments.
(a) Reactor 1 effluent, inlet $H_2/CO = 1.0$. (b) Reactor 2 effluent, inlet $H_2/CO = 1.0$.
(c) Reactor 1 effluent, inlet $H_2/CO = 2.0$. (d) Reactor 2 effluent, inlet $H_2/CO = 2.0$.

A higher proportion of the CO converted within Reactor 2 went to CO_2 under the distributed regime, resulting in greater hydrogen production from the water-gas shift reaction. This hydrogen acted to increase the H_2/CO ratio in the distributed syngas feeding regime and explains the observed final product distributions where the normal regime produced hydrocarbons with a higher average molecular weight.

The reaction model calculated the same effect on CO_2 and C_{5+} selectivity in the 2.0 H_2/CO case that was calculated for the 1.0 H_2/CO case. Therefore, experimental and computational results disagree for the 2.0 H_2/CO case, as the distributed syngas feeding strategy experimentally resulted in a higher degree of water-gas shift activity relative to FT in Reactor 2 and a lighter overall product distribution. The origin of the disagreement

does not appear to be in the H_2/CO profile exiting the first reactor and entering the second; the H_2/CO ratios entering Reactor 2 in both the normal and distributed regimes were between 2.1 and 2.3 as calculated by the model and observed experimentally. However, the ratio of CO_2 to H_2+CO entering Reactor 2 differed between model and experiment. Table 4.3 summarizes the amount of CO_2 relative to H_2 and CO entering Reactor 2 for both model and experiment, where the model computes lower amounts of CO_2 entering Reactor 2 than were experimentally observed. The extent of the water-gas shift reaction through Reactor 1 was higher experimentally, leading to lower overall water-gas shift activity in Reactor 2 and less opportunity for suppression of this activity in the distributed regime. Due to the relatively low water-gas shift activity computed by the model through Reactor 1, the potential to suppress the water-gas shift reaction in Reactor 2 of the distributed regime is greater relative to experiment. This leads to the computational trend in C_{5+} hydrocarbon selectivity observed at the interface of Reactors 1 and 2 in Figure 4.11b. The disagreement between model and experiment in this case may indicate that the rate expression derived for the water-gas shift reaction over iron FT catalysts is inaccurate in its response to CO_2 partial pressure under these experimental conditions.

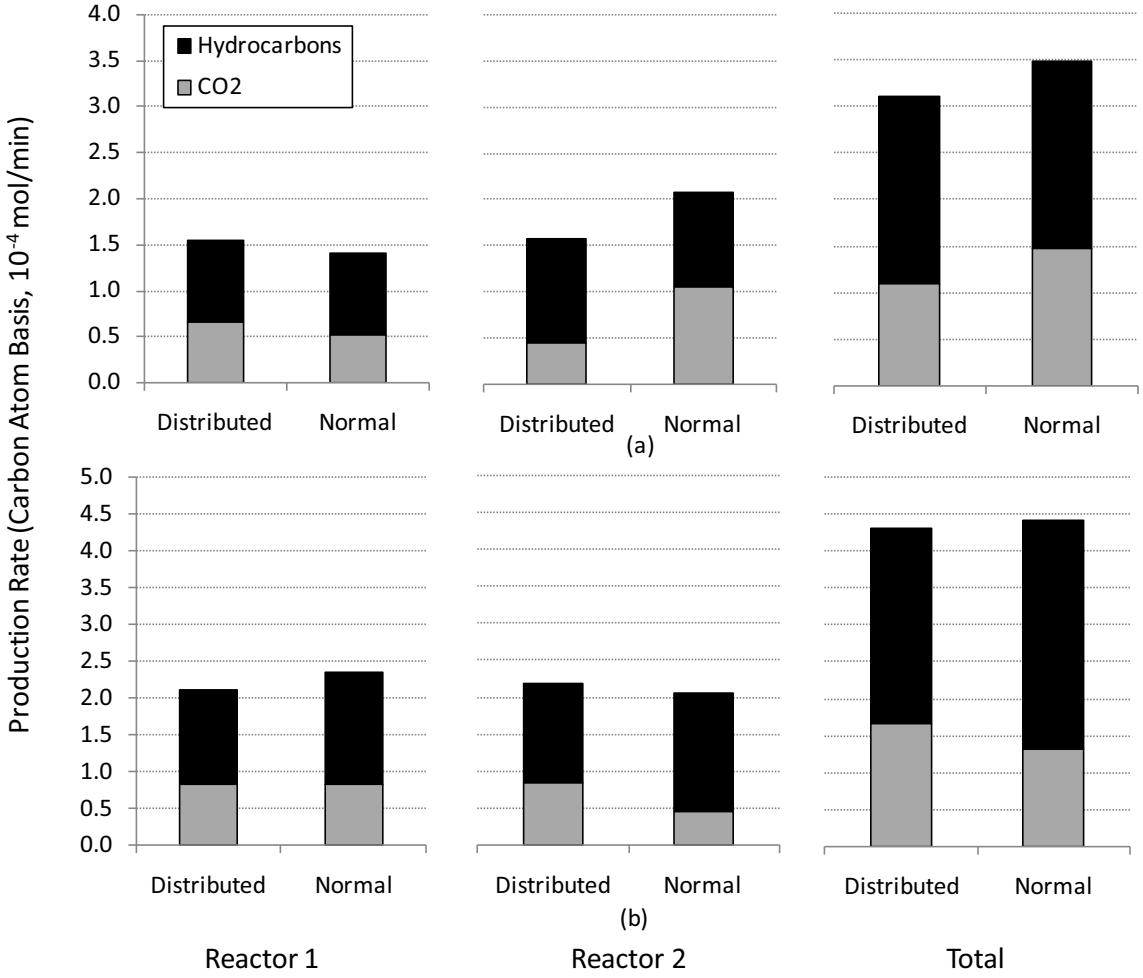

Figure 4.10: Experimental production rates of hydrocarbons and CO_2 on a carbon atom basis for the LR2CL experiments within Reactor 1, within Reactor 2, and in total. (a) Inlet $H_2/CO = 1.0$. (b) Inlet $H_2/CO = 2.0$.

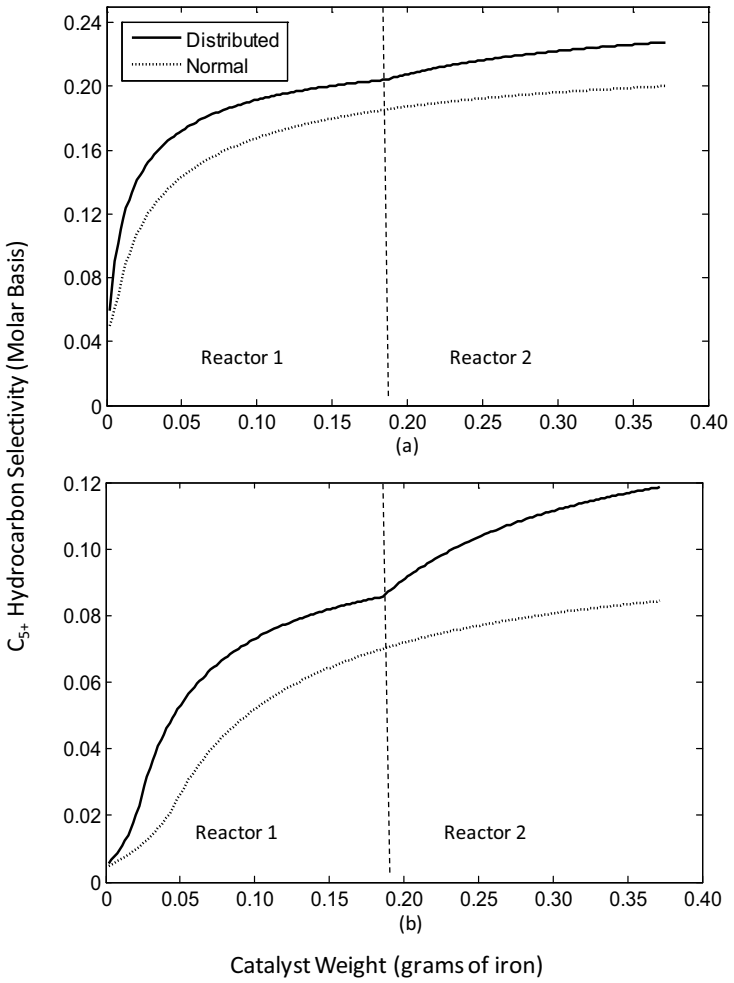

Figure 4.11: C_{5+} hydrocarbon selectivity along the reaction axis as computed by the FT reaction model for the conditions of the LR2CL experiments. (a) Inlet $H_2/CO = 1.0$. (b) Inlet $H_2/CO = 2.0$.

Table 4.3: Ratios of $CO_2/(CO+H_2)$ entering Reactor 2 in the LR2CL experiments.

	Distributed Regime	Normal Regime
Experimental	0.089	0.049
Computational	0.022	0.024

4.3.2.4 Relationship between Carbon Monoxide Conversion and Hydrocarbon Selectivity

Figure 4.12 depicts a scatterplot of methane and C_{5+} hydrocarbon selectivity, both on a molar basis, versus CO conversion. Although previous FT studies have found linear

or curvilinear relationships between hydrocarbon selectivity and CO conversion, such studies have examined normal syngas feeding regimes. The results displayed in Figure 4.12 demonstrate that the hydrocarbon selectivity results reported in the current study did not simply rely on the amount of CO conversion that was effected. Approximately the same CO conversions were achieved at the exit of Reactor 1 of the distributed regime, at the exit of Reactor 2 of the distributed regime, and at the exit of Reactor 2 of the normal regime for both 1.0 and 2.0 H_2/CO cases. However, statistically distinct hydrocarbon selectivities were achieved between the distributed and normal syngas feeding regimes. This observation demonstrates that any advantage imparted by a distributed syngas feeding regime in improving the selectivity of heavier hydrocarbons cannot be replicated simply by adjusting the extent of CO conversion in the corresponding normal regime.

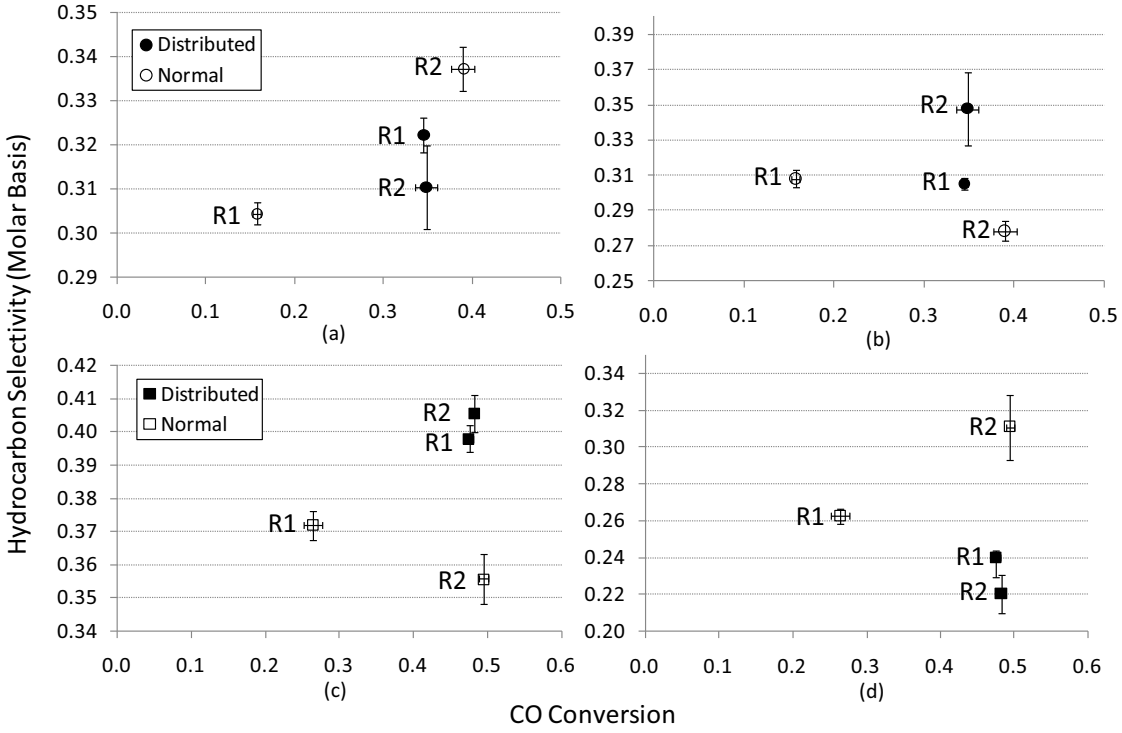

Figure 4.12: Depiction of hydrocarbon selectivity versus CO conversion for the LR2CL experiments. The symbols R1 and R2 denote the conditions exiting Reactor 1 and Reactor 2, respectively. (a) Methane selectivity, inlet $H_2/CO = 1.0$. (b) C_{5+} hydrocarbon selectivity, inlet $H_2/CO = 1.0$. (c) Methane selectivity, inlet $H_2/CO = 2.0$. (d) C_{5+} hydrocarbon selectivity, inlet $H_2/CO = 2.0$.

4.4 Conclusions

The study of the current chapter endeavored to determine whether a distributed syngas feeding strategy in FT would produce heavier molecular weight hydrocarbons than normal syngas feeding. A two-stage series reactor system was used in which CO conversion in the first reactor was incremental and CO conversion in the second was varied.

In both the HR2CL and LR2CL experiments, the distributed feeding regime generated a heavier product distribution than the normal regime for an inlet syngas with inlet $H_2/CO = 1.0$, showing an improvement in C_{5+} hydrocarbon selectivity of 25-30%. The relative activity of the water-gas shift reaction to FT within Reactor 2 appeared to

most heavily influence the final product distributions. Suppressed water-gas shift activity in Reactor 2 of the distributed regime, and the consequent suppressed production of hydrogen from the water-gas shift reaction, caused a heavier product distribution to be formed in the distributed regime. Simulations of the LR2CL experiments for the 1.0 H_2/CO case support the explanation of suppressed water-gas shift activity and increased C_{5+} selectivity throughout Reactor 2. This result represents a significant finding in that the weight of an FT product distribution was increased simply by altering the location of the inlet syngas.

In the 2.0 H_2/CO case, the distributed feeding regime resulted in a heavier product distribution for the HR2CL experiments and a lighter product distribution for the LR2CL experiments. The water-gas shift activity relative to FT in Reactor 2 of the distributed regime was unchanged by the fresh syngas feed in both sets of experiments. This finding, taking into consideration the large experimental variability of the data in the 2.0 H_2/CO case of the HR2CL experiments, casts some doubt as to whether a distributed feeding strategy can produce higher molecular weight products for hydrogen rich syngas.

The concept of hydrogen residence time was also put forth by Sharifnia et al. [4] to explain product selectivity results using distributed hydrogen feeding. In general they found that withholding hydrogen from a plug-flow reactor resulted in the production of higher molecular weight hydrocarbons. The increase in C_{5+} selectivity came at the expense of overall CO conversion, an industrially undesirable tradeoff. The distributed regime of the present study also resulted in lower overall CO conversions; this decrease in conversion was more than offset by the increase in selectivity such that the yield of C_{5+}

hydrocarbons from the distributed regime was greater than that observed in the normal regime.

References

1. G. van der Laan, A. Beenackers, Ind. Eng. Chem. Res. 38 (1999) 1277-1290.

2. G. Huff, C. Satterfield, Ind. Eng. Chem. Process Des. Dev. 23 (1984) 696-705.

3. M. Dry in: J. Anderson and M. Boudart (Eds.), Catalysis Science and Technology Vol. 1, Springer Verlag, Berlin, 1981, p. 177.

4. S. Sharifnia et al., Fuel Proc. Technol. 86 (2005**)** 1253-1264.

Chapter Five

The Effect of Co-Fed Azomethane on Fischer-Tropsch Product Distributions

5.1 Introduction

Methane is often considered the least desirable FT product because its sale requires the geographic proximity of natural gas pipelines which may not be convenient to the location of the FT plant. Its production therefore represents a decrease in the efficiency of syngas use, the manufacture of which comprises 60-70% of a typical FT plant's capital and operating costs [1]. The reduction of methane selectivity presents an ongoing challenge to industrial FT operation.

Activation of primarily formed methane provides a possible avenue to reducing methane yield. This task is not a trivial one given the chemical stability of methane relative to other hydrocarbon species. Such routes investigated in the scientific literature have included oxidative coupling of methane (OCM) [2-4] and chlorine catalyzed methane polymerization [5]. These processes take place at very different conditions of temperature and pressure as FT; consequently, any combination of methane activation with FT would require separation of methane from the FT effluent, activation of methane within a separate reactor, and recycle of the activated species to the FT reaction unit.

Methyl and methylene radicals ($\cdot CH_3$ and $\cdot CH_2$ respectively) are the likeliest species that would result from methane activation and could subsequently partake in FT

chemistry. The effect of these species on FT has been studied in order to elucidate the mechanism by which the reaction takes place. The most notable among these studies is the work of Brady and Petit who reacted diazomethane (CH_2=N=N) over cobalt, iron, ruthenium, palladium, and nickel catalysts in both the presence and absence of hydrogen gas [6]. Their findings advanced the theory of a stepwise methylene addition mechanism for the growth of hydrocarbon chains during FT via dissociation of diazomethane into $\cdot CH_2$ surface species. The study of van Barneveld and Ponec examined the nature of the FT reaction mechanism using chlorinated methyl compounds such as methyl and methylene chloride [7]. They reached similar conclusions as Brady and Petit regarding the FT polymerization mechanism.

The introduction of methyl radicals into an FT reactor via azomethane (CH_3-N=N-CH_3) has not been investigated thoroughly. Azomethane thermally decomposes into methyl radicals and dinitrogen at temperatures similar to those at which FT occurs [8]. Its dissociation properties render it a better candidate than chloromethane for studying the effect of added methyl radicals on FT product distributions, as the C-Cl bond in chloromethane homolytically cleaves only at temperatures above 1000K.

Surface $\cdot CH_3$ species act as chain initiators in FT, and as such, the addition of extra methyl radicals via azomethane may decrease the average hydrocarbon chain length of FT products assuming that the added radicals are then adsorbed onto the catalyst surface. However, Wojciechowski has maintained that methyl surface species may also act as chain terminators [9]. If this termination route occurs in parallel to hydrogen termination, a portion of the desorbed products would increase in chain length as a result of the termination step. Additional methyl radicals would also increase the paraffin

content of hydrocarbon products, as the rate of methyl termination would increase relative to that of olefin termination.

The current study examines the effect of azomethane co-feeding on FT product distributions. Its objective is twofold: 1. quantifying and understanding the aforementioned effect, and 2. providing a preliminary proof of concept for a study in which a recycled stream of activated methane, composed primarily of methyl radicals, would be co-fed with syngas into a conventional FT reactor to improve C_{5+} hydrocarbon selectivity. The subsequent sections describe the experimental procedure and results of azomethane co-feeding experiments. Diffuse Reflectance Infrared Fourier Transform Spectroscopy (DRIFTS) was employed in an effort to further investigate the fate of azomethane upon introduction to catalytic surfaces.

5.2. Experimental

The experimental procedure consisted of catalyst synthesis, azomethane synthesis, FT experiments, and DRIFTS studies. The steps of this procedure are subsequently detailed.

5.2.1 Catalyst Synthesis

A precipitated iron catalyst, supported by silica and promoted by copper and potassium, was synthesized in advance of the FT experiments. The catalyst composition and synthesis procedure were described in detail in Section 4.2.1. The catalyst was crushed and sieved according to this procedure as well.

5.2.2 Azomethane Synthesis

A modified version of the procedure followed by Renaud and Leitch [10] was followed to synthesize azomethane. A 14.2 wt.% solution of 1,2-dimethylhydrazine dihydrochloride in deionized water was prepared and brought to a pH of 7.0 with a solution of 7.2 wt.% sodium hydroxide in deionized water. The dimethylhydrazine solution was added very slowly to a suspension of yellow mercuric oxide in deionized water (0.56 g HgO per mL deionized water) with immediate precipitation of metallic mercury. The resulting supernatant azomethane solution (approximately 3 wt.%) was removed by pipette.

5.2.3 Fischer-Tropsch Reaction Procedure

A 316 stainless steel reactor with 3/4" outer diameter and 0.065" wall thickness was used to construct the packed bed reactor of the current study. The reactor was equipped with a 1/8" outer diameter stainless steel feed-through tube designed to exit directly into the catalyst bed and a 1/8" stainless steel thermocouple to measure the catalyst bed temperature. A diagram of the reactor is shown in Figure 5.1.

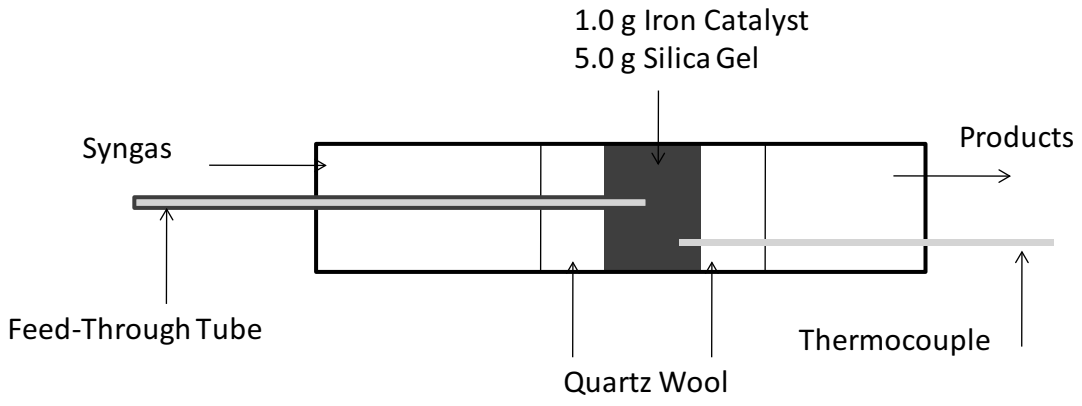

Figure 5.1: Depiction of reactor used for azomethane co-feeding experiments.

Approximately 1.0 grams of precipitated iron catalyst physically blended with 5.0 grams silica gel (60-200 mesh size) were loaded into the reactor; the catalyst bed was secured between two plugs of fine quartz wool. The catalyst was then reduced under 200 sccm hydrogen at 300°C and 55 psia (0.38 MPa).

Syngas of two H_2/CO ratios, 1.0 and 2.0, was introduced into the FT reactor, and fresh catalyst was used between the experiments of each syngas composition. The catalyst was pre-conditioned under the reaction conditions summarized in Table 5.1 until steady state syngas conversion and product concentrations were observed, about 36 hours. Nitrogen was used as an inert standard.

Table 5.1: Flowrates for catalyst pre-conditioning and experiments.

Inlet H_2/CO ratio	1.0	2.0
H_2/CO/N_2 flowrate (sccm)	20/20/10	40/20/10
W/F ratio (g mol/hr)	7.47	5.34

After pre-conditioning, nitrogen was directed through a saturator containing deionized water to establish baseline product distributions. The temperature of the liquid in the saturator was kept at 75-80°C and recorded using an internal thermocouple. The exit of the saturator was connected to the feed-through tube of the reactor so that the saturator effluent would be introduced directly into the catalyst bed.

The reaction was run for 24 hours while co-feeding water, after which the reaction was run again for another 24 hours in the absence of water. The saturator was then filled with the previously described aqueous azomethane solution, and the nitrogen standard was directed through the saturator. Its contents were kept at 75-80°C as with the water co-feed. The reaction was run thusly for another 24 hours.

Temperature and pressure were maintained at 270°C and 140 psia (0.97 MPa) throughout the experiments. Analysis of the reactor effluent was performed using a gas chromatograph equipped with one thermal conductivity detector (TCD) for the analysis of CO, CO_2, and N_2; one TCD for the analysis of H_2; and one flame ionization detector (FID) for the analysis of hydrocarbons from C_1 to C_{15}. All lines carrying product were heated to 200°C to prevent condensation of heavier hydrocarbons. Appendix B contains further information of the analytical setup.

5.2.4 DRIFTS Investigation

The interaction of azomethane on silica and reduced iron catalyst surfaces was investigated using DRIFTS. Silica gel (60-200 mesh size) and reduced iron catalyst were each wet impregnated with the aqueous azomethane solution described in Section 5.2.2. The samples were individually introduced to the DRIFTS chamber in a windowed sample cell, after which absorbance measurements were taken at 15°C under flowing nitrogen. Each sample was heated to and maintained at 80°C under flowing nitrogen until no condensation was observed on the sample cell windows, indicating complete evaporation of water from the sample. Absorbance measurements were taken of each sample at 100, 200, 300, and 400°C. The samples were maintained at each temperature for approximately one to two hours so that multiple measurements could be made and transient effects could be observed.

5.3 Results and Discussion

5.3.1 Azomethane Co-Feeding Experiments

Since azomethane was co-fed as an aqueous solution, the following sections compare the results of the FT experiments in which water was co-fed with syngas into the FT reactor with those in which aqueous azomethane was co-fed. Water is known to influence both the rate of FT and the water-gas shift reaction [11], and as such, comparing the results of the azomethane co-feeding experiments with those in which syngas was the only reactant would fail to account for the effect of water on FT.

5.3.1.1 1.0 H_2/CO Case

Table 5.2 summarizes CO conversion, CO_2 selectivity, and alpha values for the 1.0 H_2/CO inlet syngas case of the experiments described in Section 5.2.3. Two alpha values are reported; the first represents the chain growth probability of C_1-C_7 hydrocarbons, whereas the second represents the chain growth probability of C_8-C_{13} hydrocarbons.

Table 5.2: CO conversion, CO_2 carbon atom selectivity, and alpha values for water and azomethane co-feeding experiments with inlet H_2/CO = 1.0. Parenthetic values next to CO conversion and CO_2 selectivity data represent standard deviations. Parenthetic values next to alpha values represent 95% confidence intervals.

Co-Feed	Water	Azomethane
CO Conversion (%)	94.2 (±0.2)	94.5 (±0.2)
CO_2 Selectivity (%)	55.7 (±0.6)	55.1 (±0.7)
α_1 (C_1-C_7)	0.627 (0.620 – 0.634)	0.622 (0.615 – 0.629)
α_2 (C_8-C_{13})	0.691 (0.686 – 0.696)	0.653 (0.646 – 0.661)

CO conversions for the water and azomethane co-feeding experiments were respectively 94.2% and 94.5%. Experimental variation was large enough such that these

CO conversions were statistically equivalent to one another. The carbon atom selectivity of CO_2 was also nearly identical with and without azomethane shown in Table 5.2.

The chain growth probabilities of the product distributions with and without azomethane are approximately equivalent according to their 95% confidence intervals for the C_1-C_7 hydrocarbon range. However, C_8- C_{13} selectivity decreased to a statistically significant extent upon addition of the azomethane co-feed. This observation indicates that the addition and dissociation of methane may have led to an increase in the concentration of initiating species on the catalyst surface, thereby generating a lighter distribution of hydrocarbon products.

Figure 5.2 depicts paraffin fraction versus carbon number for the 1.0 H_2/CO inlet syngas case, where the error bars represent standard deviation. Table 5.3 shows the values of the two-sample t-statistics comparing the paraffin fractions of the experiments with water and azomethane ($n = 23$ for both water and azomethane/water, where n represents number of samples). A two-sample t-test proves distinctiveness between two statistical distributions – in this case paraffin fractions of the water and azomethane co-feeding experiments – at a certain confidence level. Values above the critical level of 3.79 indicate distinctiveness at 99.9% confidence for the paraffin fraction data of these experiments.

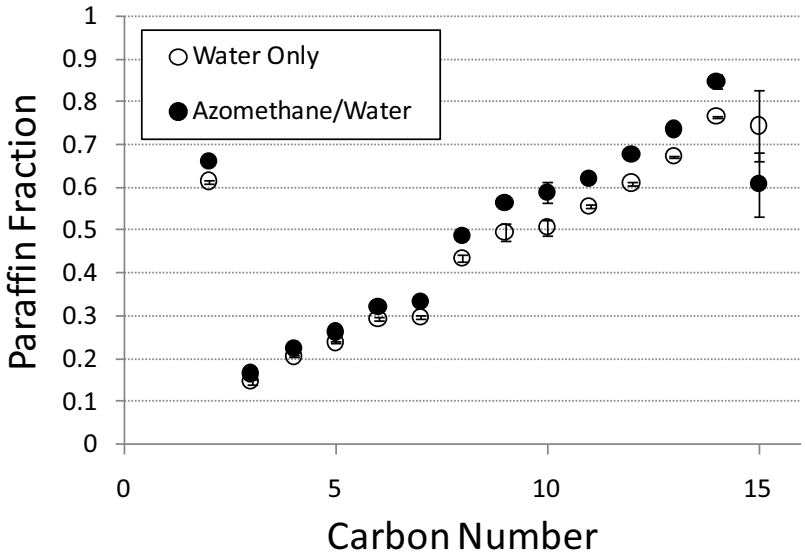

Figure 5.2: Paraffin fraction versus carbon number for the 1.0 H_2/CO inlet syngas case comparing the water and azomethane co-feeding experiments.

The values of the t-statistics are all well above the critical value proving statistical distinctiveness at 99.9% confidence (3.79 for n – 1 = 22 degrees of freedom), and the paraffin fractions for the azomethane co-feed are higher than those for the water co-feed across all carbon numbers except C_{15}. This observation may provide preliminary proof that methyl termination occurs during FT, as increased paraffin fraction would be expected assuming that such termination steps were occurring in the presence of added methyl surface species.

Table 5.3: Two-sample t-statistics comparing significance of the differences between observed paraffin fraction data of the water and azomethane co-feeding experiments (inlet syngas $H_2/CO = 1.0$). The critical t-value for 99.9% certainty of statistical distinctiveness is 3.79 with n – 1 = 22 degrees of freedom.

Carbon Number	Two-Sample t-Value
2	49.5
3	13.5
4	42.4
5	41.8
6	42.9
7	34.7
8	28.0
9	15.4
10	13.8
11	50.2
12	48.8
13	37.7
14	22.4
15	5.87

5.3.1.2 2.0 H_2/CO Case

Table 5.4 summarizes experimental observations for the co-feeding experiments in which inlet $H_2/CO = 2.0$. As for the case in which the inlet syngas H_2/CO ratio was 1.0, CO conversion and CO_2 carbon atom selectivity were statistically equivalent between the water and azomethane co-feeding experiments. The carbon atom selectivity of CO_2 was slightly lower in the 2.0 H_2/CO inlet syngas case, as lower partial pressures of CO slow the water-gas shift rate.

Table 5.4: CO conversion, CO_2 carbon atom selectivity, and alpha values for water and azomethane co-feeding experiments with inlet $H_2/CO = 2.0$. Parenthetic values next to CO conversion and CO_2 selectivity data represent standard deviations. Parenthetic values next to alpha values represent 95% confidence intervals.

Co-Feed	Water	Azomethane
CO Conversion (%)	92.4 (±0.2)	92.6 (±0.2)
CO_2 Selectivity (%)	48.9 (±1.1)	48.3 (±2.5)
α_1 (C_1-C_7)	0.602 (0.594 – 0.610)	0.596 (0.588 – 0.603)
α_2 (C_8-C_{13})	0.697 (0.686 – 0.709)	0.639 (0.627 – 0.651)

Chain growth probabilities in the C_1-C_7 range were again statistically similar, whereas the water co-feeding experiments generated a heavier product distribution in the C_8-C_{13} range. The observed disparity in α_2 was greater than in the 1.0 H_2/CO inlet syngas case. The increased partial pressure of hydrogen and resultant higher relative frequency of termination steps provide an explanation for this trend.

Paraffin fraction trends in the 2.0 H_2/CO inlet syngas case (Figure 5.3) were identical to those of the 1.0 H_2/CO case, where the azomethane co-feeding experiments generated products with a higher paraffin content across virtually the entire observed carbon number range. Table 5.5 demonstrates the statistical distinctiveness between paraffin fractions of the water and azomethane co-feeding experiments to 99.9% confidence.

The difference in paraffin fractions observed in Figure 5.3 for the 2.0 H_2/CO inlet syngas case are smaller than those seen in Figure 5.2 for the 1.0 H_2/CO inlet syngas case. The expected effect of methyl termination would be less drastic under conditions of higher hydrogen partial pressure, and this expectation was observed experimentally in the paraffin fraction data of both inlet syngas compositions.

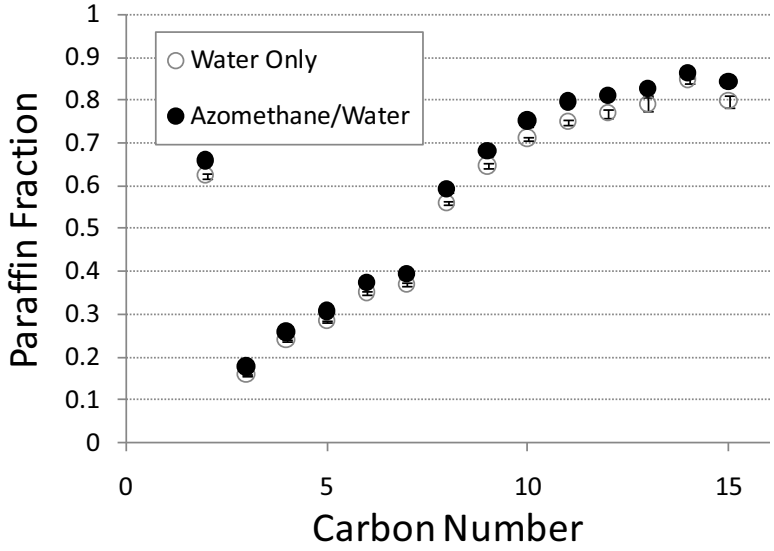

Figure 5.3: Paraffin fraction versus carbon number for the 2.0 H_2/CO inlet syngas case comparing the water and azomethane co-feeding experiments.

Table 5.5: Two-sample t-statistics comparing significance of the differences between observed paraffin fraction data of the water and azomethane co-feeding experiments (inlet syngas H_2/CO = 2.0). The critical t-value for 99.9% certainty of statistical distinctiveness is 3.79 with n – 1 = 22 degrees of freedom.

Carbon Number	Two-Sample t-Value
2	33.0
3	15.8
4	48.7
5	38.0
6	28.7
7	19.7
8	18.5
9	14.0
10	15.4
11	37.9
12	17.3
13	7.94
14	4.67
15	13.6

5.3.2 DRIFTS Investigation

Infrared spectra of a silica sample that was wet impregnated with an aqueous azomethane solution are shown in Figure 5.4. The three peaks between 3000 and 2500 cm^{-1} are associated with C-H bond stretching and gradually disappear with time at a temperature of 200°C. The broad rounded feature centered at approximately 3400 cm^{-1} is at first obscured by the C-H stretching features but becomes clearer after those features disappear. This feature persists after an hour on stream at 200°C and disappears immediately at 300°C; Rasko attributes this feature to hydrogen bonded surface species [12].

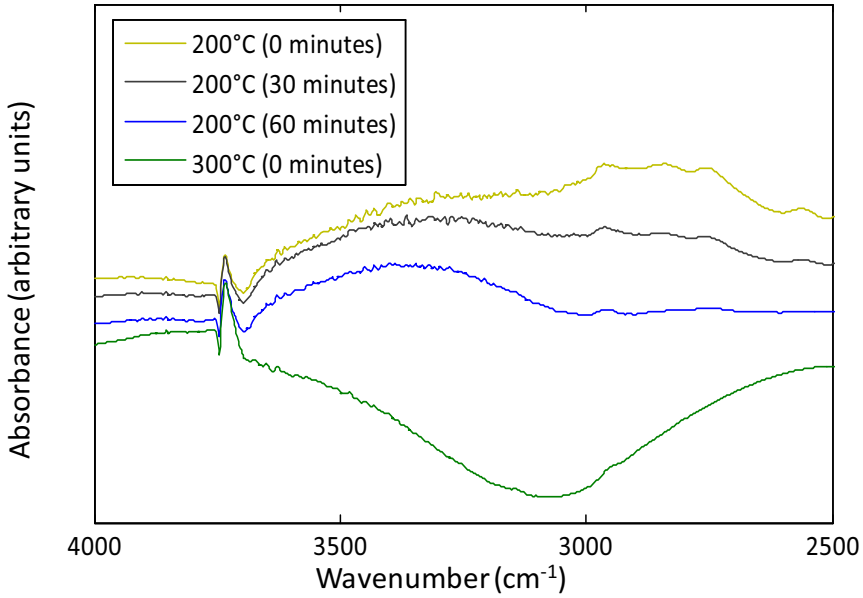

Figure 5.4: Infrared spectra of silica gel sample wet impregnated with aqueous azomethane.

The above observations provide some evidence for the thermal dissociation of azomethane at 200°C. The source of the C-H stretching vibration bands may be the methyl groups in azomethane, whereas the broad peak may be caused by the nitrogen in azomethane bound to the hydroxyl groups on the silica surface by hydrogen bonds. If

azomethane failed to dissociate, both features should disappear simultaneously as the compound was flushed from the silica surface. However, apparent disappearance of the methyl groups and persistence of surface-bound nitrogen suggest the dissociation of the two. Figure 5.5 pictorially represents the postulated surface events.

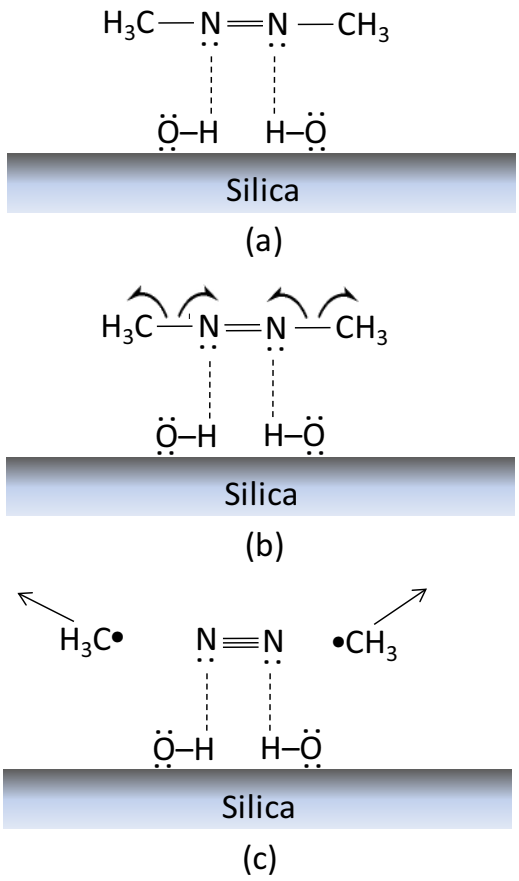

Figure 5.5: Pictorial representation of postulated azomethane desorption into methyl radicals and dinitrogen on silica based on evidence from infrared spectra.

DRIFTS analysis of the reduced iron catalyst wet impregnated with azomethane were less conclusive. Very slight absorbance features were observed from 3000 to 2800 cm^{-1}, and these features persisted to a temperature of 400°C on the catalyst surface. This observation may indicate the presence and persistence of methyl surface species on

reduced iron, but no further evidence of dissociation was observed. As such, homolytic cleavage of the C-N bond can only be presumed in the results described in Section 5.3.1.

5.4 Conclusions

The addition of an aqueous azomethane solution to the FT reactor resulted in the generation of a lighter yet more paraffinic product distribution compared to the distribution generated when only water was co-fed. Azomethane is known to dissociate into methyl radicals upon exposure to temperatures at which FT occurs, and given that methyl surface species act as hydrocarbon chain initiators, the creation of lighter products is unsurprising. The increased paraffinic nature of the products from the azomethane co-feeding experiments can potentially be explained by the greater frequency of methyl termination steps. This termination pathway is largely neglected in the FT modeling literature, but the evidence presented here supports its previously proposed significance [9].

The preceding conclusions operate under the assumptions that 1. azomethane was successfully co-fed with syngas into the FT reactor, 2. it thermally or catalytically dissociated into dinitrogen and methyl radicals, and 3. a portion of those methyl radicals adsorbed to the surface of the precipitated iron catalyst. The DRIFTS studies performed on azomethane impregnated silica seem to provide evidence of the dissociation of azomethane into methyl radicals and dinitrogen; those performed on azomethane impregnated iron provide very preliminary evidence for the presence of methyl surface species resulting from azomethane. Improved DRIFTS studies over iron should be performed to strengthen such conclusions.

References:

1. M. Dry, J. Chem. Technol. Biotechnol. 77 (2001) 43-50.
2. G. Keller, M. Bhasin, J. Catal. 73 (1982) 9-19.
3. N. Amin, S. Pheng, Chem. Eng. Journal 116 (2006) 187-195.
4. K. Peil, J. Goodwin, G. Marcelin, J. Catal. 131 (1991) 143-155.
5. M. Weissman, S. Benson, International J. Chem. Kinetics, 16 (1984) 307-333.
6. R. Brady, R. Pettit, J. Am. Chem. Soc. 102 (1980) 6182-6184.
7. W. van Barneveld, V. Ponec, J. Catal. 88 (1984) 382-387.
8. L. Hanley, X. Guo, J. Yates, J. Phys. Chem. 93 (1989) 6754-6757.
9. B. Wojciechowski, Catal. Reviews 30 (1988) 629-702.
10. R. Renaud, L. Leitch, Canadian J. Chem. 32 (1954) 545-549.
11. G. Huff, C. Satterfield, Ind. Eng. Chem. Process Des. Dev. 23 (1984) 696-705.
12. J. Rasko, App. Catal. A 225 (2002) 193-206.

Chapter Six

Conclusions and Future Work

6.1 Fischer-Tropsch Reaction Modeling

An FT reaction model over a precipitated iron catalyst with carbon number dependent rate constants is constructed in Chapter Two. The dissociation of reactants into chemically active species is modeled both by using quasi-equilibrium assumptions and by equating methylene monomer formation to an empirical rate law for CO consumption. Section 2.3.1.1 demonstrates that the carbon number dependent reaction model based on the empirical rate law (CNDERM) predicts CO conversion and CO_2 carbon atom selectivity better than the model based on quasi-equilibrium assumptions (CNDQEM). The empirical rate method was then used to compare the CNDERM with one from the literature that assumes secondary olefin re-adsorption (ORM).

In general, the CNDERM more closely predicts the experimental hydrocarbon selectivity and paraffin fraction data than the ORM. The most glaring deficiency of the ORM is its inability to predict the abnormally high C_2 paraffin fraction that is commonly observed in FT product distributions. It also seems incapable of predicting deviations from ASF, whereas the CNDERM approximates FT product distributions that deviate from a strictly logarithmic relationship between hydrocarbon selectivity and carbon number.

The apparent success of the CNDERM in calculating FT distributions does not necessarily confirm the suggested dependence of termination and propagation rate constants on the surface chain length. Further modeling work would be required in order to provide concrete evidence of such dependence; such calculations must have the ability to predict conformational positions of growing hydrocarbon chains relative to the catalyst surface based on physical and steric effects.

Quantification of uncertainty in the CNDERM represents one area in which the model must be improved in the future. First, uncertainty in the rate constants must be quantified based on experimentally observed error. The study of van der Laan and Beenackers reported an uncertainty range for certain input constants in its ORM, but did not directly report experimental error [1]. Calculation of uncertainty in the constants of the CNDERM would require either 1. undertaking further efforts to contact the authors regarding the uncertainty in their data, 2. assuming product rate data to be normally distributed about its reported value with a standard deviation of a fixed percentage of this nominal value, or 3. using different experimental data altogether. The statistical distributions of the experimental data could then be sampled to derive statistical distributions of the rate constants. Second, the distributions of the rate constants must be sampled when the program is run in MATLAB under the desired conditions. Such sampling would yield output distributions, the standard deviations of which could be reported as uncertainty in the model.

Two viable options exist for the aforementioned sampling. The first consists of determining the local sensitivities of the output variables (i.e., product rates) to changes in the rate constants within their statistical distributions. The input variable to whose

changes the outputs are most sensitive would then be randomly sampled about its normal distribution, thereby giving uncertainty in the model outputs. The second and more rigorous method consists of sampling each input parameter simultaneously using Latin Hypercube Sampling (LHS). The model would be run at each LHS sample point to generate uncertainty in the model's output parameters.

6.2 Distributed Syngas Feeding Experiments

Chapters Three and Four examine the effect of distributed syngas feeding on FT product distributions through plug flow reactors as compared to normal syngas feeding. These experiments took place over precipitated iron catalysts having simultaneous water-gas shift activity that can affect FT product distributions via CO consumption and H_2 generation.

The results of Chapter Three demonstrate that complete CO conversion in each reactor stage of a distributed syngas feeding regime is counterproductive to generating heavier FT product distributions regardless of inlet syngas composition, leading to a 60% reduction in C_{5+} hydrocarbon selectivity. Complete conversion in a staged manner leads to higher overall H_2/CO ratios along the axis of the reactor system, resulting in a lighter product distribution than that observed for a normal syngas feeding strategy.

A distributed syngas feeding strategy seems to improve the yield of heavy hydrocarbons in cases where incremental CO conversion is effected through the initial portion of the reactor system (Chapter Four); increases of up to 30% in C_{5+} hydrocarbon selectivity and 40% in C_{5+} hydrocarbon yield were experimentally observed. This phenomenon occurs consistently when hydrogen deficient syngas (H_2/CO = 1.0) is used

as a reactant whether incremental or near-complete CO conversion occurs over the remainder of the reaction axis. The use of hydrogen rich syngas ($H_2/CO = 2.0$) in a distributed feeding system does not consistently improve heavy hydrocarbon yields.

The apparent cause for the improvement under the distributed regime appears to be the suppression of water-gas shift activity and its resultant hydrogen production. This explanation is consistent with that of Sharifnia et al. during distributed hydrogen feeding studies in which decreasing hydrogen contact time in the reactor led to increased C_{5+} hydrocarbon yields [2].

Implementation of a distributed syngas feeding strategy in a multi-stage reactor system represents the next phase of the work presented in Chapters Three and Four. A reactor system with three to seven catalyst beds would be constructed to this end, with the ability to equally distribute a given amount of syngas among each bed. Only hydrogen deficient syngas would be utilized in this work given its proven efficacy at improving C_{5+} hydrocarbon yields in a distributed syngas feeding regime.

On a more applied level, the effect of adding CO_2 to the inlet syngas in a distributed regime should be examined. Idealized reactant mixtures consisting of only CO and H_2 were used in the experiments of Chapters Three and Four. Industrial syngas produced from coal or biomass contains 5-10% by volume CO_2 [3,4], and as such, the suppression of the water-gas shift reaction in Reactor 2 of the distributed regime may be affected by more accurately approximating inlet syngas.

6.3 Azomethane Co-Feeding Experiments

Chapter Five reports the results of experiments in which an aqueous azomethane solution was co-fed with syngas into a plug flow FT reactor over a precipitated iron catalyst. Azomethane thermally decomposes into methyl radicals and dinitrogen at FT temperatures; the motivation for studying the effect of these radicals on FT product distributions was twofold:

1. Methyl radicals derived from azomethane act as a surrogate for a recycled methane stream that has been reactivated through a second reactor.
2. Addition of methyl radicals into an FT system may shed light on the role of methyl surface species in the termination of hydrocarbon chains bound to the catalyst surface.

Azomethane co-feeding experiments resulted in lighter product distributions compared to experiments in which only deionized water was co-fed into the FT reactor through a saturator. The addition of methyl radicals, which act as the initiating species in the FT polymerization, decreases average chain length by increasing the ratio of initiating to propagating species on the catalyst surface. Despite the observed decrease in the average product weight, a more paraffinic distribution resulted when azomethane was co-fed, suggesting the occurrence of surface hydrocarbon chain termination by methyl radicals as opposed to solely hydrogen. Initial DRIFTS studies confirmed thermal azomethane dissociation and provided preliminary evidence for the resulting presence of surface methyl species on iron.

Future work in this area will concentrate on providing further experimental validation of the proposed effects of azomethane on FT product distributions. A more concentrated solution of azomethane should be synthesized and co-fed in an attempt to

amplify the effects reported in Chapter Five. Doing so would diminish the possibility that the experimental observations were caused by transient effects over the catalyst during time on stream. Additionally, further due diligence is required to confirm that azomethane is dissociating within the reactor and subsequently reaching the catalyst bed. This work can be accomplished by:

1. The use of a blank reactor held at the same temperature as the saturator containing the azomethane solution (approximately 80°C), into which a nitrogen stream saturated with aqueous azomethane would be introduced. Collection and visual inspection of condensed vapors at the exit of the blank reactor would confirm azomethane introduction into the reactor, as the compound exhibits a bright yellow color in aqueous solution.

2. The use of a blank reactor held at FT reaction temperature (270°C), into which into which a nitrogen stream saturated with aqueous azomethane would be introduced. Effluent analysis by gas chromatograph should reveal the presence of ethane, which in turn would indicate that thermal dissociation and subsequent recombination of methyl radicals had occurred within the reactor.

3. Further DRIFTS studies to confirm the persistence of methyl radicals on the catalyst surface and their interaction with CO. The reduced iron catalyst samples discussed in Section 5.4 were undiluted with silica or potassium bromide. Future studies will seek to improve the DRIFTS signal over iron by diluting the sample to less than 5% iron in potassium bromide and decreasing sample particle size to improve infrared signal strength. Additional studies in which CO is fed into the DRIFTS chamber with an azomethane impregnated catalyst sample may give information on the extent to which CO and azomethane occupy FT catalyst surface sites.

Future work in azomethane co-feeding will also seek to provide stronger evidence of methyl termination steps. The use of deuterated azomethane as a co-feed, followed by analysis using a gas chromatograph/mass spectrometer (GC/MS), would give more information on the extent to which methyl termination steps affect FT product distributions. The presence of hydrocarbon products with two deuterated methyl groups would provide concrete evidence of methyl termination, as one of the groups would have resulted from an initiating methyl species and the other necessarily would have resulted from a terminating methyl species.

6.4 Industrial Applicability

The work put forth in this dissertation seeks to investigate practical avenues into increasing FT selectivity in the transportation fuel range. As such, the preceding research would ideally be implemented in an FT plant with a minimum of modifications, and given future breakthroughs, make FT production possible on a smaller, distributed scale.

Implementation of a distributed syngas feeding strategy (Chapters Three and Four) in an existing FT plant represents the most easily enacted technique introduced in this dissertation. Chemical plants normally operate many reactors in parallel; a distributed syngas feeding strategy could be implemented by connecting two or more reactors in series with fresh syngas inlets between them. This technique could also easily be implemented in a skid-mounted distributed FT system, although the improvements reported herein are not adequate of themselves to render such a system economically feasible.

Recycle and subsequent activation of methane would prove more difficult to implement in either an existing plant or a proposed skid-mounted system. Methane activation steps normally occur at far different temperature conditions than FT, necessitating a separate reactor unit from which activated species must be quickly removed to prevent premature self-reaction. Before attempting to implement this technique, the efficacy of species resulting from activated methane in improving C_{5+} FT selectivity must be demonstrated.

Ideally, the marginal improvements resulting from each technique presented in this dissertation would be used in conjunction with one another. Any synergistic effects resulting from this combination would require further study at the laboratory and pilot scales before full-scale implementation in an FT plant or skid-mounted system. The role of FT reaction modeling would be critical to this study, as the FT reaction model developed in Chapter Two could be modified in an attempt to predict beneficial trends in FT selectivity.

Much work remains in the development of an FT process highly selective to transportation fuels such that distributed systems become economically possible. The invention of such a system will combine the efforts in the areas of catalysis research, reaction engineering, and process integration. The work presented in this dissertation highlights the need for continued innovation in the area of FT reaction engineering and establishes inroads into techniques that industrial practitioners may utilize in the future.

References:

1. G. van der Laan, A. Beenackers, Ind. Eng. Chem. Res. 38 (1999) 1277-1290.

2. S. Sharifnia et al., Fuel Proc. Technol. 86 (2005**)** 1253-1264.

3. From data supplied by treepower.org, http://www.treepower.org/fuels/biomasssyngas.html.

4. S. Shi et al., Fluent News (2004) S11, http://www.fluent.com/about/news/newsletters/04v13i2/pdfs/s11.pdf.

Appendix A

Definitions

The following parameters are used extensively throughout this dissertation, and their mathematical expressions are defined below.

- **CO conversion** is defined simply as the percentage of CO consumed in an FT reactor as compared to the amount fed to that reactor:

$$X_{CO} = \frac{F_{CO,o} - F_{CO,exit}}{F_{CO,o}} \tag{A-1}$$

where X_{CO} represents CO conversion, $F_{CO,o}$ represents the CO flowrate into the FT reactor, and $F_{CO,exit}$ represents the CO flowrate leaving the reactor. The reader should note that the CO conversion given within Reactor 1 of the distributed syngas feeding regimes described in Chapters Three and Four takes into account only the CO fed to its entrance as $F_{CO,o,}$ not the total amount of CO eventually fed to the system.

- **Hydrocarbon selectivity** is defined as the molar fraction of a given hydrocarbon product in the FT reactor effluent as compared to the total moles of hydrocarbon products, such that:

$$S_n = \frac{F_n}{\sum_{i=1}^{x} F_i} \tag{A-2}$$

where S_n represents the hydrocarbon selectivity of a hydrocarbon species containing n carbon atoms, F_n represents the effluent molar flowrate of the hydrocarbon species containing n carbon atoms, F_i represents the molar flowrate of the hydrocarbon species containing i carbon atoms, and x represents the carbon number of the heaviest analyzed product (10 for the reaction model of Chapter Two, 15 for the experiments of Chapters Three through Five). Hydrocarbon selectivity naturally excludes CO_2.

- **Carbon atom selectivity** is defined as the fraction of carbon contained in a specific product as compared to the total amount of carbon contained in all products. For hydrocarbon species, it is defined as:

$$Y_n = \frac{nF_n}{F_{CO2} + \sum_{i=1}^{x} iF_i} \tag{A-3}$$

where Y_n represents the carbon atom selectivity of a hydrocarbon species containing n carbon atoms, F_n represents the molar effluent flowrate of a hydrocarbon species containing n carbon atoms, F_{CO2} represents the molar effluent flowrate of CO_2, F_i represents the molar flowrate of the hydrocarbon species containing i carbon atoms, and x represents the carbon number of the heaviest analyzed product. For CO_2, carbon atom selectivity is defined as:

$$Y_{CO2} = \frac{F_{CO2}}{F_{CO2} + \sum_{i=1}^{x} iF_i} \tag{A-4}$$

where Y_{CO2} represents the carbon atom selectivity of CO_2. The selectivity of CO_2 is defined strictly on a carbon atom basis throughout this dissertation, as this parameter reflects the proportion of CO converted to CO_2 via the water-gas shift relative to CO converted to hydrocarbons via FT.

- **Paraffin fraction** is defined as the fraction of paraffin products of a given carbon number relative to the sum of paraffin and olefin products of that carbon number, such that:

$$P_n = \frac{F_{pn}}{F_{pn} + F_{on}} \tag{A-5}$$

where P_n represents the paraffin fraction of a hydrocarbon species containing n carbon atoms, F_{pn} represents the molar effluent flowrate of a paraffin product containing n carbon atoms, and F_{on} represents the molar effluent flowrate of an olefin product containing n carbon atoms.

The results of Chapter Three present paraffin fraction averaged from C_2 to C_{15}, such that:

$$P_T = \frac{\sum_{i=2}^{15} F_{pi}}{\sum_{i=2}^{15} (F_{pi} + F_{oi})} \tag{A-6}$$

where P_T represents the total paraffin fraction of C_2-C_{15} products, F_{pi} represents the molar effluent flowrate of a paraffin product containing i carbon atoms, and F_{oi} represents the molar effluent flowrate of an olefin product containing i carbon atoms.

- **Chain growth probability**, represented by the symbol α, is defined as part of the expression:

$$m_n = n \ln \alpha + \ln\left(\frac{1-\alpha}{\alpha}\right) \tag{A-7}$$

where m_n represents the hydrocarbon selectivity of a hydrocarbon product containing n carbon atoms. The term α can be determined by taking the inverse logarithm of the slope from a plot of hydrocarbon selectivity versus carbon number, and it has a value between zero and unity (although local values greater than unity are possible). The average molecular weight of an FT product distribution increases with increasing α.

A double-α model is used in this dissertation, where lines of best fit are derived for two different ranges of carbon numbers within a given product distribution, e.g., C_1-C_5 and C_6-C_{15}, and separate α-values are found from the slopes of each line. This method is used to account for the clear break that occurs in the plot of hydrocarbon selectivity versus carbon number that occurs in the C_5-C_7 range of the FT hydrocarbon product distributions observed in the experiments of this dissertation.

Appendix B

Analysis of Reactor Effluent Streams

B.1 Physical Design of Gas Chromatograph

A Varian CP-3800 gas chromatograph (GC) was used to detect and quantify the chemical species comprising the effluent of the reactors in the experiments described in Chapters Three through Five. The GC was designed such that the reactor effluent was introduced into it through three parallel channels, each of the channels equipped with a detector for the analysis of different species. The effluent was introduced into each channel by means of pneumatically activated valves. Under normal circumstances, the effluent flowed into the valves through sample loops to the atmosphere. At the beginning of a sample run, a valve event occurred to introduce the gases in the sample loop to the separation column(s) and detector associated with that channel. The valves and sample loops were housed in an oven heated to 200°C to prevent the condensation of C_{5+} hydrocarbons.

Separation columns were placed between the channel inlets and associated detectors to achieve separation of the chemical species in advance of detection and quantification by the respective detectors. Sections B.1 through B.3 give further detail on species separation and quantification within each channel.

B.1.1 Channel 1 Setup

Channel 1 was equipped with a thermal conductivity detector (TCD) for the quantification of carbon monoxide, carbon dioxide, and nitrogen gases. Methane was also visible to this detector but was instead quantified using the flame ionization detector (FID) of Channel 3, described later in this section.

Helium was used as the carrier gas to the TCD of Channel 1. The peak areas associated with hydrogen are highly non-linear with concentration when helium is used as a carrier gas, and as such, the subsequently described TCD of Channel 2 was used for hydrogen quantification. Helium flowrates through Channel 1 are given in section B.2. The separation columns associated with this channel existed in a somewhat complicated configuration that provided for the separation and accurate quantification of CO, CO_2, and N_2. The analytes were first run through two packed bed columns in series – the first of these was a 0.5 meter long, 1/8" outer diameter Hayesep T column with 80/100 mesh size packing material, and the second was a 0.5 meter long, 1/8" outer diameter Hayesep Q column with 80/100 mesh size packing material. This configuration resulted in the separation of analyte gases such that a mixture of N_2, CO, and CH_4 eluted first and CO_2 eluted second.

The mixture of N_2, CO, and CH_4 was then sent through a pneumatically activated valve and directed to a packed column equipped with a molecular sieve (Molsieve 13X) measuring 1.5 meters in length and 1/8" in outer diameter with 80/100 mesh size material. This column would ensure effective separation of N_2, CO, and CH_4 that had not been accomplished through the previous Hayesep columns. These gases were then directed to the TCD for quantification.

The elution of CO_2 through the first two series Hayesep columns occurred after elution of the N_2/CO/CH_4 mixture. The CO_2 then flowed through the same pneumatic valve as the previously eluted gaseous mixture but was instead diverted through a needle valve restriction parallel to the molecular sieve column. This setup ensured that CO_2 did not come into contact with the molecular sieve column, the packing material of which would irreversibly adsorb CO_2 and thereby ruin the column.

The initial GC setup allowed for CO_2 to quickly flow through the needle valve restriction and arrive at the TCD prior to the gaseous mixture traversing the molecular sieve column. However, changes in retention time through the Hayesep columns necessitated the development of a separate GC method for the quantification of CO_2, further described in Section B.2.

B.1.2 Channel 2 Setup

Channel 2 was equipped with a TCD for the detection and quantification of hydrogen. Argon was used as the carrier gas through this channel to avoid the complications of quantifying hydrogen with helium as a carrier gas. Argon flowrates are given in Section B.2.

The analytes introduced into Channel 2 traversed two packed bed columns in series; the first was a packed bed Hayesep Q column with 80/100 mesh size packing material measuring 1.0 meters in length and 1/8" in outer diameter, and the second was a packed bed molecular sieve column (Molsieve 5A) with 80/100 mesh size packing material measuring 1.0 meters in length and 1/8" in outer diameter.

Hydrogen eluted first from the Hayesep column and was allowed to enter the molecular sieve column. The entry of hydrogen into the second column coincided with a valve timing event such that all other components of the reactor effluent were forced backward through the Hayesep column to an external vent in order to prevent contact with the molecular sieve column. Hydrogen then eluted through the second column to the TCD for quantification.

B.1.3 Channel 3 Setup

Channel 3 was equipped with an FID for detection and quantification of all hydrocarbon species up to C_{15}. Analyte separation was accomplished by means of a capillary column (CP-Porabond Q) measuring 25 meters in length and 0.32 millimeters in internal diameter with a coating thickness of five micrometers. After separation the hydrocarbon analytes arrived at the FID whose flame was sustained by a stoichiometric mixture of hydrogen and air. The temperature ramp rate of the column is described in Section B.2.

B.2 Gas Chromatograph Method for Analyte Quantification

The method to analyze reactor effluent streams lasted 28.13 minutes in total. The helium carrier gas was fed through Channel 1 at 1.0 mL/min and 19.6 psig. The argon carrier gas was fed through Channel 2 at 60 mL/min and 35.0 psig. Hydrogen and air were fed at a stoichiometric ratio through Channel 3 at a total flowrate of 60 mL/min and 31.8 psig. The respective temperatures of the Channel 1 TCD, Channel 2 TCD, and Channel 3 FID were maintained at 250°C, 280°C, and 300°C.

The temperature of the oven in which the separation columns were housed was maintained at 45°C for the first 13.5 minutes of the sample method, during which C_1-C_5 hydrocarbons eluted through the capillary column in Channel 3. At 13.5 minutes, a temperature ramp rate of 40C°/minute up to 230°C was implemented to effect the vaporization and elution of hydrocarbons heavier than C_5.

Separate methods were run for the quantification of CO_2 and N_2/CO via the Channel 1 TCD. These methods were run at the conditions described in this section; the only difference between the two methods involved a timing event in the pneumatically activated valve following the Channel 1 Hayesep columns. The experiments described in Chapters Three to Five took place at steady state over multiple days, ensuring that the collection of CO_2 and N_2/CO concentration data in distinct samples would not affect the experimental results.

B.3 Gas Chromatograph Calibration

The peak areas associated with the TCD and FID responses were linear with respect to concentration for each analyte. The following sections describe the calibration procedure for each chemical species that was analyzed in the experiments described in Chapters Three through Five.

B.3.1 Nitrogen

The calibration curve for nitrogen was attained using gaseous mixtures containing 10% and 20% nitrogen by volume and was based on the response from the Channel 1 TCD. Table B.1 summarizes the peak areas found at each concentration; the resulting

calibration curve assumed that a peak area of zero occurred at a nitrogen concentration of zero.

Table B.1: Peak area counts for nitrogen under calibration conditions.

Nitrogen Composition (volume %)	Trial 1	Trial 2	Trial 3	Average
10	2413222	2375602	2422035	2403620
20	5070450	4985510	5032178	5029379

The area count divisor resulting from the above calibration was 249248, meaning that peak area counts attained from each GC sample were divided by this number to arrive at the volume percentage of nitrogen contained within the sample.

B.3.2 Carbon Monoxide

The calibration curve for carbon monoxide was attained using gaseous mixtures containing 5%, 10% and 20% carbon monoxide by volume and was based on the response from the Channel 1 TCD. Table B.2 summarizes the peak areas found at each concentration; as with nitrogen, the resulting calibration curve assumed that a peak area of zero occurred at a carbon monoxide concentration of zero. The resulting area count divisor was 257455.

Table B.2: Peak area counts for carbon monoxide under calibration conditions.

Carbon Monoxide Composition (volume %)	Trial 1	Trial 2	Trial 3	Trial 4	Average
5	1263000	1235675	1257190	1240654	1249130
10	2580745	2551691	2558192	2573076	2565926
20	5156976	5173479	5158417	--	5162957

B.3.3 Carbon Dioxide

The calibration curve for carbon dioxide was attained using a gaseous mixture of 4.89% carbon dioxide by volume and was based on the response from the Channel 1 TCD. Table B.3 summarizes the peak areas found at this concentration; the calibration curve was assumed to run through zero at a CO_2 concentration of zero. The resulting area count divisor based on Trials 3 through 6 was 2166788.

Table B.3: Peak area counts for carbon dioxide under calibration conditions.

Carbon Dioxide Composition (volume %)	Trial 1	Trial 2	Trial 3	
4.89	11060772	10446669	10570020	
4.89	Trial 4	Trial 5	Trial 6	Average (Trials 3-6)
	10579308	10598236	10634812	10595594

B.3.4 Hydrogen

The calibration curve for hydrogen was attained using gaseous mixtures containing 10%, 20%, 80%, and 90% hydrogen by volume and was based on the response from the Channel 2 TCD. Table B.4 summarizes the peak areas found at each concentration; again, the calibration curve was assumed to reach zero area counts at a hydrogen concentration of zero. The resulting area count divisor was 46494.

Table B.4: Peak area counts for hydrogen under calibration conditions.

Hydrogen Composition (volume %)	Trial 1	Trial 2	Trial 3	Trial 4	Average
10	496515	495687	--	--	496101
20	981910	981508	982754	978827	981250
80	3728562	3731006	3746382	--	3735317
90	4159106	4160194	4147259	--	4155520

B.3.5 Methane

The calibration curve for methane was attained using gaseous mixtures containing 0.1%, 4.0%, 10%, and 20% methane by volume and was based on the response from the Channel 3 FID. Table B.5 summarizes the peak areas found at each concentration; the calibration curve was assumed to reach zero at a methane concentration of zero. The resulting area count divisor was 86335.

Table B.5: Peak area counts for methane under calibration conditions.

Methane Composition (volume %)	Trial 1	Trial 2	Trial 3	Average
0.1	10063	8098	8003	8721
4.0	317043	317030	--	317037
10	866432	870139	870327	868966
20	1730172	1729309	1729180	1729554

B.3.6 C_2-C_{15} n-Paraffins and α-Olefins

A mixture of 1000 parts per million by volume each of methane, ethane, propane, butane, pentane, and hexane (balance helium) was used to generate a calibration curve for these hydrocarbon species. Figure B.1 displays the peak area counts from this calibration.

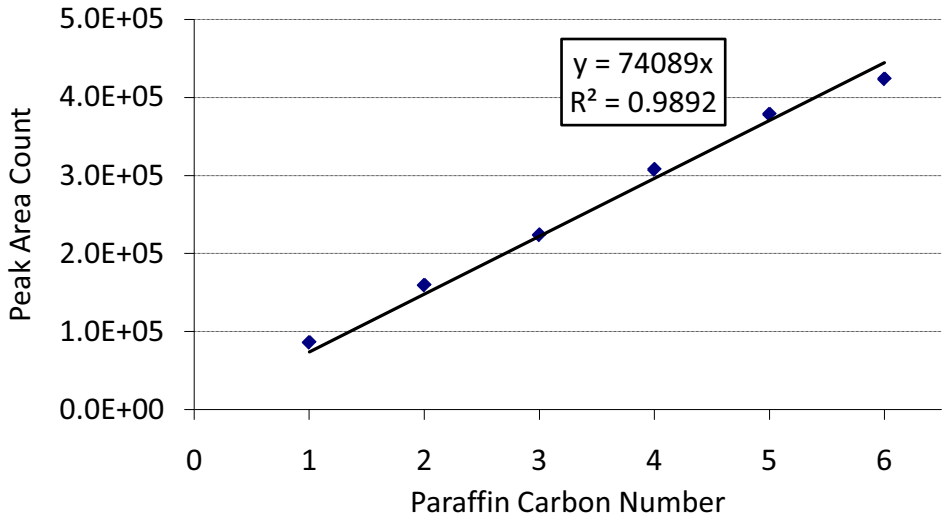

Figure B.1: Peak area count versus carbon number for C_1-C_6 n-paraffin species at 1000 ppm.

The FID response to paraffins was highly linear with respect to carbon number, and as such, the concentration of C_7-C_{15} paraffins was determined by the extrapolation of this line.

Similarly, a mixture of 1000 parts per million by volume each of ethylene, propylene, 1-butene, 1-pentene, and 1-hexene (balance helium) was used to generate a calibration curve for these hydrocarbon species. Figure B.2 displays the peak area counts from this calibration.

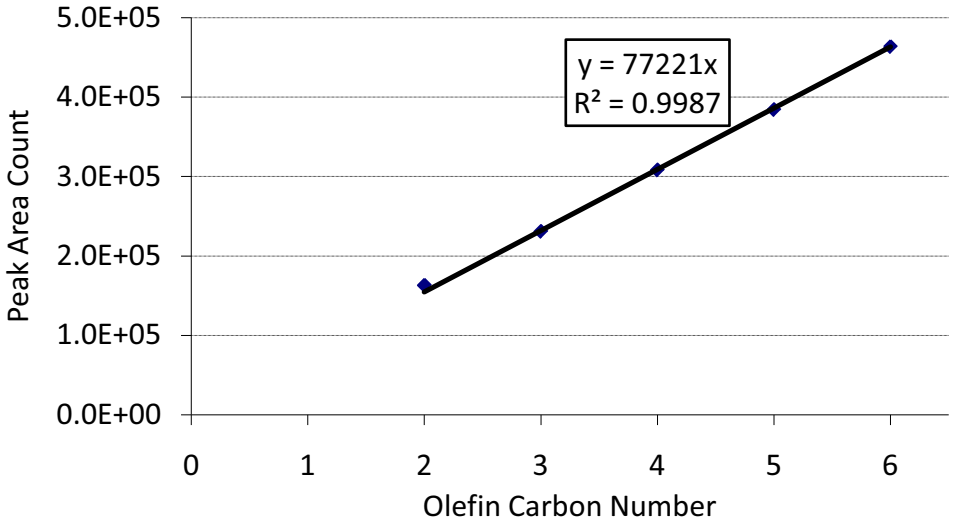

Figure B.2: Peak area count versus carbon number for C_2-C_6 α-olefin species at 1000 ppm.

As with n-paraffins, the response of the FID was highly linear with respect to α-olefin carbon number. The concentration of C_7-C_{15} α-olefins was extrapolated from the trend line in Figure B.2.